IFC·IBC·contents&author 9/26/05 10:56 AM Page 1

Vol. 66, No. 1, March 2005
KDN PP5476/7/2005 ISSN 0126-513X

MAJLIS BAGI SESI 2005/2006 (IEM COUNCIL SESSION 2005/2006)

YANG DIPERTUA / *PRESIDENT:*
Ir. Prof. Dr Ow Chee Sheng

TIMBALAN YANG DIPERTUA / *DEPUTY PRESIDENT:*
Y. Bhg. Dato' Paduka Ir. Keizrul bin Abdullah

NAIB YANG DIPERTUA / *VICE PRESIDENTS:*
Ir. Choo Kok Beng, Ir. Neoh Cheng Aik, Ir. Prof. Ishak bin Abdul Rahman, Ir. Prof. Dr Chuah Hean Teik, Ir. Prof. Dr Ruslan bin Hassan, Y. Bhg. Dato' Ir. Hj Abdul Rashid bin Maidin, Ir. Tan Yean Chin

SETIAUSAHA KEHORMAT / *HONORARY SECRETARY:*
Ir. M.C. Hee

BENDAHARI KEHORMAT / *HONORARY TREASURER:*
Ir. Lee Weng Onn

WAKIL STRUKTUR / *STRUCTURAL REPRESENTATIVE:*
Ir. Jeffrey Chiang Choong Luin

WAKIL AWAM / *CIVIL REPRESENTATIVE:*
Ir. Aik Siaw Kong

WAKIL ELEKTRIK / *ELECTRICAL REPRESENTATIVE:*
Ir. Mah Soo

WAKIL MEKANIK / *MECHANICAL REPRESENTATIVE:*
Ir. Gopal Narian Kutty

WAKIL KIMIA & DISIPLIN LAIN / *CHEMICAL & OTHERS REPRESENTATIVE:*
Ir. Ahmad Nordeen bin Mohd. Salleh

AHLI MAJLIS / *COUNCIL MEMBERS:*
Ir. Dr Wong Chin Chaw, Ir. Prof. Dr Siti Hamisah binti Tapsir, Ir. Chin Mee Poon, Ir. Peter Tan Hoh You, Ir. Kukanesan a/l Sakthiveil, Ir. Muhammad Imran bin Baharuddin, Ir. Adnan bin Zulkiple, Ir. David Lai Kong Phooi, Ir. Manogaran a/l K. Raman, Ir. Hj. Mohd. Hassin @ Mohd Hashim Daud, Ir. Assoc. Prof. Lt. Kol. Mohd. Hazani bin Hj. Shafie, Ir. Mohd. Rasid bin Osman, Ir. Woo Ah Keong, Ir. Yeo Boon Kah, Ir. Yusouf bin Ahmad, Ir. Dr Tee Tiam Ting, Ir. Vincent Chen Kim Kieong, Ir. Dr Tan Yean Guan, Ir. Dr G. Balamurugan, Ir. Yim Hon Wa, Ir. Patrick Cyril Augustin, Ir. Major (R) Hj. Ahmad Mazlan bin Othman, Ir. Assoc. Prof. Dr Norlida binti Buniyamin, Ir. Hoo Choon Sean, Ir. Ching Chin Chuan, Ir. Awangku Hidup bin Awangku Hosain, Y. Bhg. Datuk Abdul Hadi bin Mohd. Deros, Ir. Dr Judin bin Abdul Karim

BEKAS YANG DIPERTUA TERAKHIR / *IMMEDIATE PAST PRESIDENT:*
Ir. Prof. Abang Abdullah bin Abang Ali

BEKAS YANG DIPERTUA / PAST PRESIDENT:
Y. Bhg. Tan Sri Ir. (Dr) J. G. Daniel, Ir. T. T. Chiam, Y. Bhg. Dato' Ir. Pang Leong Hoon, Y. Bhg. Academician Dato' Ir. Lee Yee Cheong, Ir. P.E. Chong, Y. Bhg . Dato' Ir. Abdul Rashid bin Ahmad, Ir. Dr Ting Wen Hui, Ir. Hj. Mohd Mazlan, Y. Bhg. Datuk Ir. (Dr) Hj. Ahmad Zaidee bin Laidin, Ir. Dr Gue See Sew

PENGERUSI CAWANGAN / *BRANCH CHAIRMAN:*
Pulau Pinang – Ir. Vincent Tan Huei Meng
Selatan – Ir. Steve Chong Yoon On
Perak – Y. Bhg. Dato' Ir. Hj. Abdul Rahman bin Dahan
Timur – Y. Bhg. Dato' Ir. Hj. Annies bin Md. Ariff
Terengganu – Y. Bhg. Dato' Ir. Hj. Mohamad bin Husin
Negeri Sembilan – Ir. Hj. Ahmad Husaini bin Hj. Sulaiman
Melaka – Ir. Hj. Abd Rahim bin Shamsudin
Sarawak – Ir. Zawawi bin Embong
Sabah – Ir. Lee Tet Fon
Miri – Ir. Dr Edwin Jong Nyon Tchan
Kedah-Perlis – Y. Bhg. Dato' Ir. Hj. Abdullah bin Hj. Abbas

AHLI JAWATANKUASA PENERBITAN / *STANDING COMMITTEE ON PUBLICATIONS:*
Pengerusi / Chairman: Ir. Prof Ruslan bin Hassan
Naib Pengerusi / Vice Chairman: Ir. Dr G. Balamurungan a/l B. Gurusamy
Setiausaha / Secretary: Ir. Assoc. Prof. Dr Junaidah binti Ariffin
Pengerusi (Perpustakaan) / Library Chairman: Dr Chuah Teong Guan
Ahli-Ahli / Committee Member: Ir. Chin Mee Poon, Ir. Mah Soo, Ir. Look Keman bin Hj. Sahari, Ir. Dr Jeffrey Chiang Choong Luin, Sdr. K.H. Man

LEMBAGA PENGARANG / *EDITORIAL BOARD:*
Ketua Pengarang / *Chief Editor* – Ir. Chin Mee Poon
Pengarang (Bulletin) / *Bulletin Editor* – Ir. Mah Soo
Pengarang (Jurnal) / *Journal Editor* – Ir. Assoc. Prof. Dr Aminuddin bin Mohd. Baki
Setiausaha / *Secretary* – Ir. Assoc. Prof. Dr Junaidah binti Ariffin
Ahli-Ahli / *Committee Member* – Ir. Dr Jeffrey Chiang Choong Luin, Ir. Look Keman bin Hj. Sahari, Sdr. K.H. Man

AHLI JAWATANKUASA JOURNAL / SUB-COMMITTEE ON JOURNAL:
Pengerusi / *Chairman* – Ir. Assoc. Prof. Dr Aminuddin bin Mohd. Baki
Ahli-Ahli / *Committee Member* – Ir. Assoc. Prof. Dr Junaidah binti Ariffin, Ir. Mohd. Taufik bin Salleh, Ir. Mohd. Zawawi bin Ahmad, Ir. Dr Jeffrey Chiang Choong Luin, Assoc. Prof. Dr Mohamad Azmi bin Ayob

THE INSTITUTION OF ENGINEERS, MALAYSIA
Bangunan Ingenieur, Lots 60 & 62, Jalan 52/4, P.O. Box 223,
(Jalan Sultan) 46720 Petaling Jaya, Selangor.
Tel: 03-7968 4001/4002 Fax: 03-7957 7678
E-mail: sec@iem.org.my Homepage: http://www.iem.org.my

Printed by : SETIAKAWAN PRINTERS SDN. BHD.
NO. 5 & 7, Jalan Industri PBP 11,
Taman Industri Pusat Bandar Puchong, 47100 Selangor Darul Ehsan, Malaysia.
Tel: 603-5891 7363 Fax:603-5891 7232/33 E-mail: skpsb@tm.net.my

CONTENT

1 **Kesan Kuantiti Agen Penyerak Dalam Pencirian Saiz Zarah Oksida Seramik Menggunakan Kaedah Pembelauan Laser** *by A. Muchtar*

6 **Analysis of Design Parameter Effects on Vibration Modes of a Motorcycle Drum Brake and Brake Shoe Using the Finite Element Method** *by Zahrul Fuadi*

13 **Elasto-Plastic Deformation of Hostun Sand During Cyclic Loading in Triaxial Test** *by Eqramul Hoque*

19 **A Generalised Price-Scoring Model for Tender Evaluation** *by Thum Peng Chew*

28 **Numerical Modelling of Reverse Pulse Cleaning on Rigid Ceramic Filters** *by T. G. Chuah*

34 **A Method to Evaluate Design Efficiency Based on Assembly Criteria in Support of Design for Modularity** *by A. B. Abdullah*

41 **Bedload Transport Model for Field Conditions - Using Characteristic Diameter Approach** *by Mohammad Ashiq*

53 **Highly Reactive Electrogenerated Zinc: Perparation and its Use in Cross-Coupling Reactions***by Aishah Abdul Jalil*

61 **Determination of Probability Distribution for Data on Rainfall and Flood Levels in Bangladesh** *by M. Ferdows*

73 **Development and Performance Evaluation of a Prototype Electric Hybrid Powertrain System for Automotive Applications** *by Azhar Abdul Aziz*

INTERNATIONAL ADVISORY PANEL

Prof. J. M. Owen
University of Bath, UK

Prof. Don Mclean
University of Southampton, UK

Prof. Hiroshi Yabe
University of Kyoto, Japan

Prof. M. Rodds
University of Wales, UK

Prof. A. J. Saul
University of Sheffield, UK

BRANCHES

HEAD-QUARTERS	**THE INSTITUTION OF ENGINEERS, MALAYSIA** BANGUNAN INGENIEUR, LOT 60/62, JALAN 52/4 PETI SURAT 223, 46720 PETALING JAYA, SELANGOR.	**TEL: 03-7968 4001** **7968 4002** **FAX: 03-7957 7678**
KEDAH-PERLIS	**THE INSTITUTION OF ENGINEERS, MALAYSIA** CAWANGAN KEDAH-PERLIS, NO. 135, 2ND FLOOR, KOMPLEKS ALOR SETAR, LEBUHRAYA DARUL AMAN, 05100 ALOR SETAR, KEDAH.	**TEL: 04-734 3420** **FAX: 04-733 3962**
PENANG	**THE INSTITUTION OF ENGINEERS, MALAYSIA** LEVEL 5, 5-A NORTHAM VENTURE, 37 JALAN SULTAN AHMAD SHAH, 10050 PENANG	**TEL: 04-818 2045** **808 2046** **FAX: 04-818 2046**
SARAWAK	**THE INSTITUTION OF ENGINEERS, MALAYSIA** ULTIMATE PROFESSIONAL CENTRE 2ND FLOOR, 16 JALAN BUKIT MATA KUCHING, 93100 KUCHING, SARAWAK.	**TEL: 082-428 506** **FAX: 082-243 718**
MIRI	**THE INSTITUTION OF ENGINEERS, MALAYSIA** LOT 2935, 2ND FLOOR, FARADALE COMMERCIAL CENTRE, JALAN BULAN SABIT, 98000 MIRI, SARAWAK.	**TEL: 085-453 297** **FAX: 085-454 959**
PERAK	**THE INSTITUTION OF ENGINEERS, MALAYSIA** NO. 11, JALAN JOHAN 1/2, KAWASAN PERINDUSTRIAN PENGKALAN II, BATU 7, 31550 LAHAT, PERAK.	**TEL: 05-365 4733** **FAX: 05-365 4739**
NEGERI SEMBILAN	**THE INSTITUTION OF ENGINEERS, MALAYSIA** No. 28-1, JALAN DURIAN EMAS 4, BETARIA BUSINESS CENTRE OFF JALAN DATO' SIAMANG GAGAP 70100 SEREMBAN, NSDK.	**TEL: 06-767 7333** **FAX: 06-767 7000**
TERENGGANU	**THE INSTITUTION OF ENGINEERS, MALAYSIA** D/A JKR, TINGKAT 12, WISMA NEGERI, 20200 KUALA TERENGGANU, TERENGGANU	**TEL: 09-622 2444** **FAX: 09-623 5624**
MELAKA	**THE INSTITUTION OF ENGINEERS, MALAYSIA** 2, JALAN MALINJA 2, TAMAN MALINJA, BUKIT BARU, 75150 MELAKA..	**TEL: 06-284 8028** **FAX: 06-283 8919**
SABAH	**THE INSTITUTION OF ENGINEERS, MALAYSIA** 77-3, WISMA NEW FAR EAST, LUYANG, 88855 KOTA KINABALU, SABAH.	**TEL: 088-236 749** **FAX: 088-236 749**
SOUTHERN	**THE INSTITUTION OF ENGINEERS, MALAYSIA** NO. 24-B, JALAN ABIAD, TAMAN TEBRAU JAYA, 80400 JOHOR BAHRU.	**TEL: 07-331 9705** **FAX: 07-331 9710**
EASTERN	**THE INSTITUTION OF ENGINEERS, MALAYSIA** PEJABAT PENGARAH KERJA RAYA KELANTAN, JALAN KUALA KRAI, 15050 KOTA BHARU, KELANTAN DARUL NAIM.	**TEL: 09-745 5901** **FAX: 09-745 5970**

INFORMATION FOR AUTHORS

Submission of a contribution is taken to manifest the fact that the submission has not been submitted, accepted, published, or copyrighted elsewhere.

To avoid publication delays, please send all manuscripts to the Editor and observe the following guidelines.

A) SUBMISSION OF PAPER

Send four (4) copies of your manuscript. Each copy should be complete with illustrations (if any) and an abstract. Submission should be made to the address below :

Chief Editor
The Institution of Engineers, Malaysia
Bangunan Ingenieur,
Lots 60 & 62, Jalan 52/4
Peti Surat 223, Jalan Sultan
46720 Petaling Jaya
Selangor Darul Ehsan
Tel : 03 – 7968 4001 / 7968 4002
Fax : 03 – 7957 7678

Three types of papers are solicited for the IEM Journal:

(1) **Regular Paper** – Presentation of significant research, developments or applications in any field of engineering or within the scope of the journal. Tutorials and surveys are also considered. For submission, the length should be about 30 pages; double-spacing, single column with font of 12 (Times).

(2) **Brief Paper** – A concise description of new technical concepts or applications within the scope of the journal. Submission should be about 20 pages; double-spacing, single column with font of 12 (Times).

(3) **Technical Correspondence** – Letter to the Editor, comments on established engineering topics and discussion of published papers. Submission should be about 10 pages; double-spacing, single column with font of 12 (Times).

NOTE: *In the event your paper is accepted for publication, the style of manuscript is in a different format (see point 7 below)*

Manuscripts submitted as papers should state the significance of the problem in the Introduction.

Paper size should be of A4 (210 cm x 297 cm) with 2 cm margins on the left, right, and bottom and 3 cm from the top.

Enclose a signed letter giving your preferred address, telephone, fax number, and e-mail address (if available) for correspondence and return of proofs.

If the manuscript has been presented, published, or submitted for publication elsewhere, please also inform the Editor. Our primary objective is to published technical materials not available elsewhere, but on occasion we publish papers of unusual merit that have appear or will appear before other audiences.

The language of the journal is English. However, a papers in Bahasa Melayu are also accept and an abstract in English must be included.

Note that upon acceptance of an article for publication, the author is requested o submit a camera-ready format of the manuscript with single-spacing, double-column and font of 10 (Times). Illustrations and keywords of the papers should be included in the text. An electronic copy of the manuscript should also be submitted together with the hardcopies. The author is also requested to submit a passport-sized and a short biography. This information will be sent to the author by the Editor.

B) STYLE FOR MANUSCRIPT

The manuscript should be typewritten using double-space, using font of 12 (Times); use one side of sheet only and single column format.

The format for IEM Journal follows that of the IEEE Transactions (USA), except that the submission for you should follow Point 1 above.

As we practice blind review, please do not put your name and address in the manuscript.

Provide and informative 100- to 250- word abstract at the head of the manuscript.

All section should be numbered in Roman such as 1, 11, etc. with the title in capitals.

Sub-sections should be numbered in alphabet such as A, B, C, etc.

Sub-sub-sections (if any) should be numbered as A., A.2, etc.

Number all equations in round brackets such as ( ) and flush to right. The equation should be in the center.

References in the text should be cited each by a reference number in square brackets, e.g. [12] or [4-6], etc.

In the reference section, the references should be written as follows :
Style for papers: Reference Number, Author, first initials followed by last name, title (italics), location and publisher, year, chapter or page numbers, month, and year.

Style for books : Reference Number, Author, first initial followed by last name, title (italics), location and publisher, year, chapter or page numbers (if desired).

Sample format for REFERENCES is as follows :
(for paper)
[3] M. Khalid, S. Omatu, and R. Yusof, "Temperature Regulations with Neural Networks and Alternative Control Shcemes"' IEEE Trans on Neural Networks, Vol. 6, No. 3, pp. 572-582, May, 1995.

(for book)
[4] S. Omatu, M. Khalid, and R. Yusof, Neural-Control and Its Applications,London: Springer-Verlag, 1995.

If your paper is in Bahasa Melayu, please provide an abstract in English.

In the event of the paper being accepted, we will require the camera-steady manuscript to be submitted in a double column format, single-spacing and font of 10 (Times). Include all illustrations in between the text (if possible). An electronic copy should be submitted. We prefer word processing to be done in Microsoft Word. If other word processing software is used, please specify.

C) STYLE FOR ILLUSTRATIONS

Try to include the illustrations in between the text.

Originals for illustrations should be sharp, noise-free and of good contrast.

Each illustration must be numbered such as "Figure 1, Figure 2, etc." and have a meaningful caption at the bottom.

For tables, the caption must be at the top.

On graphs, show only the coordinate axes, or at most the major grid lines, to avoid a dense hard-thread result.

All lettering should be large enough to permit legible reduction of the figure to column width, perhaps as much as 4:1. Typing on figures is not acceptable.

Photographs should be glossy prints, of good contrast and gradation and any reasonable size.

Number each original on the back, or at the bottom of the front, and also indicate the author's name.

Upon acceptance of your paper submit a set of the figures and a list of the captions.

ADVERTISING
To advertise in Journal of IEM, please contact Dimension Publishing Sdn. Bhd. Advertisements that appear in Journal of IEM implies neither endorsement nor recommendation by The Institution of Engineers, Malaysia.

SUBSCRIPTIONS
To subscribe Journal of IEM please contact Dimension Publishing Sdn. Bhd. (address below).

Dimension Publishing Sdn. Bhd. (449732-T)
Unit No. 3A-10, Block F, Phileo Damansara 1
9 Jalan 16/11, Off Jalan Damansara
46350 Petaling Jaya, Selangor Darul Ehsan.
Tel: (603) 7955 5335
Fax: (603) 7955 5773
Email: info@dimensionpublishing.com

PUBLICATION DISCLAIMER
The publication has been compiled by IEM and Dimension with great care and they disclaim any duty to investigate any product, process, service, design and the like which may be described in this publication. The appearance of any information in this publication does not necessarily constitute endorsement by IEM and Dimension. They do not guarantee that the information in this publication is free from errors. IEM and Dimension do not necessarily agree with the statement or the opinion expressed in this publication.

COPYRIGHT
Journal of IEM is the official magazine of The Institution of Engineers, Malaysia and is published by Dimension Publishing Sdn. Bhd. The Institution and the Publisher retain the copyright in all material published in the magazine. No part of this magazine may be reproduced and transmitted in any form, or stored in any retrieval system of any nature without the prior written permission of IEM and the Publisher.

KESAN KUANTITI AGEN PENYERAK DALAM PENCIRIAN SAIZ ZARAH OKSIDA SERAMIK MENGGUNAKAN KAEDAH PEMBELAUAN LASER

A. Muchtar[1], S. M. Tasirin[2] dan S.R.S. Abdullah[2]

[1]*Jabatan Kejuruteraan Mekanik dan Bahan,*

[2]*Jabatan Kejuruteraan Kimia dan Proses, Fakulti Kejuruteraan, Universiti Kebangsaan Malaysia, 43600 UKM Bangi, Selangor*

ABSTRAK

*Kertas kerja ini membincangkan isu kesan penambahan agen penyerak dalam pencirian saiz zarah oksida seramik dengan menggunakan kaedah pembelauan cahaya laser. Adalah diketahui umum bahawa zarah seramik terutamanya daripada serbuk sintetik yang dihasilkan secara kimia dan berada dalam julat saiz di bawah 1 μm atau dikenali sebagai zarah koloid amat mudah membentuk aglomerat. Kehadiran aglomerat dijangka menyukarkan kerja-kerja pencirian saiz sebenar zarah dalam serbuk kerana gumpalan aglomerat akan menyebabkan saiz zarah yang diperolehi menjadi jauh lebih besar daripada saiz diskret zarah yang sebenar. Dalam kajian ini, sejenis agen penyerak komersil, Darvan*7, dikaji keberkesanannya dalam menyerakkan zarah bagi membolehkan pengukuran saiz diskret zarah yang tepat. Kuantiti agen penyerak yang digunakan adalah dalam julat 0 hingga 4 g/L. Dapatan kajian menunjukkan bahawa kuantiti berkesan Darvan*7 adalah 2 g/L sekiranya sampel serbuk yang dikaji ialah serbuk oksida seramik alumina dan zirkonia manakala untuk serbuk magnesia, kuantiti berkesan yang diperolehi ialah 1.2 g/L. Saiz zarah yang diperolehi melalui teknik pembelauan cahaya laser dibandingkan dengan imej visual yang diperolehi menggunakan mikroskop elektron imbasan (SEM). Kajian ini mendapati bahawa dalam pencirian saiz zarah serbuk sintetik seramik yang biasa digunakan dalam fabrikasi komponen seramik termaju, adalah penting untuk mengenalpasti terlebih dahulu kuantiti agen penyerak yang paling berkesan dalam menyahaglomerat zarah sebelum proses pencirian saiz zarah dapat dilakukan dengan tepat.*

Katakunci: *Pencirian Saiz Zarah, Agen Penyerak, Oksida Seramik, Pembelauan Cahaya Laser*

ABSTRACT

*The present paper discusses issues related to the addition of a dispersing agent in the characterisation of particles of oxide ceramics using the laser diffraction technique. It is well known that chemically synthesised powders of sizes below 1 μm or also known as colloids very readily form agglomerates. The presence of agglomerates is expected to hinder the accurate measurement of the size of the particles as the agglomerates may generate an apparent particle size, which is way above the correct discrete size of each individual particle. In this work, the effectiveness of a commercially available dispersing agent, Darvan*7, as used in the measurement of the sizes of the discrete particles, is scrutinised. The amount of Darvan*7 used is in the range of 0 to 4 g/L. The results indicate that for the particle size measurement of alumina and zirconia particles, the optimum amount of Darvan*7 for obtaining the correct particle size is 2 g/L whereas for magnesia particles, the optimum amount is found to be 1.2 g/L. The particle sizes as obtained via the laser diffraction technique are validated by visual inspection under the scanning electron microscope (SEM). This work has shown that in the size characterisation of synthetic ceramics commonly used in the fabrication of advanced ceramic components, it is highly important to first identify the optimum quantity of the dispersing agent that is able to deagglomerate the particles to ensure accuracy in the measurements.*

Keywords: *Particle Size Characterisation, Dispersing Agent, Oxide Ceramics, Laser Diffraction*

PENGENALAN

Kebanyakan sifat kimia, mekanik, fizik dan elektrik bahan adalah bergantung kepada ciri-ciri zarah sesuatu bahan tersebut [1-2]. Antara sifat yang dipengaruhi sepenuhnya oleh ciri-ciri zarah bahan ialah seperti kestabilan produk, kereaktifan kimia, kelegapan dan kekuatan bahan. Oleh itu, pencirian saiz dan bentuk zarah amat diperlukan atas tujuan terutamanya dalam penyelidikan di industri bagi memastikan mutu sesuatu barangan produk terjamin. Secara teknikalnya, sistem serbuk bersaiz submikron menjadi semakin penting semenjak abad lepas. Kebanyakan industri dan metodologi pengukuran saiz zarah menunjukkan perkembangan yang sejajar iaitu yang selaras dengan kepentingan kajian ke atas zarah seni yang menyumbangkan kepada peningkatan kualiti bahan yang hendak dimajukan [3]. Di samping itu, dengan wujudnya perkembangan dalam teknologi pemprosesan, telah terbukti bahawa pengukuran saiz zarah secara tepat dan automatik adalah amat diperlukan. Oleh itu, pengetahuan mengenai saiz zarah dan taburan saiz pada julat 0.1 hingga 1000 mm merupakan asas dalam bidang industri pemprosesan [4].

Dalam pembikinan komponen seramik termaju, penggunaan bahan mentah yang terkawal dari segi ketulenan dan saiz zarahan adalah wajib. Oleh yang demikian, pilihan terbaik bagi bahan mentah untuk fabrikasi seramik ialah

001-005·kesan kuantiti 9/20/05 11:54 AM Page 2

serbuk seramik yang dihasilkan secara sintetik [5]. Untuk fabrikasi komponen seramik struktur, seringkali objektif pembikinan ialah untuk menghasilkan komponen yang berbijian halus kerana kajian terdahulu telah membuktikan peningkatan prestasi mekanik komponen sedemikian berbanding komponen yang berbijian kasar [6-9]. Salah satu syarat bagi menghasilkan komponen berbijian halus yang wajib dipatuhi ialah penggunaan bahan mentah berkoloid yang saiznya kurang daripada 1 μm [10-11]. Walau bagaimanapun, sebelum pemprosesan serbuk seramik ini boleh terus dilakukan, langkah asas yang perlu dijalankan ialah mencirikan saiz zarah serbuk sebagai sebahagian daripada langkah kawalan kualiti terawal bagi memastikan penghasilan komponen yang berprestasi tinggi.

Akur dengan masalah pengaglomeratan zarah berkoloid, kajian ini bertujuan untuk mendapatkan kuantiti agen penyerak optimum yang paling berkesan dalam menyerakkan zarah beberapa jenis serbuk oksida seramik. Ini bagi membolehkan pencirian saiz zarah yang tepat dan pantas dengan menggunakan teknik pembelauan cahaya laser. Teknik ini merupakan sebuah teknik terbaru dan dijangka tercanggih dalam kerja-kerja pencirian saiz zarah. Kajian literatur mendapati walaupun penggunaan teknik ini amat meluas dan merangkumi pelbagai bahan kajian yang berbeza contohnya pencirian pigmen organik [12], pencirian endapan di muara sungai [13] serta pencirian ampaian spora *Bacillus* [14], artikel dalam jurnal mengenai penggunaan teknik ini masih kurang dan sukar diperolehi terutama dalam pencirian zarah bahan seramik.

METODOLOGI

Dalam kerja penyelidikan ini, empat jenis serbuk seramik berketulenan tinggi dan berbijian halus dipilih sebagai bahan kajian. Ini termasuklah dua jenis serbuk seramik alumina berketulenan tinggi iaitu TMDAR (Taimei Chemicals, Japan) yang berketulenan 99.99% dan AL160SG-1 (Kyoritsu Chemicals, Japan) yang berketulenan 99.8 %. Selain itu, serbuk oksida seramik yang dikaji ialah serbuk magnesia berketulenan 99.95% (Strem Chemicals, US) dan serbuk zirkonia berketulenan 99.95% (Strem Chemicals, US).

Pengabaian langkah persampelan dalam analisis teknologi serbuk akan mengakibatkan keputusan yang tidak jitu. Adalah amat penting bahawa setiap sampel yang dipilih untuk analisis adalah mewakili keseluruhan sampel serbuk seramik yang dikaji. Oleh itu, bagi tujuan analisis yang berkesan, kaedah persampelan yang disarankan oleh Allen [15] dipatuhi.

Gabungan media dan agen penyerakan yang bersesuaian memainkan peranan yang penting dalam pencirian saiz zarah yang tepat [16]. Dalam kajian ini, sejenis agen penyerak komersil iaitu Darvan*7 (R.T. Vandervilt Co. Inc., US) digunakan di mana bahan utama penyerak ini ialah sodium polimetaklarat. Agen penyerak jenis cecair ini diharapkan dapat bertindak secara berkesan dengan serbuk seramik oksida yang dikaji tanpa menimbulkan kesan-kesan yang boleh menyebabkan gangguan kepada pemerhatian saiz zarah. Penggunaan agen penyerak ini juga bertujuan mengelakkan tindak balas kimia di antara zarah seramik oksida dengan agen dan medium penyerakan. Dalam kajian ini, air suling digunakan sebagai medium penyerakan serbuk seramik ketika ujian dijalankan. Agen penyerak Darvan*7 dicampurkan ke dalam air suling tadi pada kuantiti yang berlainan iaitu 0.0, 1.0, 1.2, 1.4, 1.6, 1.8, 2.0, 2.5, 3.0, 3.5 dan 4.0 g/L.

Alat yang digunakan untuk mencirikan saiz zarah dalam kajian ini ialah Malvern Particle Sizer S (SiberHegner) sementara prosedur piawai yang dipilih untuk digunapakai ialah prosedur ASTM C 1070 – 86 [17]. Alat ini terdiri daripada alat pemancar laser, kanta yang telah dikaliberasikan dan komputer analisis yang dilengkapi dengan perisian bagi pengiraan taburan saiz zarah sampel. Pengukuran dilakukan melalui cahaya laser helium-neon berkuasa rendah yang dibelaukan oleh kehadiran zarah serbuk, menggunakan satu siri susunan optik kanta (Fourier) yang terdapat di dalam alat ini. Susunan optik disambung kepada alat pengesan yang akan merekodkan arus yang setara dengan keamatan cahaya laser yang dibelaukan lalu jatuh ke atasnya. Sudut belauan cahaya adalah berkadar songsang dengan saiz zarah. Rajah 1 menerangkan prinsip pengukuran menggunakan alat pembelau laser ini sementara Rajah 2 pula menunjukkan ilustrasi skematik keseluruhan sistem alat pencirian saiz zarah Malvern Mastersizer S. Keputusan saiz zarah diperolehi dengan pantas melalui penggunaan sebuah perisian khusus untuk alat ini.

KEPUTUSAN DAN PERBINCANGAN

Perolehan Kepekatan Optimum Agen Penyerak

Rajah 3 menunjukkan kesan kuantiti agen penyerak terhadap nilai min saiz zarah yang diperolehi menggunakan alat Malvern Mastersizer S yang berkonsepkan pembelauan cahaya laser. Untuk setiap jenis serbuk oksida seramik yang dikaji, agen penyerak dicampurkan dalam kuantiti yang berlainan. Setiap larian ujikaji akan menghasilkan taburan saiz zarah di mana nilai saiz min yang diperolehi kemudiannya diplotkan melawan kepekatan agen penyerak seperti yang tertera dalam Rajah 3.

Dapatan kajian mendapati larutan agen penyerak Darvan*7 dengan kepekatan 2.0 g/L paling berkesan dalam menyahaglomerat zarah kesemua jenis serbuk seramik kecuali bagi serbuk magnesia di mana kepekatan berkesan yang

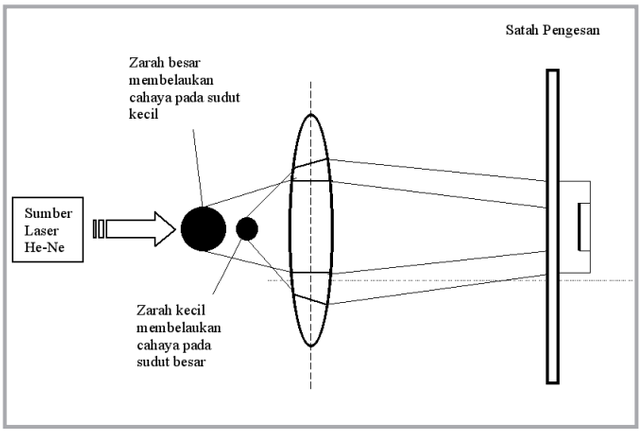

Rajah 1: Prinsip pengukuran saiz zarah menggunakan teknik pembelauan cahaya laser

diperolehi ialah 1.2 g/L. Kepekatan berkesan yang dimaksudkan ialah apabila larutan agen penyerak atau pemerai yang digunakan berupaya menjerap pada keseluruhan permukaan zarah dan bertindak meningkatkan daya penolakan

001-005·kesan kuantiti 9/20/05 11:54 AM Page 3

sesama zarah melalui pengecasan elektrik. Nilai kepekatan berkesan ini dikenalpasti apabila bacaan nilai min saiz zarah adalah terendah kerana dijangkakan pada ketika ini, zarah-zarah tunggal dan bukannya aglomerat yang wujud di dalam ampaian.

Mengikut prinsip kendalian alat Malvern Mastersizer S, penentuan saiz zarah bergantung kepada pembelauan cahaya yang sampai ke satah pengesan (Rajah 1). Zarah yang kecil akan membelaukan cahaya pada sudut yang besar sementara zarah yang besar akan membelaukan cahaya pada sudut yang

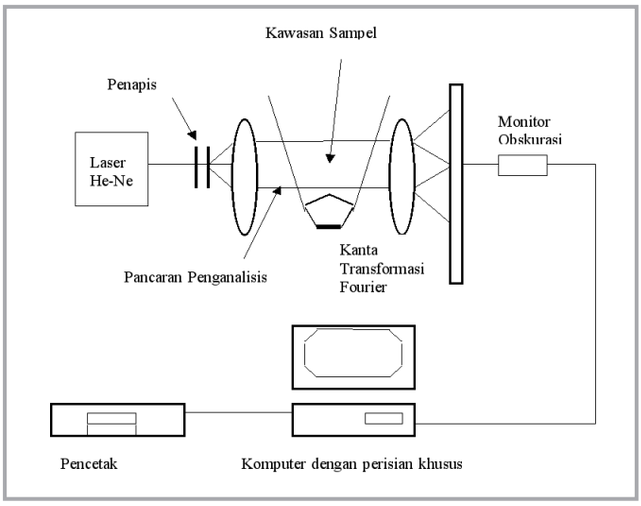

Rajah 2: Ilustrasi skematik sistem Malvern Mastersizer S

kecil. Dengan demikian, perolehan saiz min yang terkecil boleh diambil kira sebagai manifestasi kemampuan agen penyerak menyerakkan zarah dalam ampaian kerana pada situasi ini, zarah berkemungkinan besar hadir sebagai unsur diskret dalam ampaian menyebabkan cahaya laser terbelau pada sudut yang besar. Sebaliknya, perolehan saiz min yang lebih besar menandakan zarah telah bergumpal menyebabkan cahaya laser terbelau pada sudut yang kecil lalu memberikan keputusan saiz zarah yang kurang tepat. Keputusan ini menepati hasil kajian oleh Osamu et al.[16] yang mendapati nilai saiz zarah titanium dioksida yang mereka kaji menurun setelah sampel melalui proses penyahaglomeratan secara mekanik.

Pengagglomeratan Zarah Melalui Tindakan Elektrostatik

Agen penyerak, Darvan*7 yang digunakan dalam kajian ini, yang mana bahan utama penyerak ini ialah sodium polimetaklarat, boleh dikategorikan sebagai satu polimer anion yang bercas negatif. Polimer yang tinggi jisim molekulnya ini mampu untuk menjerap ke permukaan gumpalan seramik oksida yang bercas positif disebabkan oleh tindakan elektrostatik melalui mekanisma penjerapan dan peneutralan cas [18]. Hal ini bukan sahaja dapat meneutralkan cas positif dalam kawasan terjerap tetapi juga menyediakan cas negatif tambahan untuk cas positif yang lain pada permukaan serbuk tersebut. Keadaan ini akan memudahkan penyahaglomerat antara zarah secara tolakan elektrostatik. Pada kuantiti agen penyerak yang optimum, polimer ini akan menepu kepada permukaan serbuk seramik oksida sehingga cas bersih pada zarah serbuk diterbalikkan daripada positif kepada negatif menerusi penjerapan berlebihan ion lawan. Hasilnya, serbuk seramik oksida akan

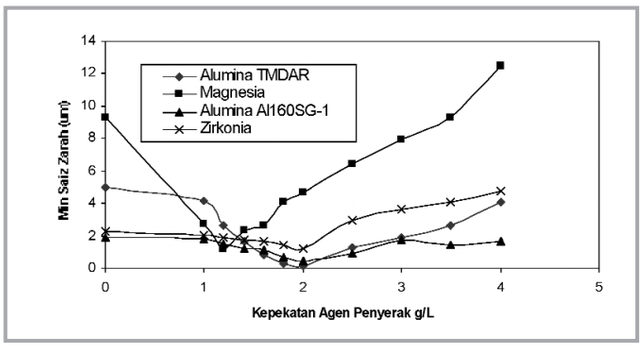

Rajah 3: Kesan kuantiti agen penyerak dalam menentukan saiz zarah serbuk seramik

distabilkan atau dinyahalomeratkan kerana penepuan cas bersih negatif pada permukaan serbuk akan mengakibatkan serbuk-serbuk tersebut menolak antara satu sama lain. Dan sekiranya dos agen penyerak yang melebihi kuantiti optimumnya terus ditambahkan kepada serbuk seramik oksida yang telah dinyahaglomeratkan, kation yang terdapat pada agen penyerak Darvan*7 boleh berperanan untuk meneutralkan cas bersih negatif serbuk seramik dan membolehkan serbuk-serbuk ini kembali bergumpal disebabkan tarikan elektrostatik. Hal ini menerangkan mengapa kesemua susuk min saiz zarah meningkat setelah melepasi tahap optimum bagi kesemua jenis serbuk yang dikaji, seperti yang diperolehi dalam Rajah 3.

Dari keputusan kajian yang diperolehi (Rajah 3), kuantiti optimum agen penyerak bagi serbuk seramik alumina oksida (Al_2O_3) dan zirkonia oksida (Z_rO_2) adalah 2.0 g/L, manakala kuantiti optimum bagi serbuk seramik magnesia (MgO) pula adalah lebih rendah iaitu hanya 1.2 mg/L. Perbezaan ini boleh dijelaskan dengan keadaan nombor pengoksidaan pada setiap serbuk seramik yang dikaji. Serbuk seramik magnesia, alumina dan zirkonia masing-masing mempunyai nombor pengoksidaan +2, +3 dan +4. Oleh kerana, alumina dan zirkonia mempunyai nombor pengoksidaan yang lebih tinggi berbanding serbuk magnesia, maka kuantiti optimum agen penyerak yang lebih tinggi diperlukan bagi menjerap dan meneutralkan cas-cas pada pada permukaan serbuk-serbuknya berbanding dengan serbuk magnesia.

Taburan Saiz Zarah Pada Kepekatan Optimum Agen Penyerak

Salah satu fungsi utama alat Malvern Mastersizer S yang mampu dilakukan dengan pantas ialah perolehan terperinci taburan saiz zarah sampel serbuk yang diperolehi dalam masa beberapa saat sahaja. Berbanding teknik pencirian saiz zarah lainnya yang dianggap lazim, teknik terbaru ini jauh lebih pantas dan cekap di samping mampu memberikan jawapan yang tepat [19-20]. Rajah 4 dan 5 menunjukkan taburan zarah serbuk pada kepekatan optimum agen penyerak seperti yang diperolehi dalam kajian ini. Berdasarkan kepada Rajah 4, lebih kurang 92% saiz zarah Alumina (TM-DAR) berada dalam julat 0.05-0.23 µm, manakala 80% saiz zarah Alumina (Al 160SG-1) berada dalam julat 0.05-0.58 µm. Di samping itu, hampir 90% saiz zarah Magnesia (Stremchemicals) berada dalam julat 0.11-1.68 µm dan lebih dari 95% saiz zarah Zirkonia (Stremchemicals) berada dalam julat 0.05-1.95 µm, seperti yang ditunjukkan dalam Rajah 5.

001-005·kesan kuantiti 9/20/05 11:54 AM Page 4

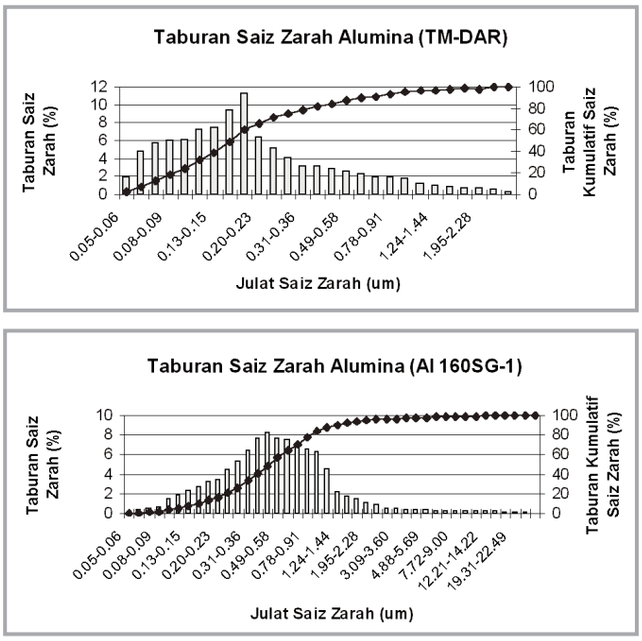

*Rajah 4: Taburan saiz zarah serbuk alumina TMDAR dan AL160SG-1 seperti yang diperolehi melalui teknik pembelauan cahaya laser pada kuantiti Darvan*7 yang optimum iaitu 2 g/L*

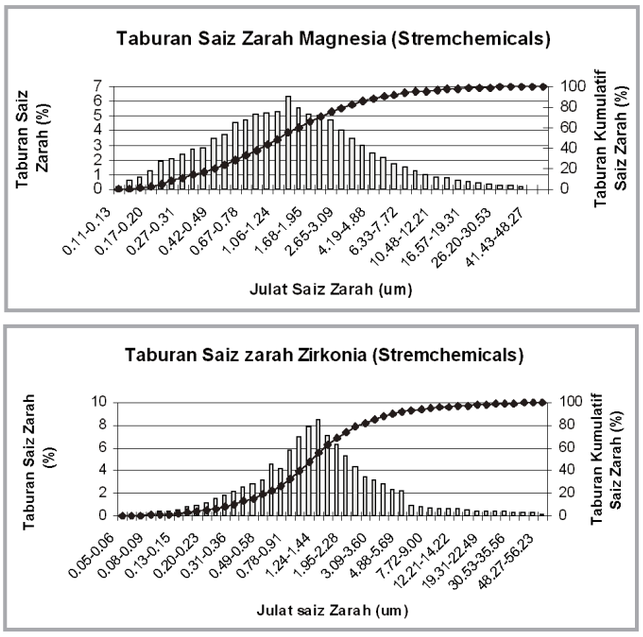

*Rajah 5: Taburan saiz zarah serbuk magnesia dan zirkonia seperti yang diperolehi melalui teknik pembelauan cahaya laser pada kuantiti Darvan*7 yang optimum iaitu 2 g/L bagi serbuk zirkonia dan 1.2 g/L bagi serbuk magnesia*

Imej Zarah Menggunakan SEM

Sebagai data tambahan kepada kajian ini, visual zarah serbuk yang dikaji turut diperolehi melalui penggunaan mikroskop imbasan elektron atau SEM. Rajah 6 dan 7 memaparkan imej SEM bagi serbuk alumina, magnesia dan zirkonia yang digunakan dalam kajian ini. Perolehan imej SEM yang jelas dan terfokus dengan baik bagi kedua-dua jenis serbuk alumina didapati agak mudah. Walau bagaimanapun, penulis menghadapi banyak masalah mendapatkan imej yang jelas bagi serbuk magnesia dan zirkonia, terutama bagi

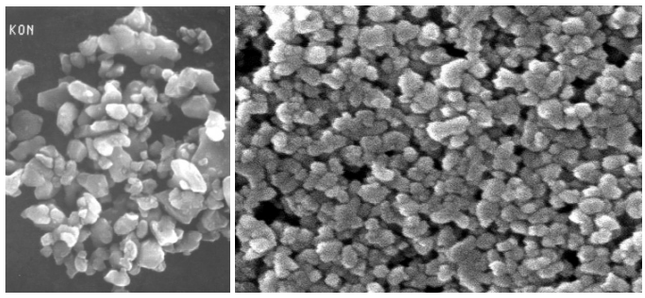

Rajah 6: Mikrograf SEM menunjukkan bentuk dan saiz zarah alumina AL160SG-1 (kiri) dan TMDAR (kanan)

mendapatkan imej pada magnifikasi yang tinggi. Secara umumnya, kerja-kerja pensaizan zarah dijangka lebih mudah dan lebih tepat bilamana imej zarah diperolehi dengan jelas. Untuk zarah kedua-dua serbuk alumina, saiz zarah yang kelihatan menepati keputusan saiz zarah seperti yang diperolehi daripada teknik pembelauan cahaya laser pada kuantiti agen penyerak yang optimum.

Walau bagaimanapun, teknik SEM didapati sukar untuk mencirikan saiz zarah bila mana imej SEM yang jelas tidak dapat diperolehi seperti halnya untuk serbuk magnesia dan zirkonia (Rajah 7). Zarah kelihatan bergumpal sehingga menyukarkan perolehan saiz sebenar zarah. Di samping itu, serbuk magnesia dan zirkonia seperti yang digunakan dalam kajian ini tidak berupaya dikaji pada magnifikasi yang tinggi kerana imej SEM akan menjadi kabur dan tidak terfokus. Oleh itu, dalam kes sebegini, jelas teknik pembelauan cahaya laser merupakan teknik pencirian saiz zarah yang lebih mudah.

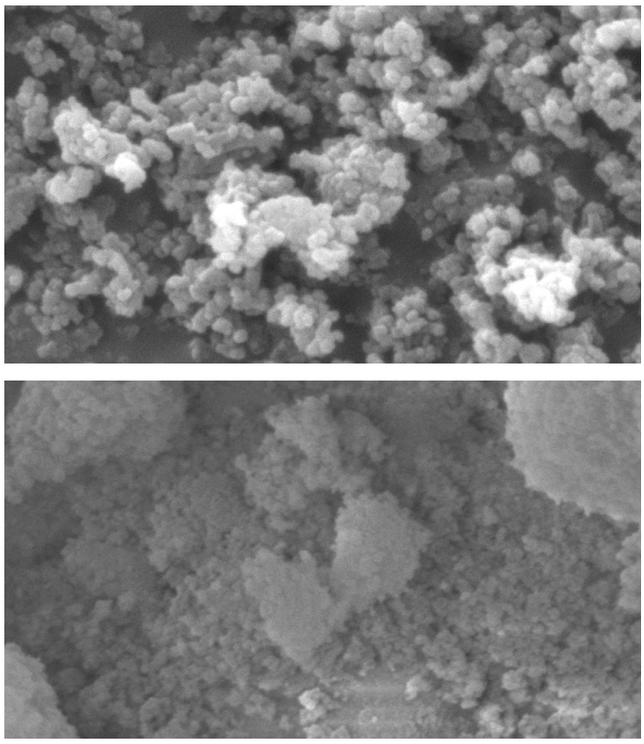

Rajah 7: Mikrograf SEM menunjukkan bentuk dan saiz zarah magnesia (atas) dan zirkonia (bawah)

KESIMPULAN

Kajian ini telah menunjukkan betapa pentingnya mengenalpasti kepekatan optimum atau paling berkesan dalam menyerakkan

001-005·kesan kuantiti 9/20/05 11:54 AM Page 5

zarah dalam ampaian sehingga zarah mampu wujud sebagai individu diskret dan tidak bergumpal membentuk aglomerat. Ini bagi memastikan keputusan ujikaji pencirian saiz zarah seramik oksida secara pembelauan cahaya laser seperti yang dilaksanakan dalam kajian ini adalah tepat dan bukan sebaliknya. Keputusan nilai saiz zarah yang diperolehi telah dibandingkan dengan imej visual zarah yang diperolehi melalui teknik mikroskop elektron imbasan,atau SEM.

Dalam kajian ini, kuantiti agen penyerak Darvan *7 yang optimum bagi pencirian saiz zarah alumina AL160SG-1 dan TMDAR serta zirkonia (Strem Chemicals) didapati ialah pada 2g/L sementara untuk serbuk magnesia (Strem Chemicals), kuantiti agen penyerak yang optimum ialah 1.2 g/L.

PENGHARGAAN

Penulis merakamkan setinggi-tinggi penghargaan kepada Universiti Kebangsaan Malaysia dan Kerajaan Malaysia atas sokongan kewangan bagi kajian ini melalui geran IRPA 03-02-02-0047. Sumbangan pelajar L. Glass dalam mendapatkan data penyelidikan juga amat dihargai. ■

RUJUKAN

[1] L. Guoqiang, Z. Ti dan P. Su-Seng, Analytical modeling of particle size and cluster effect on particulate-filled composite, *Materials Science and Engineering*, A271, ms 43 –52, 1999

[2] J.E.Tabiason, G.S. Johnson, P.K. Westerhoff dan B. Vigneswaran, Particle size and chemical effects on contact filtration performance, *Journal of Environmental Engineering*, **Vol 119 (3)**, ms 520 – 539, 1993

[3] M.J. Groves, The applications of particle characterisation methods to submicron dispersions and emulsions, Modern Methods of Particle Size Analysis, Howard G Barth (pnyt.), John Wiley & Sons Inc., New York, 1984

[4] P.E. Plantz, Particle size measurement from 0.1 to 1000 μm, based on light scattering and diffraction, Modern Methods of Particle Size Analysis, Howard G. Barth (pnyt.), John Wiley & Sons Inc., New York. 1984

[5] D. Segal, Chemical Preparation of Powders, *Materials Science and Technology: 17A*, ms 69-98, 1996

[6] B. Mussler, M.V. Swain dan N. Claussen, Dependence of fracture toughness of alumina on grain size and test technique, *J. Am. Ceram. Soc.,* **65 (11)**, ms 566 – 572, 1982

[7] P, Chantikul, S.J. Bennison dan B.R. Lawn, Role of grain size in the strength and R-curve properties of alumina, *J. Am. Ceram. Soc.,* **73 (8)**, ms 2419 – 2427, 1990

[8] N. Miyahara, Y. Mutoh, K. Yamaishi, K. Uematsu dan M. Inoue, The effects of grain size on strength, fracture toughness, and static fatigue crack growth in alumina. In Grain Boundary Controlled Properties of Fine Ceramics, K. Ishizaki, K. Niihara, M. Isotani dan R.G. Ford (penyunting), JFCC Workshop Series: Materials, Processing and Design, ms 125 – 136, Elsevier Science Publishers Ltd, 1992

[9] A. Muchtar dan L.C. Lim, Indentation fracture toughness of high purity submicron alumina, *Acta Materialia*, **46**, ms 1683 – 1690, 1998

[10] J. Reed, Principles of Ceramics Processing, ed ke-2, John Wiley & Sons Inc, 1995

[11] A. Muchtar, Sintering Characteristics and microstructures of colloidally processed alumina, *Jurnal Kejuruteraan,* **11 (2)**, ms 3 – 12, 1999

[12] M. McGravey, D. McGregor dan R.B. McKay, Particle size analysis by laser diffraction in organic pigment technology, *Progress in Organic Coatings,* **31**, ms 223 – 228, 1997

[13] O.A. Mikkelsen dan M. Pejrup, The use of a LISST-100 laser particle sizer for in-situ estimates of floc size, density and settling velocity, *Geo-Marine Letters,* **20**, ms 187 – 195, 2001

[14] R.G.K. Leuschner, A.C. Weaver dan P.J. Lillford, Rapid particle size distribution analysis of Bacillus spore suspensions, *Colloids and Surfaces B: Biointerfaces*, **13**, ms 47 – 57, 1999

[15] T. Allen, Particle Size Measurement, ed ke-4, Chapman and Hall, London, 1990

[16] H. Osamu, N. Kenji, N. Makio dan T. Junichiro, Experimental analysis of sample preparation conditions for particle size measurement, *Powder Technology*, **100**, ms 61 – 68, 1998

[17] ASTM C 1070 – 86, Standard Test Method for Determining Particle Size Distribution of Alumina or Quartz by Laser Light Scattering, Reapproved 1992

[18] G. Tchobanoglous, Wastewater engineering treatment, disposal, reuse. Ed. ke-2. New York: Tata McGraw-Hill Book Company, 1990

[19] Andanastuti Muchtar, Siti Masrinda Tasirin dan Murni Melati Ahmad, Analisis Perbandingan Pengukuran Saiz Zarah Kaolin dengan Menggunakan Alat Malvern Mastersizer S dan Kaedah Sedimentasi, Pascasidang Penyelidikan dan Pengembangan 1999, Jabatan Kejuruteraan Mekanik dan Bahan, UKM, ms 41-46, 1999.

[20] Andanastuti Muchtar, Siti Masrinda Tasirin dan Abdullah Tahir, Pencirian Saiz Zarah Alumina: Perbandingan di antara Kaedah Lazim dan Teknik Pembelauan Cahaya Laser. Prosidang abstrak Seminar Fizik Kebangsaan 2000, 7-8 Nov 2000, Universiti Malaysia Sabah, ms 2, 2000

006-012·analysis/ iem referees 9/20/05 11:59 AM Page 6

ANALYSIS OF DESIGN PARAMETER EFFECTS ON VIBRATION MODES OF A MOTORCYCLE DRUM BRAKE AND BRAKE SHOE USING THE FINITE ELEMENT METHOD

Zahrul Fuadi and Zaidi Mohd. Ripin

Faculty of Engineering, Universiti Sains Malaysia, Seri Ampangan, 14300 Nibong Tebal, Seberang Perai Selatan, Pulau Pinang

ABSTRACT

The natural frequencies and vibration modes of the particular motorcycle drum brake and brake shoe have been determined using the finite element method. The results show that the drum brake has 42 mode shapes in the frequency range of 100 Hz to 12 kHz. Most of the mode shapes occurred in pair (repeated root). The brake shoe is found to have 10 mode shapes in the frequency range analysed. Parametric analysis has also been conducted to study the effect of various design parameters to the occurrence of natural frequency of the model and the results have been presented in the frequency response function. The results show high modal density in the frequency range of 1500 – 2000 Hz and 5600 – 6400 Hz. Modal density of the drum can be reduced by increasing its stiffness for the low frequency range and increasing flange stiffness for the high frequency range. These results indicate important parameters for the design and prevention of drum brake noise.

Keywords: *Drum Brake, Noise, Vibration, Finite Element Method, Design*

INTRODUCTION

Vibration of the components of the drum brakes when braking causes noise to be emitted. The motorcycle drum brake consists of two major components, the drum and the brake shoe. The vibration of these two components are related to the squeal noise generated by the motorcycle drum brake which is related to the perceived quality of the motorcycle and noise pollution. Noise emanating from brakes has been studied as early as 1935 when Lamarque [1] collected the experience of manufacturers and operators on the cause and prevention of squeal in drum brakes. There have been a considerable number of works on drum brake squeal and this has been collated in a relatively comprehensive overview by Crolla and Lang in 1991 [2]. Since then there have been a remarkable improvement in the understanding on the cause of drum brake squeal particularly when the problem is treated as a stability problem associated with the complex eigenvalue of the brake system [3,4,5]. One of the latest works by Hamabe [6] clearly showed the effect of modal intensity and the influence of various geometric parameters in drum brake squeal analysis.

The effect of various parametric designs has also been highlighted in the previous studies of drum brake squeal. The effect of suspension system on the drum brake noise has been studied by Fieldhouse [7]. The importance of drum brake back plate on the drum brake squeal has also been reported by many researchers [6,7,8].

The present work attempts to identify the design parameter of a motorcycle drum brake which influence its natural frequency in particular those parameters which can reduce the modal intensities and the diametral mode of the drum. A typical drum brake of a light motorcycle (110 cc) of a Malaysian made is used in this analysis. The importance of this work lies on the fact that unlike disc, a drum brake assembly is relatively more complex and asymmetry exists due to its design. This work will highlight the effect of such geometry on its overall natural frequencies and mode shapes.

DESCRIPTION OF THE MODEL

A motorcycle drum brake chosen for the analysis is shown in Figure 1. The rear wheel motorcycle drum brake consists of a drum brake, a pair of shoes, actuator, and brake linings. The drum itself was attached with the spokes and two bearings.

Because the brake system is complex, it is decided to consider only the drum for the analysis. The specification of

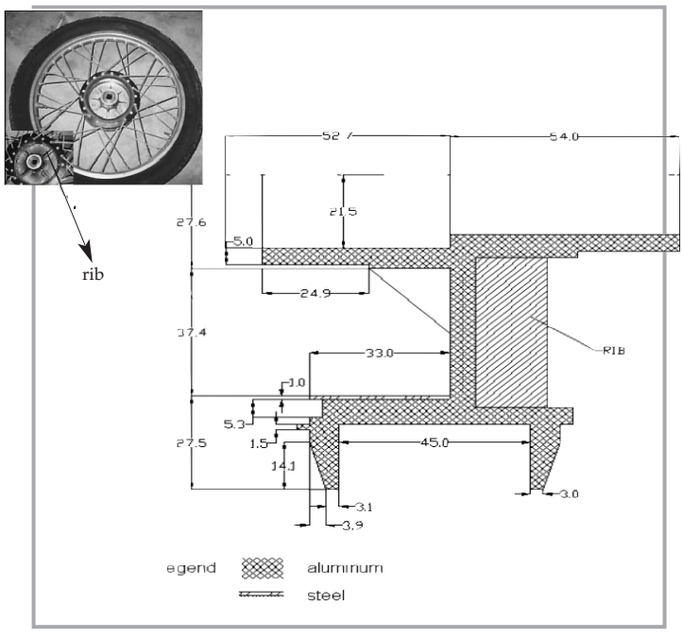

Figure 1: Motorcycle drum brake and its cross-sectional area (dimension in mm)

Table 1: Specifications of the drum brake and brake shoe

Drum Brake			Brake Shoe		
	Drum	Friction Steel		Aluminum back plate	Lining
Modulus Elasticity, E_d, E_s	69 GPa	207GPa	Modulus of elasticity, E	69 GPa	8 GPa
Diameter, d_d, d_s	136 mm	130 mm			
Drum Width, l_d, l_s	30 mm	33 mm	Density, ρ	2720 kg/m³	2500 kg/m³
Density, ρ_d, ρ_s	2720 kg/m³	7520 kg/m³			

006-012·analysis/ iem referees 9/20/05 11:59 AM Page 7

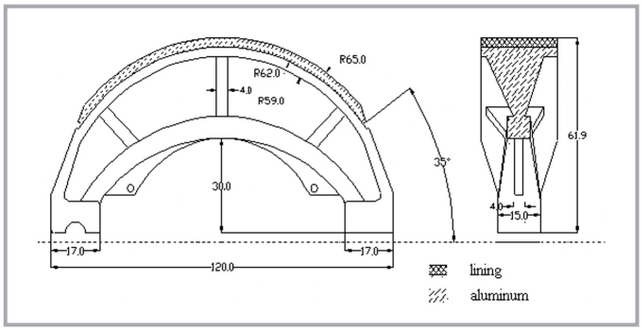

Figure 2: Motorcycle brake shoe and its cross-sectional area (dimensions in mm)

the drum is shown in Table 1. The drum brake is made of cast aluminum alloy and friction part of the drum in contact with the lining is made of cylindrical steel. The motorcycle drum brake is shown in Figure 2. The shoe back plate is made of the same material as that of the drum brake. The specifications of the drum brake and brake shoe are shown in Table 1.

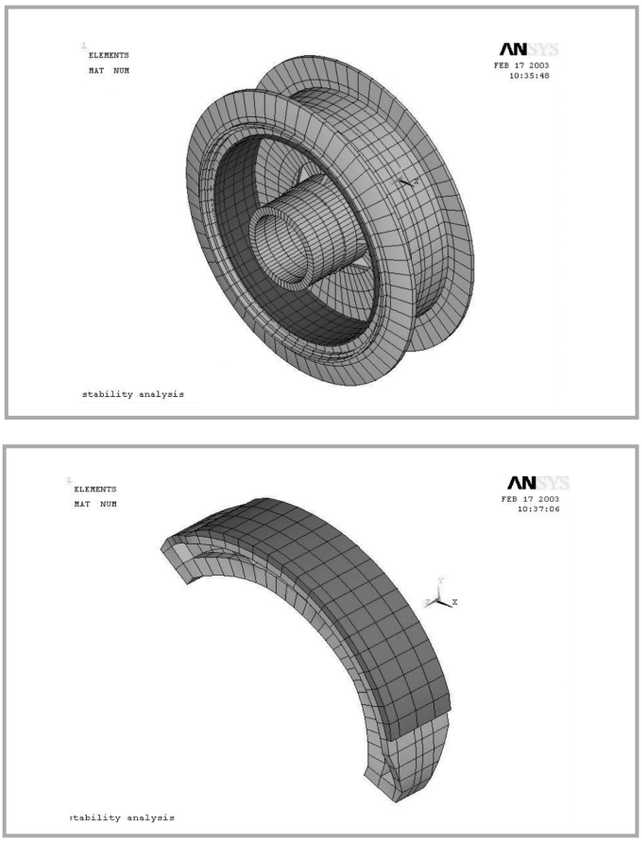

Figure 3: 3-D finite element model; (a) drum, and (b) brake shoe

FINITE ELEMENT MODEL

A three-dimensional finite element model of the drum brake and brake shoe are shown in Figure 3. The models consist of hexahedral elements with eight nodes. The definition of nodes and elements are created using ANSYS 6.0 finite element solver package.

The following assumptions are considered for the analysis:

1. The spokes and the spokes holes are neglected.
2. The bearings are excluded.
3. Details produced by casting process are neglected.

Modal Analysis of the Drum

Natural frequencies of the drum brake are calculated by modal analysis option available in ANSYS 6.0 software. The element type used is 8-node isoperimetric brick known as SOLID45 in ANSYS nomenclature. The modal analysis was conducted in the range of frequency from 100 Hz to 12 kHz. There are 42 mode-shapes occurred in the specific frequency range which indicates that the modal density of the drum brake is high as it has many modes in a small frequency band. It can also be observed as well that drum brake has repeated roots where two modes have the same mode shape but different modal frequency. The repeated roots occur at the structure that is axially symmetrical with identical frequency for both roots. But in the case of this particular drum brake, the repeated roots have different frequencies. This is caused by the presence of back plate ribs and will be shown later in this paper.

Mode shape of the drum can be classified into several groups according to geometrical mode shapes, such as diametral modes and flange modes. The first diametral mode shapes occurred at frequencies of 1170 Hz. The second diametral mode of the drum occurred at frequencies of 1955 Hz and 2233 Hz. The third diametral mode shape of the drum occurred at a frequency of 5213 Hz. The fourth drum diametral mode shapes occurred at frequencies of 8766 Hz and 8799 Hz. Another set of third diametral mode shapes of the drum occurred at frequencies of 11230 Hz and 11055 Hz.

Flange mode shapes dominate the mode shape of the drum brake with 25 mode shapes out of 42 mode shapes. Flange mode shapes occurred at frequencies of, among others, 2873 Hz, 3066 Hz, 3492 Hz, 4341 Hz, 4367 Hz, 5699 Hz, 5967 Hz, 6187 Hz, 7049 Hz, 7054 Hz, 7420 Hz, 7619 Hz, 8350 Hz, 8766 Hz, 9087

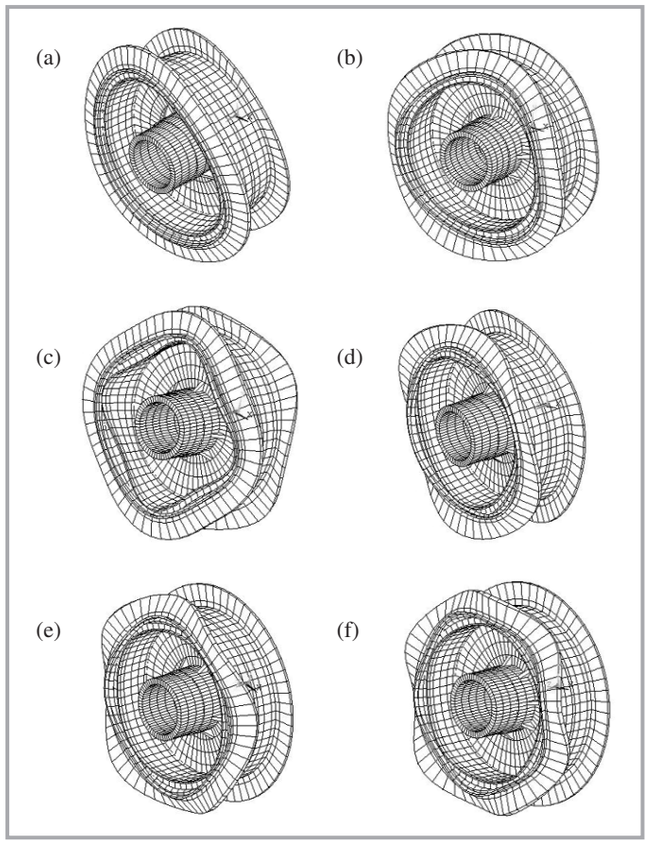

Figure 4: (a) Second diametral mode shape at 1955 Hz, (b) Third diametral mode shape at 5213 Hz, (c) Fourth diametral mode shape at 11203 Hz, (d) Fourth flange mode shape at 5699 Hz, (e) Fifth flange mode shape at 7054 Hz, and (f) Sixth flange mode shape at 8766 Hz

006-012·analysis/ iem referees 9/20/05 11:59 AM Page 8

Hz, 9210 Hz, 10603 Hz, 10604 Hz, and 10974 Hz. Some of the mode shapes are presented in Figure 4.

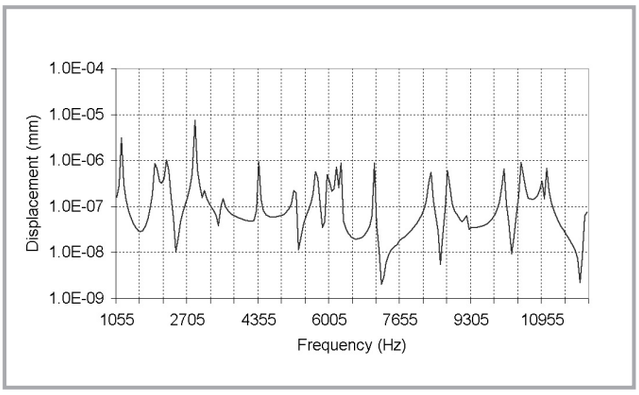

Figure 5: Frequency response function of the drum brake (in radial direction)

Other mode shape include back plate mode shapes which occurred at frequencies of 1369 Hz and 2873 Hz and cylindrical mode shapes occurred at frequencies of 2873 Hz, 10061 Hz, 10476 Hz, and 11970 Hz. The frequency response function of the drum brake is shown in Figure 5.

Classification of the mode shape according to the frequency range is given in Table 2. The most numbers of the mode shapes occurred in the frequency range between 10 kHz and 11 kHz with 7 mode shapes.

Frequency range (Hz)	Number of mode shapes
1000 – 2000	5
2000 – 3000	3
3000 – 4000	3
4000 – 5000	2
5000 – 6000	5
6000 – 7000	1
7000 – 8000	5
8000 – 9000	6
9000-10000	2
10000-11000	7
11000-12000	3
Total	42

Table 2: Classifications of mode shapes according to frequency range

Modal Analysis of the Shoe

Modal analysis of the brake shoe is conducted in the frequency range of 100 Hz and 12000 Hz. The analysis resulted in 10 mode shapes of the brake shoe. The mode shape can be grouped into bending mode shapes and twisting mode shapes. The bending modes are those that involve major deformation in the radial direction while the torsion modes are when the displacement involves major displacement in the axial direction.

There are 5 mode shapes that can be categorised as bending mode shapes and 4 mode shapes as the twisting mode shapes. The bending mode shapes occurred at frequencies of 358 Hz, 2141 Hz, 6485 Hz, 10253 Hz, and 10986 Hz. The twisting mode shapes occurred at frequencies of 927 Hz, 2690 Hz, 5937 Hz, and 9323 Hz. Several brake shoe mode shapes are given in Figure 6. The frequency response function of the brake shoe is given in Figure 7.

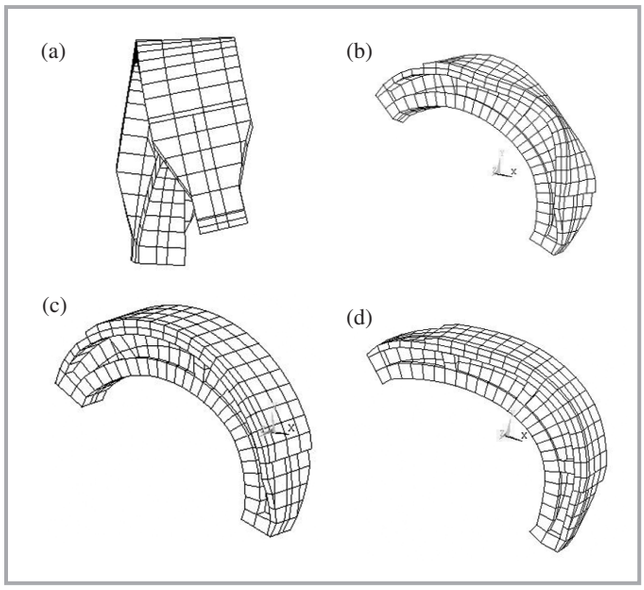

Figure 6: (a) Twisting mode at 2690Hz, (b) twisting mode at 9323Hz, (c) bending mode at 2141Hz, and (d) bending mode at 10984Hz

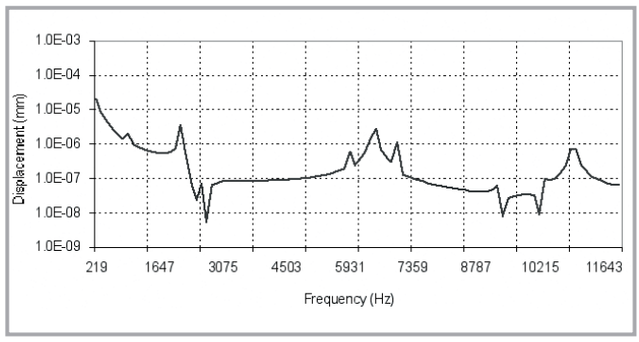

Figure 7: Frequency response function of the brake shoe (in radial direction)

PARAMETRIC ANALYSIS

Parametric analysis is conducted to find out the design parameters effect for natural frequencies, mode shape and modal density of the model. The interested parameters for the analysis are stiffness of the drum back plate ribs, flanges, shoe, as well as flange thickness.

Effect of Drum Back Plate Ribs

The particular motorcycle drum brake used in this analysis has four ribs at its back plate ribs. The back plate ribs of the drum brake are the part where torque from the sprocket is applied. The influence of the ribs to the overall mode shape of the drum brake is analysed by conducting the modal analysis after removing the ribs. The results showed that the frequencies of each of the repeating roots (mode shape pair) become identical to each other. For example, one of the mode shape pair have the frequencies of 1955 Hz and 2233 Hz. As the ribs are removed, this mode shape frequency and its pair occurred at a frequency of 1927 Hz. The comparison of the frequency response function for this mode pair with and without the presence of back plate ribs is given in Figure 8. With the presence of rib (indicated by continuous line) there are two peaks for the same mode shape, at frequencies of 1955 Hz and 2233 Hz. As the ribs are removed (indicated by dotted line), there

006-012·analysis/ iem referees 9/20/05 12:00 PM Page 9

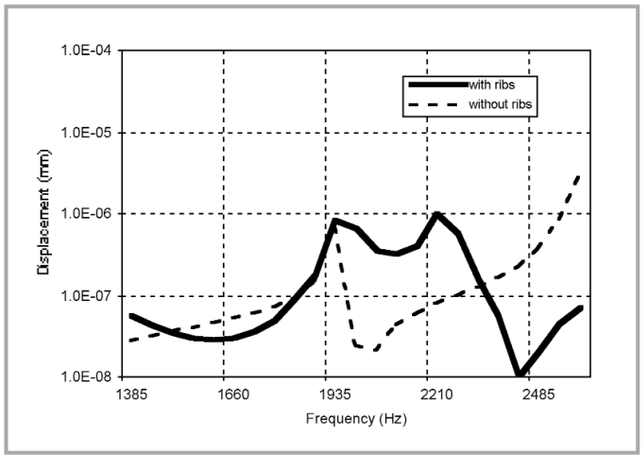

Figure 8: Effect of back plate ribs for the particular pairing mode shapes

is only one peak left, indicating that this mode pair occurred at the same frequency of 1927 Hz. Another example is the mode pair at frequencies of 4341 Hz and 4367 Hz. After the ribs are removed, this mode pair occurred at frequency of 4334 Hz. Both of these mode pair are shown in Figure 9.

Of all the 42 mode shapes of the drum brake at the frequency range between 1 kHz and 12 kHz, 17 of them are mode pair with

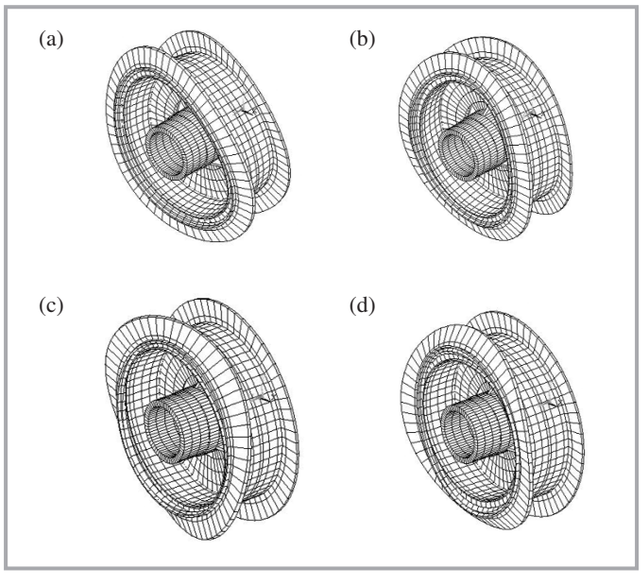

Figure 9: (a) Mode shape at 1955 Hz, (b) pairing mode of (a) at 2233 Hz, (c) mode shape at 4341 Hz, and (d) pairing mode of (c) at 4367 Hz

different frequencies. As the ribs are removed, all of these mode pair shapes occurred at the same frequency.

The effects of various components' stiffness can be observed in Figure 10. The drum modulus of elasticity and the back plate rib modulus of elasticity were changed to 207 GPa with density of 7820 kg/m3 for each case. The baseline for the comparison is the frequency response function of the drum brake having modulus elasticity of 69 GPa (indicated by continuous line).

Stiffening the drum (indicated by a dash-dot lines) resulted in some decrease in the natural frequencies of the drum brake while stiffening the drum back plate ribs has resulted in a more significant increase in the natural frequencies of the drum brake.

Effect of Flanges

The flanges are the part where spokes are mounted to connect

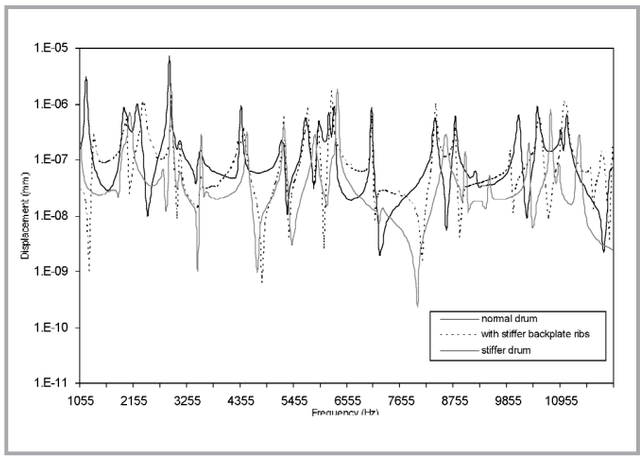

Figure 10: The effects of drum and ribs stiffness to the drum brake frequency response function

the drum to the rim. Modal analysis conducted after removing the flanges decreased the modal density of the drum brake to 33 mode shapes. It indicates that the flanges contributed 25 mode shapes to the overall drum brake mode shapes. The effects of other parameters of the flanges were analysed by altering the thickness of the flanges and changing the modulus elasticity of the flanges.

The effects of various parameters related to flanges to the drum brake frequency response function can be observed in Figure 11. The initial drum brake has E of 69 GPa and flange thickness of 4 mm. Increasing the thickness of the flange has resulted in the reduction of the natural frequencies of the drum brake. Increasing the stiffness of the flange has significantly reduced the natural

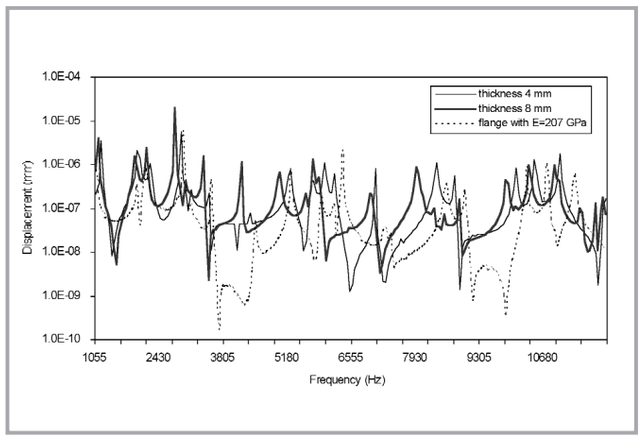

Figure 11: Effects of parameters related to flanges to the drum brake frequency response function

frequencies of the drum brake. The effect of various parameters for drum diametral mode shape frequencies is given in Table 3.

Effect of Shoe Back Plate Modulus of Elasticity

The flanges are the part where spokes are The influence of shoe back plate stiffness is analysed by changing the modulus elasticity of the shoe back plate from 69 GPa and density of 2720 kg/m^3 to 210 GPa and density of 7800 kg/m^3. Figure 12 gives the frequency response function in radial direction of the drum brake in reference to the lining node as the effect of this change.

DISCUSSION

Comparison of results from Figure 5 and Figure 7 when

006-012·analysis/ iem referees 9/20/05 12:00 PM Page 10

Table 3: Effect of various parameters for drum diametral mode shape frequencies

	Initial Drum E=69 GPa, 4 mm flange	Drum with E=207 GPa 4mm fla	Drum with rib E=207 GPa	Drum with 8mm flange	Drum with 4mm flange
First diametral mode frequency	1170Hz	1039Hz	1309Hz	1102Hz	899Hz
Second diametral mode frequency	1955Hz and 2233Hz	1952Hz and 2119Hz	1974Hz and 2346Hz	1899Hz and 2146Hz	1734Hz and 1906Hz
Third diametral mode frequency	5213Hz	5243Hz	5228Hz	4993Hz	4488Hz

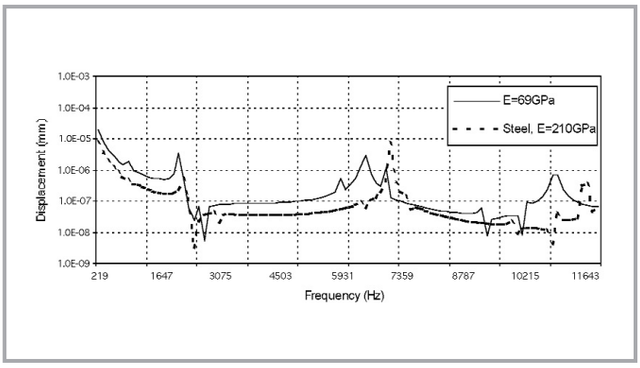

Figure 12: Frequency response function of the brake shoe for different stiffness and material properties, with damping ratio 0.04%, translation in radial direction

compared indicated high modal density of the drum brake and brake shoe with one mode at frequencies of 1500-2000 Hz and 3 modes at frequencies of 5600–6400 Hz, respectively. This mode proximity is potentially vulnerable to squeal since squeal in general occurs when two separate and distinct modes coalesce to form a mode pair, one of which is stable and the other unstable. The unstable mode manifests itself as squeal mode [10]. Since modal proximity is one of the criteria that can be used to prevent drum brake squeal at the design stage, parameters affecting the modes can be used to achieve this. In particular are the size and shape of the drum brake ribs whereby in the current design, the ribs consisted of radial stiffeners at 90 degrees angular space. The ribs cause mode separation of 278 Hz for the second radial mode which is essential for stability purposes and should be maintained. Removing the ribs causes the second radial mode pair to exist at a common frequency of 1955 Hz and this is to be avoided.

Changing the modulus of elasticity of the material does not have major influence on the number of mode shapes, which remains 42. The frequencies of the mode shifted to higher values, commensurate with the overall increase in stiffness.

The drum back plate is a dynamically important part in squeal generation where earlier works have shown that modifications carried out on drum back plate on automotive brake can stabilise the system [7,8]. With stiffer back plate ribs the overall displacement level goes down by one order of magnitude for mode shape which are related to the back plate deformation. Thus the back plate stiffening is beneficial for squeal reduction.

The effect of flanges thickness is to increase the mass of the drum but with no appreciable increase in stiffness of the back plate. This resulted in the overall decrease of the natural frequencies of the drum, particularly good frequency separation was obtained for modes in the frequency range of 5180 – 7930 Hz. If squeal occurs within this range, the modification of the flanges is one of the suitable remedies.

The shoe back plate that is currently made of cast aluminum alloy can be modified by the use of alternative materials of higher modulus of elasticity. The use of steel (E=207 GPa) will shift the natural frequency of the back plate. The overall results indicated that for the current motorcycle drum brake analysed, modal density is relatively high in the region of 1500 – 2000 Hz and 5600 – 6400 Hz. In the first range, the drum, stiffness can be increased to reduce the modal density as well as proximity. Adjusting the flange thickness to 8 mm reduces the modal density for the drum at the frequency range of 5600 – 6400 Hz, which will be one of the steps for reducing drum brake squeal propensity within the above range.

CONCLUSIONS

The analysis can be concluded as follows:

1. There are 42 mode shapes for the drum and 10 mode shapes for the shoe within the frequency range of 100 Hz and 12000 Hz.
2. Modal density is high in the frequency region of 1500 – 200 Hz and 5600 – 6400 Hz.
3. Increasing the stiffness of the drum is useful to reduce modal density for the lower frequency range (1500-2400 Hz) while increasing the flange stiffness reduces modal density in the higher frequency range (5600-6400 Hz).
4. The results have shown the important design parameters effect on the natural frequencies of the drum brake components. ■

REFERENCES

[1] P. V. Lamarque, "Brake Squeak: The Experience of Manufacturers and Operators: Report No. 8500B", *Inst. Auto Engrs. Research and Standardization Committee*, 1935.

[2] D.A. Crolla, and A.M. Lang, "Brake Noise and Vibration – The State of the Art", *Vehicle Tribology*, Leeds-Lyon 17, Tribology Series 18, (Dowson, D.;Taylor, C.M. and Godet, M., ed.) pp. 165-174, September, 1992.

[3] G.D. Liles, "Analysis of Disc Brake Squel Using Finite Element Method", *SAE Technical Paper Series* , paper 891150, 1989.

[4] H. Murakami, N. Tsunada, and M. Kitamura, "A Study Concerned with Mechanism of Disc Brake Squeal", *SAE Technical Paper Series*, paper 841233 , 1984

[5] Z.B.M. Ripin, D.C. Barton, and D.A. Crolla, "Analysis of Disc Brake Squeal Using the Finite Element Method" , *Proc. I. Mech. E., Conf. 'AUTOTECH 1995'*, paper C498/12/074, 1995.

[6] T. Hamabe, I. Yamazaki, K.Yamada, H. Matsui, and S. Nakagawa, "Study of a Method for Reducing Drum Brake Squeal", *SAE Technical Paper Series*, paper 1999-01-0144, 1999.

[7] J.D. Fieldhouse, "Low Frequency Drum Brake Noise Investigation Using a _ Vehicle Test Rig", *SAE Technical Paper Series*, paper 2000-01-0448, 2000.

[8] A. Felske, G. Hoppe, and H Matthai, "A Study on Drum Brake Noise by Holographic Vibration Analysis", *SAE Technical Paper Series*, paper 80-02-21, 1980.

[9] ANSYS Users Manual, Revision 6.0A (Vol I-IV), Swanson Analysis Inc, Houston, USA, 1992.

[10] H. Ghesquire, and L. Castel, "Brake Squeal Noise Analysis and Prediction", *Proc. I. Mech. E., Conf. 'AUTOTECH 1992*' paper C389/257,1992

006-012·analysis/ iem referees 9/20/05 12:00 PM Page 11

THE INSTITUTION OF ENGINEERS, MALAYSIA

Bangunan Ingenieur, Lots 60/62, Jalan 52/4, Peti Surat 223 (Jalan Sultan), 46720 Petaling Jaya, Selangor Darul Ehsan
Tel : 03-79684001/2 Fax : 03-79577678 E-mail : sec@iem.org.my IEM Homepage: http://www.iem.org.my

Dear IEM Members/Readers,

REFEREES FOR VETTING OF IEM PUBLICATIONS

The Standing Committee on Publications is revising the list of referees to assist in the vetting of articles received from members and non-members. The referees should preferably be at least Corporate Members of The Institution or graduates with higher degrees.

The aim of appointing the referee is to ensure and maintain a standard in the IEM Publications namely the bulletin and the Journal.

Members who are interested to be placed in the database of referees are to return the registration form to the IEM Secretariat, providing details of their degrees and particular expertise and experience in the engineering fields.

We need your services to look into the vetting of articles received for Publications and due acknowledgement would be announced yearly in the Bulletin. Referees must be committed to return the papers within a month from date of appointment.

Chairman
Standing Committee on Publications

All correspondences are to be addressed to: -

The Chief Editor
Standing Committee on Publications
The Institution of Engineers, Malaysia
Bangunan Ingenieur, Lots 60 & 62, Jalan 52/4
P.O. Box 223 (Jalan Sultan)
46720 Petaling Jaya
Selangor Darul Ehsan, Malaysia.

AREAS OF INTEREST FOR VETTING OF PAPERS

Please tick (√) the appropriate area of interest that you are able to vet the papers.

- ❑ Acoustics
- ❑ Aerodynamics
- ❑ Air Conditioning
- ❑ Air Pollution Control
- ❑ Aircraft
- ❑ Airport Engineering
- ❑ Aluminium Design
- ❑ Arbitration
- ❑ Automation
- ❑ Automotive Engineering
- ❑ Biochemical Engineering
- ❑ Biotechnology
- ❑ Boiler Engineering
- ❑ Bridge Engineering
- ❑ Building Services
- ❑ Coastal Engineering
- ❑ Co-Generation
- ❑ Computer Engineering
- ❑ Concrete Design
- ❑ Concrete Technology
- ❑ Construction Management
- ❑ Control Engineering
- ❑ Drainage Engineering
- ❑ Dynamics Design
- ❑ Earthworks
- ❑ Edible Oil Refining
- ❑ Electrical Transmission
- ❑ Electrochemical
- ❑ Electrotechnology
- ❑ Energy Technology
- ❑ Engineering Education
- ❑ Environmental Engineering
- ❑ Fine Chemical
- ❑ Finite Element
- ❑ Fire Detection
- ❑ Fire Engineering
- ❑ Floods
- ❑ Food Processing
- ❑ Foundation Engineering
- ❑ Fuzzy Logic
- ❑ Gas Engineering
- ❑ Geotechnical
- ❑ Heat Exchanger
- ❑ Highway
- ❑ Hydraulics
- ❑ H.V. Electrical Distribution
- ❑ Industrial Engineering
- ❑ Industrial Transport
- ❑ Industrial Ventilation
- ❑ Information Technology
- ❑ Instrumentation
- ❑ Lighting System
- ❑ L.V. Electrical Distribution
- ❑ Manufacturing
- ❑ Mass Transit
- ❑ Mechanical Handling Equipment
- ❑ Management
- ❑ Metal Fabrication
- ❑ Metallurgy
- ❑ Micro Electronics
- ❑ Military Vehicles
- ❑ Mini Pressure Meters
- ❑ Mining Engineering
- ❑ Naval Architecture
- ❑ Navigation
- ❑ Oil & Gas Engineering
- ❑ Operation Research
- ❑ Palm Oil Industries
- ❑ Petrochemicals
- ❑ Petroleum Engineering
- ❑ Pharmaceuticals
- ❑ Piling
- ❑ Plumbing Engineering
- ❑ Pollution Control
- ❑ Ports & Harbour Engineering
- ❑ Power Electronics
- ❑ Power Generation
- ❑ Pressure Vessels
- ❑ Prestressed Concrete
- ❑ Project Management
- ❑ Public Administration
- ❑ Public Health Engineering
- ❑ Quarry Engineering
- ❑ Railways
- ❑ Reclamation Works
- ❑ Refrigeration
- ❑ Reinforced Concrete Beams
- ❑ Road Transport
- ❑ Robotics
- ❑ Roof Structures
- ❑ Room Temperature
- ❑ Safety Engineering
- ❑ Scaffolding Works
- ❑ Seepage
- ❑ Sewerage
- ❑ Shipbuilding
- ❑ Signal Processing
- ❑ Solar Energy Technology
- ❑ Steelworks Design
- ❑ Stream Turbine Power Plant
- ❑ Sructural Analysis
- ❑ Structural Rehabilitation
- ❑ Survey Engineering
- ❑ Taligates
- ❑ Telecommunication
- ❑ Thermal Engineering
- ❑ Timber Design
- ❑ Tool Engineering
- ❑ Transfer Tunnels
- ❑ Transportation Engineering
- ❑ Urban Planning
- ❑ Vehicles
- ❑ Vertical Transportation
- ❑ Waste Treatment
- ❑ Waste Water
- ❑ Water Resources Engineering
- ❑ Water Pollution Control
- ❑ Wind Engineering
- ❑ Others (please specify)

DISCIPLINES / SUB-DISCIPLINES OF VETTER

Please tick (√) the appropriate boxes.

- ❑ Aerospace
- ❑ Aeronautical
- ❑ Agricultural
- ❑ Chemical
- ❑ Civil
- ❑ Electrical
- ❑ Electronics
- ❑ Environmental
- ❑ Industrial
- ❑ Marine
- ❑ Mechanical
- ❑ Mining
- ❑ Naval Architecture
- ❑ Petroleum
- ❑ Production
- ❑ Structural
- ❑ Others (Please specify)

VETTER'S DETAILS

Name : _____

Membership No. : _____ (if applicable)

Grade : ❑ Graduate ❑ Member ❑ Fellow ❑ Affiliate

❑ Others (please specify) _____

_____

Qualifications : _____

Addresses : (Office) _____

_____

_____

(Residence) _____

Contact No. : Handphone: _____ Office: _____ Residence: _____

E-mail Address : _____

Please mail all correspondences to the below. Please tick (✓) the appropriate boxes.

Mail to : ❑ Office ❑ Residence

Brief Biodata (not longer than 50 words) (to be appended with this Reply Slip).

_____

_____

Have you ever reviewed submissions for publication in any Journal(s) before?

❑ Yes ❑ No

If YES, name the Journal(s)

Do you have papers published in any Journal(s)?

❑ Yes ❑ No

If YES, name the Journal(s)

Date: _____ Signature: _____

ELASTO-PLASTIC DEFORMATION OF HOSTUN SAND DURING CYCLIC LOADING IN TRIAXIAL TEST

Eqramul Hoque

Department of Civil Engineering, Bangladesh University of Engineering and Technology, Dhaka – 1000, Bangladesh, INDIA

ABSTRACT

Cyclic triaxial tests were performed on dry air-pluviated solid cylindrical (7 cm diameter and 15 cm high) specimens of Hostun sand (French sand). Both axial and radial strains were measured locally by using, respectively, a pair of Local Deformation Transducers (LDTs) and three pairs of gap sensors. An isotropically consolidated specimen (at 78.4 kPa) was subjected to cyclic prestraining (CP) with a large number of relatively large amplitude axial-stress cycles. Elastic Young's modulus E^e defined for an axial strain increment less than 0.002% was evaluated at various stress-states along the CP stress path. The effects of CP were investigated on elastic and plastic deformation characteristics along the CP stress path. Elastic parameters were changed slightly due to CP although the overall elastic deformations along the CP stress path were more stable than the plastic deformation characteristics. The plastic deformation component was drastically affected by CP. As a result, the stress-dilatancy relation was changed in a complicated manner.

Keywords: *Triaxial, Local-strains, Cyclic, Elasticity, Plasticity, Prestraining*

INTRODUCTION

A soil mass upon which a structure is founded often experiences cyclic loading caused by fluctuations in loading intensity. For instance, in the case of wave loading on offshore structures, traffic loading on pavements and heavy machine vibrations on foundations the number of cyclic loading is very large although the magnitude of the non-constant component of loading is relatively small. The effects of a series of small seismic loading may also be included in this category. Cyclic loading should, therefore, be rationally accounted for whenever it is likely to improve safety and/or efficiency in design purpose. Often, engineering judgment is required to decide whether, and to what degree, the effects of cyclic loading phenomena ought to be accounted for.

Precise separation of elastic and plastic components of deformation is essential for proper elasto-plastic modeling of sand deformation subjected to a wide variety of strain history [1-2]. In this study, this was attempted by measuring elastic strain increment components frequently during shearing. The importance of the above was investigated by comparing the elasto-plastic deformation characteristics of a prestrained specimen with those of a virgin one. Effects of cyclic prestraining (CP) on the deformation of soil is very important also for structures subjected to heavy traffic, seismic activity, machine vibration, and other dynamic loading such as off-shore structures. A large number of loading cycles (of the order of single amplitude axial strain $(\varepsilon_a)_{SA}$=0.02~0.1%) on dry sand has been observed to increase the elastic limit strain and tangent stiffness both in cyclic and monotonic loadings and to decrease significantly damping at relatively large strain levels (say, $(\varepsilon_a)_{SA}\geq$0.01%), with relatively smaller effects on the elastic Young's modulus (E^e) [3]. Therefore, the deformation characteristics of a prestrained specimen differ noticeably from that of a virgin one not because of changes in elasticity but because of large changes in plasticity including dilatancy characteristics. Modeling of such a prestrained specimen should, therefore, require proper characterisation of those aspects. Described herein are the effects of CP on elastic and plastic deformation properties in the light of the results from a comprehensive series of triaxial tests.

THE TESTING SYSTEM

The triaxial apparatus used in this study is shown schematically in Figure 1. A solid, cylindrical specimen of 7.5 cm diameter and 15 cm high was tested. Unlike many other conventional triaxial systems, it includes facilities for a) measurements of axial load by using a sensitive and rigid load cell installed within the triaxial cell to eliminate the effects of piston friction, b) automated anisotropic consolidation by controlling axial and radial stresses independently, c) bedding-error-free 'on-sample' direct measurements of axial deformation by using local deformation transducers (LDTs) [4], and d) local measurements of radial deformations of dry specimen by using 3 pairs of proximity transducers mounted on a system of attachment.

One proximity transducer and one dial gage were also used to measure the displacements of the loading cap and the loading piston, respectively. The external strains obtained from the above may include large effects of bedding error. Radial strains were measured at three heights (2.5-, 7.5- and 12.5-cm above from the bottom) of each specimen assuming that radial strain distribution could be less uniform in the vertical direction compared with axial strain distribution. Two sets of proximeters, each set consisting of three, were mounted on a pair of two-direction micrometer tables so that they can be effectively moved along the vertical and horizontal directions at any stage of test if required; horizontal movement/shifting is often required when repeated loading test is performed, since such a test usually brings about large plastic deformations.

Tests were performed by using a stress-controlled loading system [5]. From the functional point of view, the system has two basic components: a static pressure unit and a cyclic pressure unit, both being fed into from a house pressure unit. The house pressure unit consists of (a) an air compressor, which supplies high air pressure; (b) a regulator, which, based on the maximum pressure, provides constant house pressure

013-018·elasto plasticity 9/20/05 12:06 PM Page 14

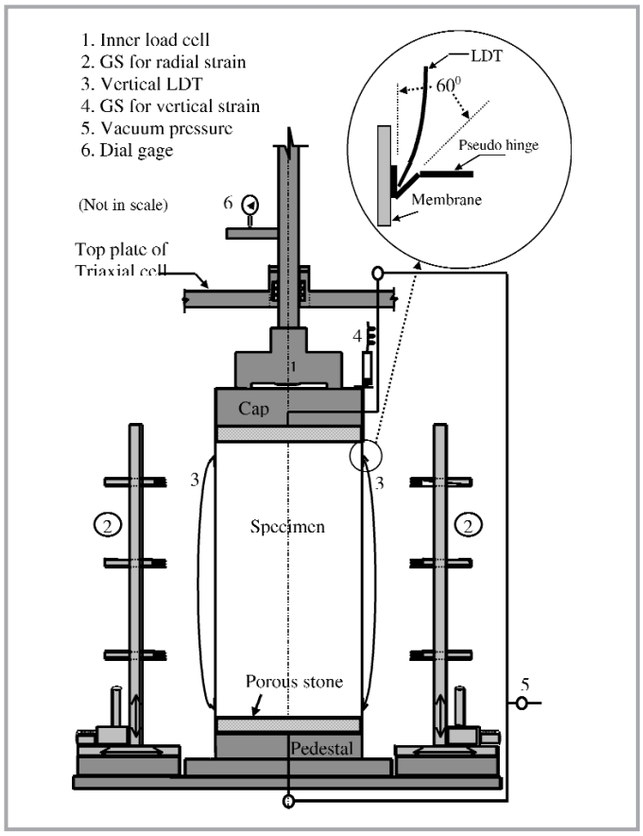

Figure. 1: Triaxial testing system

from the air-compressor; and (c) an accumulator and filter tank unit, which filters and then accumulates supplied air. The static pressure unit, fed by a high pressure line from the accumulator, supplies static pressure via a regulator to the lower chamber of a double-acting Bellofram cylinder. On the other hand, cyclic pressure is controlled by an electro-pneumatic (E-P) transducer through its two inlets. One inlet is connected to the high pressure line from the accumulator. The other receives driving signals for cyclic loading from a control unit. The control unit could be either a software-guided micro-computer or an auto-function generator. Both control units were used in the study. The E-P transducer receives continuous signals, depending on the amplitude and frequency of a cyclic loading (CL) test, from the function generator or computer; it converts the commanding signals into an equivalent pressure through maintaining a static equilibrium on the torque bar seated inside the E-P transducer. Finally, the equivalent pressure after having been amplified in volume by using another regulator (booster) is conveyed to the upper chamber of the Bellofram cylinder. A specimen is directly connected to the Bellofram cylinder through a loading piston. Any change in pressure, static or cyclic, in the Bellofram cylinder results in the corresponding change in the axial stress of the specimen. The confining stress was applied by partial vacuum. Using a 12-bit 16 channel analogue-to-digital converter card, the data acquired by using the transducers is fed into a 16-bit micro-computer.

TEST PROGRAM AND PROCEDURE

The tests were performed on specimens of Hostun sand (collected from France) at dry state. Hostun sand is a fine-grained, quartz-dominant and sub-angular (grain shape) sand. The physical properties of the sand are: D_{10}= 0.17 mm, D_{50}= 0.31 mm, U_C = 1.94, G_S = 2.65, e_{max} = 0.95 and e_{min} = 0.55. A cylindrical specimen (7.5 cm diameter and 15 cm high) was reconstituted by raining air-dried sand particles through air into a split mold. Regular ends (i.e., non-lubricated ends using porous stones) were used at both ends of the specimen. A partial vacuum of 10 kPa was applied to a specimen which was completely enclosed within a rubber membrane before the mold was dissembled. A freestanding specimen was then consolidated isotropically to a pressure σ_c (= 78.4 kPa for all specimens in this study), at which the specimen dimensions were measured before any instrumentation. Cyclic loading tests were then performed symmetrically about a neutral axial stress state.

Test program on a given specimen consisted of CL tests at various amplitudes, which was repeated at different instants of testing to investigate the effects of CP on E^e, elastic and plastic deformation characteristics along the CP stress path. Tests were performed on two specimens HOSTN3 and HOSTN5 with void ratio e, respectively, 0.72 and 0.81 being measured at σ_c = 78.4 kPa.

Elastic Young's modulus (E^e) was evaluated by applying very small cyclic axial load for which the single-amplitude axial strain, $(\varepsilon_a)_{SA}$, was kept within 0.002%. The Young's modulus of a specimen of clean sand evaluated at this strain level is observed to be independent of the type of loading (cyclic or monotonic), rate of shearing (static or dynamic), load-history and the degree of over-consolidation as long as the initial fabric remains essentially unchanged [6-8]. This feature has been validated particularly by the fact that a Young's modulus E^e value thus obtained is essentially similar to that obtained by measuring body wave velocities. So, this value can be considered to be the maximum Young's modulus which a soil element can exhibit in its current state.

Cyclic loading, including CP (i.e., the application of a large number of relatively large amplitude stress cycles along a fixed path), was applied symmetrically about either an isotropic or an anisotropic stress state. Note that in both cases, the radial stress σ_r was 78.4 kPa. The loading frequency (f) for CP was in the range of 0.1 to 0.5 Hz, while it was 0.1 Hz in the CL tests performed for evaluating soil parameters. The latter frequency (i.e., f = 0.1 Hz) was employed to assist a micro-computer to sample a sufficient number of data-per-cycle for analytical purposes. A prescribed number of cyclic loading was applied in CP with a fixed axial-stress amplitude (CP_{str}) during which the value of $(\varepsilon_a)_{SA}$ was changed drastically. Typical relationships between axial stress σ_a , axial strain ε_a and radial strain ε_r are shown in Figure 2. The relationships are plotted for the virgin cycle (i.e., cycle 1), the 2nd, 200th and 25,000th cycles. During CP with CP_{str} on a given specimen (Figure 2), the value of $(\varepsilon_a)_{SA}$ was not a constant value; rather it decreased with the number of loading cycles.

RESULTS AND DISCUSSIONS

Axial strains measured by gap sensor usually include system compliance error [2, 7] and so was the case in the present study. The axial strains ε_a measured by two vertical LDTs (Figure 1), on averaging, are shown in Figure 2 and the following figures if not otherwise specified. In this and the following figures, if not specified otherwise, the axial stress and/or the stiffness (i.e., E^e) are normalised by dividing it with

013-018·elasto plasticity 9/20/05 12:06 PM Page 15

pressure P_a (= 98 kPa). The ε_a and ε_r axes for the prestrained specimen (i.e., after CP) were shifted arbitrarily. The actual values of strains (ε_a and ε_r) at the bottom ends of the curves for the prestrained specimen (denoted as S_p) can be seen from Figure 3, in which the translation of strain axes with the number of loading cycles at the reference stress state $\sigma_a = \sigma_r =$ 78.4 kPa are shown in semi-logarithmic plot. In the figure, the volumetric strain ε_{vol}, defined as $\varepsilon_a + 2\varepsilon_r$, was also shown. It can be seen that translation was maximum in the first cycle; the translation was maximum in the direction of major principal strain (i.e., ε_a); the ε_a axis was translated almost linearly after the first cycle in the semi-logarithmic scale, while it was almost constant in ε_r axis; consequently, ε_{vol} axis was translated at a smaller rate. Even after the application of a large number of prestraining cycles, the translation of strain axis in the major principal direction did not cease completely.

Elastic Young's modulus E^e was evaluated at various stress states along the CP stress path both before and after CP. Before CP, it was measured during the 3rd cycle. Note that the elastic parameters (E^e and the elastic Poisson's ratio ν) were evaluated by applying very small amplitude cyclic loads in which the single amplitude axial strain was less than 0.002%. Figure 4 shows the relationships between $E^e/f(e)$ and the axial stress σ_a

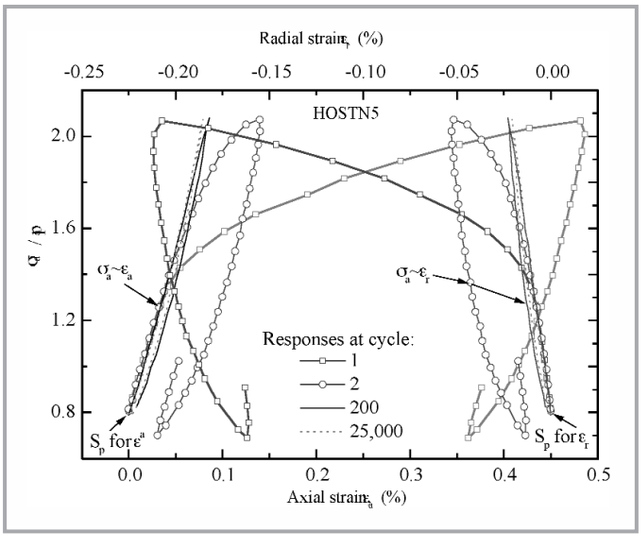

Figure 2: *σ_a~ε_a and σ_a~ε_r relationships of large CL tests at virgin state*

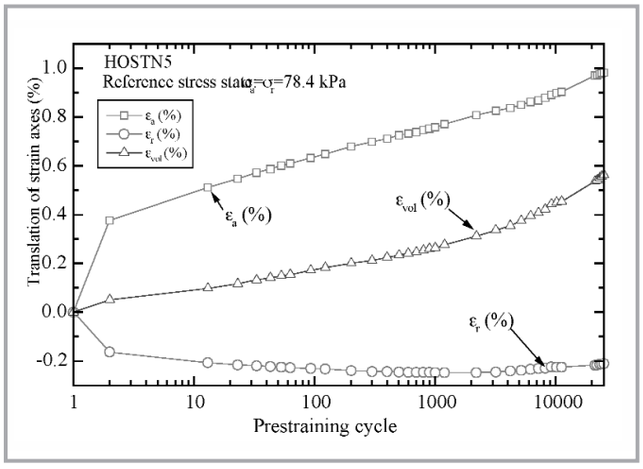

Figure 3: *Translation of sttrain axes with the number of loading cycle during CP*

in full logarithmic scale obtained from HOSTN5 specimen. The E^e value was normalised by dividing it with a void ratio function $f(e) = (2.17 - e)^2 / (1+e)$ [9] in order to account for the change in void ratio during the course of testing program. However, the change in void ratio was negligible, which needed less than 1% correction in the measured value of E^e. In the same figure, E^e values measured along the isotropic stress path at virgin state (i.e., before CP application) were also plotted for comparison. It can be seen that $E^e/f(e) \sim \sigma_a$ relationship obtained from isotropic stress path was similar to that obtained along the CP stress path at the virgin state (i.e., before CP). It indicates that E^e measured for axial strain increment increased with the increase in σ_a. That is, the elastic Young's modulus was a function of axial stress in the direction of major principal strain increment. Among many others, [6,10-11] showed a large number of data supporting the above behavior. Accordingly, the above stress-dependency of Young's modulus can be modeled as [10-11]:

$$E^e = E_1 \text{ x } f(e) \text{ x } (\sigma_a / P_a)^m \tag{1a}$$

On the other hand, the Poisson's ratio ν (i.e., horizontal-to-vertical strain ratio defined for small increment less than 0.002% in the major principal strain direction) measured along the CP stress path can be modeled as:

$$\nu = \nu_0 \text{ x } (\sigma_a / \sigma_r)^{m/2} \tag{1b}$$

In the above equation, various entities used are: $E_1 = E^e$ measured at $\sigma_a =$ 98 kPa when $f(e) = 1.0$ (i.e., for $e = 0.82$); $\nu_0 =$ the average value of Poisson's ratio ν measured at isotropic stress states; $P_a =$ atmospheric pressure and $m < 1.0$, a nonlinear exponent relating σ_a with E^e. The values of elastic parameters E_1 / P_a, ν_0 and m for HOSTN5 specimen evaluated at virgin states were, respectively, 1800, 0.20 and 0.47 and those for HOSTN3 specimen were, respectively, 1964, 0.17 and 0.46. It can also be seen from Figure 4a that the stress-dependency relationship between E^e and σ_a was slightly changed due to CP application. As a result, E^e values decreased at larger stress states while it increased at the lower stress states along the CP stress path. Consequently, both E_1/P_a and m values were noticeably changed (i.e., they became 1536, 0.81 for HOSTN5 and 1900, 0.80 for HOSTN3 specimen) from the respective initial values. However, CP did not bring about any changes on the elastic Poisson's ratio ν (and also ν_0) and its dependency on the stress ratio σ_a / σ_r as modeled by Eq.(1b). The detail of modeling E^e and ν were described in [7,12].

Elastic strains for the whole stress range of CP_{str} were obtained by integrating $d\varepsilon_a^e = d\sigma_a / E^e$ and $d\varepsilon_r^e = -\nu \text{ x } d\varepsilon_a^e = -\nu \text{ x } d\sigma_a / E^e$ by using the relations Eq.(1a) and Eq.(1b) together with the respective elastic parameters E_1, m and ν_0. Note that these values were affected by CP. The relationships between σ_a and the elastic axial and radial strains (ε_a^e, ε_r^e) were arbitrarily plotted in Figures 5a and b, respectively, with the origins denoted as S_a and S_p at the bottom end (i.e., at $\sigma_a =$ 78.4 kPa for HOSTN5) of the respective σ_a~ε_a and σ_a~ε_r relation for the range of CP_{str}. A drastic changes in the σ_a~ε_a (Figure 5a) and σ_a~ε_r (Figure 5b) relations were caused by a substantial reduction in the plastic strain components ($\varepsilon_a^p = \varepsilon_a - \varepsilon_a^e$, $\varepsilon_r^p = \varepsilon_r - \varepsilon_r^e$) due to CP, while the σ_a~ε_a^e relation changed

013-018·elasto plasticity 9/20/05 12:06 PM Page 16

very slightly due to the change in the elastic parameters. The effects of CP application by 25,000 and 65,000 cycles along the same stress path were very similar (Figures 5a and b). Now it can be understood why the stress-strain relations after CP concave upward with a small hysteresis area. It is interesting to note that the ε_r^e and σ_a relation happened to be linear. The behavior described above was due to the intrinsic elastic

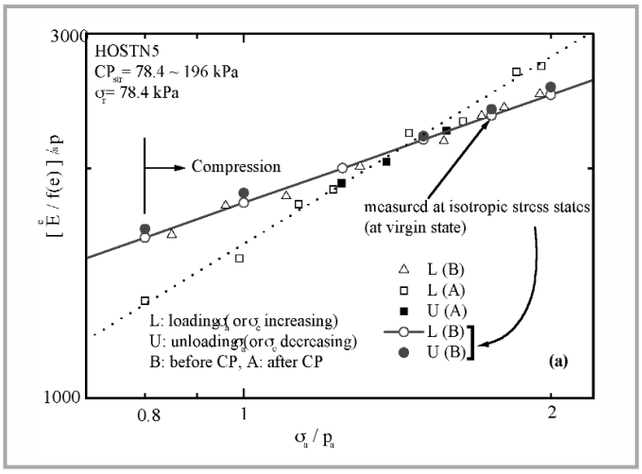

Figure 4a: Relationship between E^e *and* σ_a *of HOSTN5 specimen*

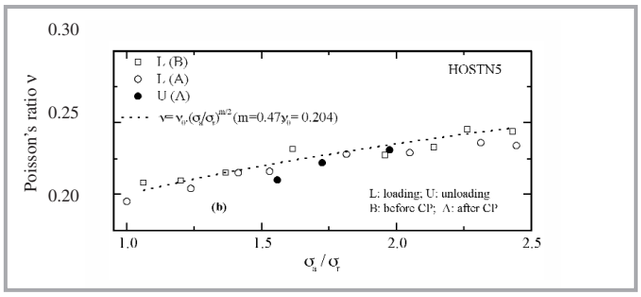

Figure 4b: Relationship between ν *and* σ_a/σ_r *along CP sstress path*

property of sand. That is, according to Eq. 1a, the elastic behavior of a sand is hypo-elastic type [10] and if one estimates the elastic strain component along a fixed stress path, the shape of the resulting elastic-strain and stress curve would be concave upward. Similar shape (i.e. concave upward) of the stress-strain curves (Figures 5a and b) was resulted from after CP application, indicating the dominance of elastic-strain component in total strain.

A considerable decrease in the plastic-to-elastic strain increment ratio occurred due to CP, which can be observed from Figures 6 and 7 for HOSTN3 and HOSTN5 specimen, respectively. The relationship between plastic-to-elastic strain increment ratio in axial direction (r_a) and σ_a , both before and after CP, are shown in Figures 6a and 7a, respectively, for HOSTN3 and HOSTN5 specimen. Similar relationship between plastic-to-elastic strain increment ratio in radial direction (r_r) and σ_a are shown in Figures 6b and 7b, respectively, for HOSTN3 and HOSTN5 specimen. It can be seen from Figures 6 and 7 that before CP, the elastic-to-plastic strain increment ratios (i.e., r_a and r_r) varied widely and nonlinearly with σ_a , whereas after CP, it varied narrowly and more-or-less linearly with σ_a during

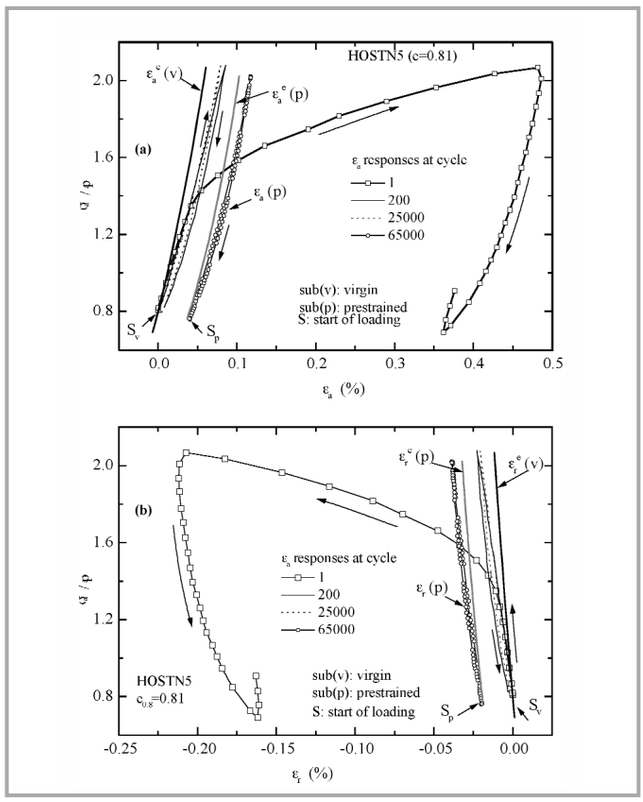

Figure 5: (a) σ_a~ε_a *and (b)* σ_a~ε_r *relationships of virgin and prestrained states in CP stress path*

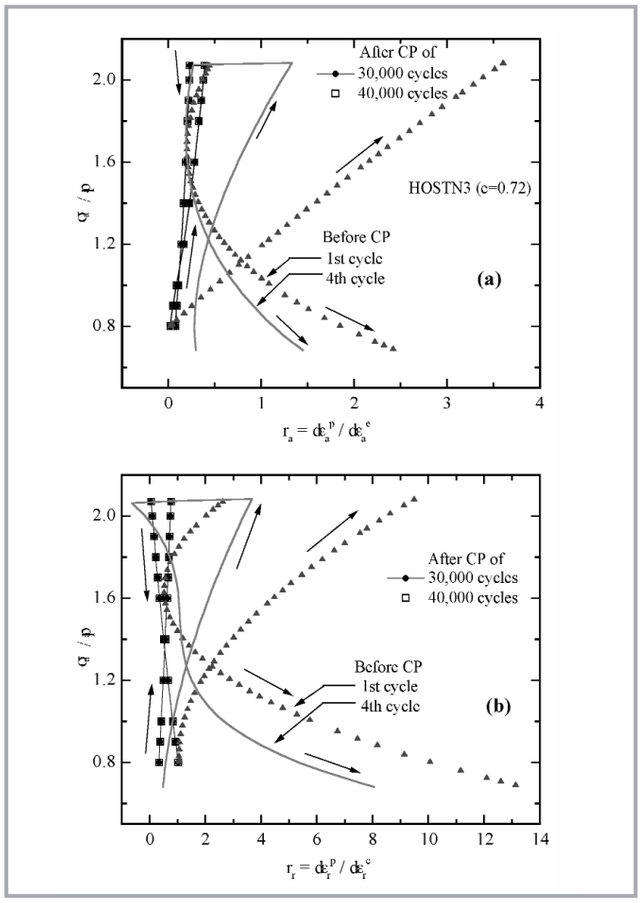

Figure 6: (a) σ_a~ε_a *and (b)* σ_a~ε_r *relationships of virgin and prestrained states in CP stress path*

013-018·elasto plasticity 9/20/05 12:06 PM Page 17

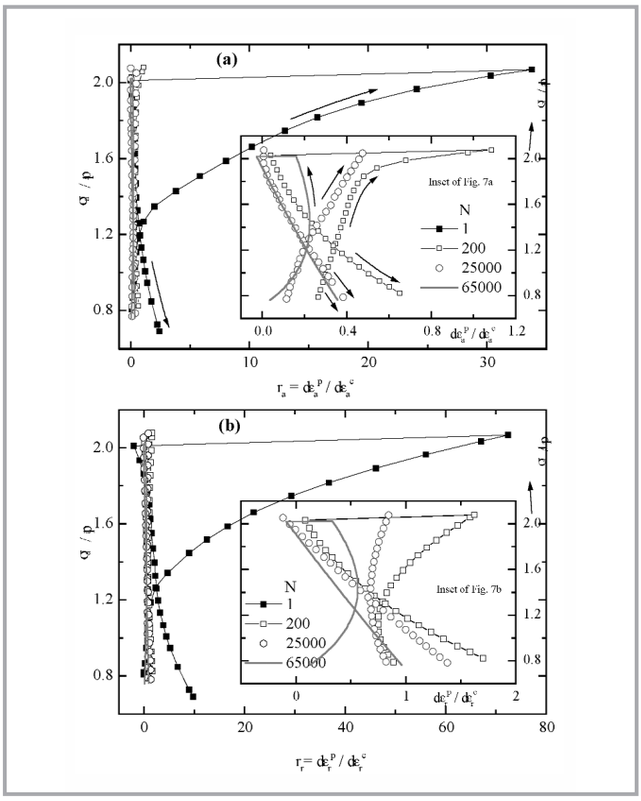

Figure 7: (a) σ_a~ε_a and (b) σ_a~ε_r relationships of virgin and prestrained states in CP stress path

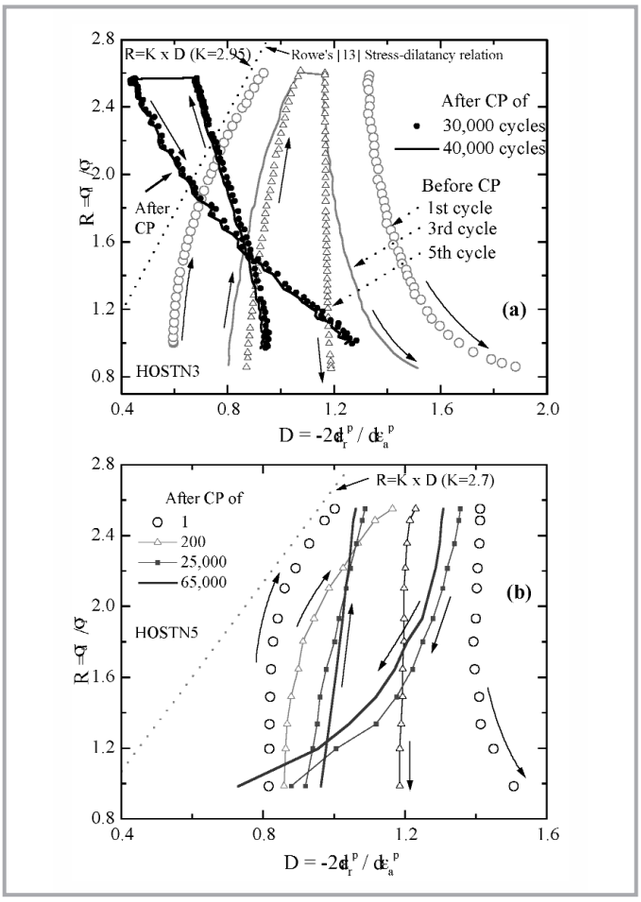

Figure 8: (a) σ_a~ε_a and (b) σ_a~ε_r relationships of virgin and prestrained states in CP stress path

both loading and unloading. For a given specimen (i.e., void ratio) before CP, the r_a values varied in much wider ranges than that occurred in r_r values. On the other hand, at a given stress level, for loose specimen (HOSTN5) the values of r_a and r_r were significantly larger than those of the dense specimen (HOSTN3). However, for both specimens after CP, both r_a and r_r values became narrowly varying within the CP stress path.

It is important to note that the higher values of r_a and r_r before CP application indicate that the deformations at this stage were dominated by the plastic strain components. As the number of prestraining cycle increased, the values of r_a and r_r decreased drastically, indicating the decrease of plastic strain component compared to the elastic strain component. Besides, significant difference was observed between the values of r_a and r_r if one compares the data of the 1st cycle and the 4th cycle (Figures 6a and b). However, after the application of a large number of prestraining cycles in the same stress path, the r_a and r_r values were in the range between 0.5 to 2.0 (Figures 6 and 7). Therefore, the deformation, in no cases, for the whole range of σ_a (CP_{str}) which was applied as CP did not become totally elastic even after the application of a very large number of CP stress cycles. On the other hand, cyclic prestraining by 30,000 and 40,000 cycles did not show any difference for medium dense specimen HOSTN3 (Figures 6a and b), whereas some differences could be observed between the responses after 25,000 and 65,000 cycles in the loose specimen HOSTN5 (Figures 7a and b).

Figures 8a and b show the relationships, respectively, of HOSTN3 and HOSTN5 between the stress ratio ($R = \sigma_a / \sigma_r$) and the dilatancy rate (defined as $D = -2d\varepsilon_r^p / d\varepsilon_a^p$). The relation (i.e., $R \sim D$) during loading at the virgin states followed closely the Rowe's [13] stress-dilatancy relation $R = K \times D$ with K=2.95 for HOSTN3 and K= 2.7 for HOSTN5. But the linear stress-dilatancy relationship (i.e., $R = K \times D$) did not observe in case of unloading, reloading and re-unloading. Before CP, the relations approached to the non-plastic volumetric strain increment condition (i.e., $D = 1.0$) for both loading ($d\sigma_a > 0$) and unloading ($d\sigma_a < 0$). The relations after CP showed a different trend; during loading more contractive behavior (i.e. $D > 1.0$) with the increase in $R = \sigma_a / \sigma_r$, whereas during unloading more dilative behavior (i.e $D < 1.0$) could be observed. This behavior was much more complicated than the behavior predicted by Pradhan and Tatsuoka [14].

Figures 9a and b show the relationships between R and plastic prestrain-to-virgin shear strain increment ratio (*PPVS*) for specimens HOSTN3 and HOSTN5, respectively. *PPVS* decreased significantly for both loading ($\Delta\sigma_a > 0$) and unloading ($\Delta\sigma_a < 0$) with a large discontinuity along *PPVS* axis at the point of stress reversal. With the increase in loading cycle (i.e. CP), the value of *PPVS* for a given σ_a gradually decreased in such a way that the $\sigma_a \sim PPVS$ relation for a particular cycle (during loading or unloading) remained parallel to the similar relation at virgin state.

CONCLUSIONS

Elastic Young's modulus E^e of Hostun sand was axial stress dependent. That is, E^e measured in the axial stress direction by applying very small amplitude cyclic loading was a function of

013-018·elasto plasticity 9/20/05 12:06 PM Page 18

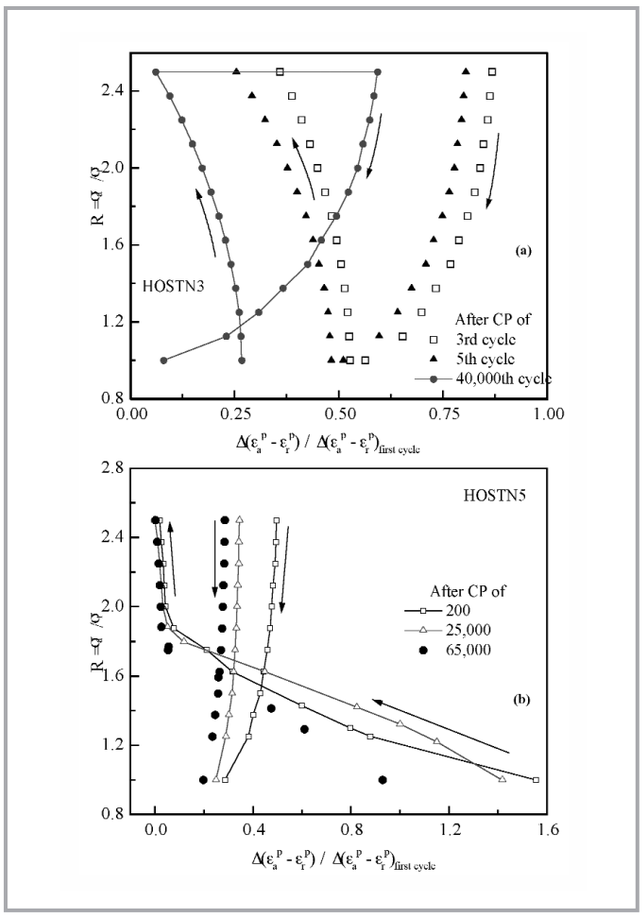

Figure 9: *(a)* σ_a~ε_a *and (b)* σ_a~ε_r *relationships of virgin and prestrained states in CP stress path*

the axial stress (σ_a) only and it increased nonlinearly with the increase in σ_a . Deformation characteristics of the sand during a relatively large amplitude stress cycle were dominated by plastic strain component at virgin state. With the increase of the application of prestraining cycles along the fixed stress path, the plastic strain increment decreased drastically. Therefore, the elastic strain component became equally significant as the plastic strain component. Deformation did not become totally elastic even after the application of a large amount of CP with a relatively large amplitude of axial stress cycle. The elastic deformation characteristics were much more stable compared to plastic deformations, but they also changed slightly due to CP. Therefore, the deformation of sand cannot be modeled precisely by a simple elasto-plastic model having a fixed range of elasto-plastic parameters. The stress-dilatancy relation was changed by cyclic loading in a complicated manner. ■

REFERENCES

[1] J.B. Burland, "Small is beautiful-the stiffness of soils at small strains", *Ninth Laurits Bjerrum Memorial Lecture, Canadian Geotechnical Journal*, Vol. 26, pp. 499-516, 1989.

[2] F. Tatsuoka, S. Teachavorasinskun, J. Dong, Y. Kohata and T. Sato, "Importance of measuring local strains in cyclic triaxial tests on granular materials", *Dynamic Geotech. Testing, ASTM STM 1213*, ASTM, pp. 288-302, 1994.

[3] S. Teachavorasinskun, *Deformation Characteristics of Sands at Small Strains*, Doctoral thesis, The University of Tokyo, 1992.

[4] S. Goto, F. Tatsuoka, S. Shibuya, Y-S. Kim and Y. Sato, "A Simple Gauge for Local Small Strain Measurements in the Laboratory", *Soils and Foundations*, Vol. 31, No. 1, pp. 169-180, 1991.

[5] E. Hoque and F. Tatsuoka, "Triaxial testing-system measuring loading-rate effects during cyclic tests of sand", *Geotechnical Testing Journal*, ASTM, Vol. 27, No. 5, pp. 483-495, Sept. 2004.

[6] M. Jamiolkowski, S. Lerouell and D.C.F. Lo Presti, "Design parameters from theory to practice", *Theme Lecture, Geo-Coast '91*, Yokohama, pp. 877-917, 1991.

[7] E. Hoque, F. Tatsuoka and T. Sato, "Measuring anisotropic elastic properties of sand using a large triaxial specimen", *Geotech. Testing J., ASTM*, Vol. 19, No. 4, pp. 411-420, 1996.

[8] F. Tatsuoka, R.J. Jardine, D. Lo Presti, H. Di Benedetto and T. Kodaka, "Characterizing the pre-failure deformation properties of geomaterials", *Theme Lecture for the Plenary Session No. 1, 14th Int. Conf. On SMFE, Hamburg*, Vol. 2, 1997.

[9] B.O. Hardin and F.E.Jr. Richart, "Elastic wave velocities in granular soils", *Journal of SMFE, ASCE*, Vol. 89, No. SM1, pp. 33-65, 1963.

[10] E. Hoque and F. Tatsuoka, "Anisotropy in elastic deformation of granular materials", *Soils and Foundations*, Tokyo, Vol. 38, No. 1, pp. 163-179, 1998.

[11] K.H.II. Stokoe, J.N.K. Lee and S.H. Lee, "Characterization of soil in calibration chambers with seismic waves", *Proc. Of Int. Symp.on Calibration Chamber Testing*, Clarkson Univ., Potsdam, NewYork, Huang Edition, Elsevier, pp. 363-376, 1991.

[12] G.L. Jiang, F. Tatsuoka, A. Flora and J. Koseki, "Inherent and stress state-induced anisotropy in very small strain stiffness of a sandy gravel", *Geotechnique*, 47-3, pp. 509-521, 1997.

[13] P.W. Rowe, "The Stress-Dilatancy Relation for State Equilibrium of an Assembly of Particles in Contact", *Proc. Royal Society, 269A*, pp. 500-527, 1962.

[14] T.B.S. Pradhan and F. Tatsuoka, "On Stress-Dilatancy Equations on Sand Subjected to Cyclic Loading", *Soils and Foundations*, Vol. 29, No. 1, pp. 65-81, 1989.

A GENERALISED PRICE-SCORING MODEL FOR TENDER EVALUATION

Thum Peng Chew
BE (Hons), M Eng Sc, FIEM, P. Eng, MIEEE

ABSTRACT

This paper proposes a generalised price-scoring model derived from behavioural features of prospect theory for use in a tender evaluation program. It has the potential to overcome the limitations of existing price models by allowing the within-price attribute score variations to be adjusted by a preference factor. It improves selectivity and incorporates a preference function that emphasises the evaluator and decision maker's preference in the lowest price by allowing a price-scoring curve to be derived from the skewness of the distribution of tender prices and the tender participation rate. It identifies prices that exceed the project budget and penalises them. Statistical data from a survey of tender prices was used to specify the model for practical use. Comparison between generic classes of models using price difference and price ratio functions as price gain measures is made to illustrate the model's general applicability. With the choices made available in this generalised price-scoring model, it is possible to compare the various methods of tender evaluation by computer simulation.

Keywords : *Tender Prices, Price Comparison, Price Scoring Model, Tender Price Evaluation, Judgment, Decision Making*

INTRODUCTION

The objective of tender price scoring is to assign the right values to tender prices within a project budget and to score them so that a fair evaluation that reflects the judgment and preference of the evaluator and decision maker, can be made. The rule of tender evaluation is to award a higher score to a lower price tender because a lower price has a higher value to the evaluator and decision maker. In manual evaluation methods, the price values are assigned by human judgment on an ordinal scale which implies a qualitative price-value relationship. If software decision-support tools are used in integrated tender evaluation of price and non-price attributes, price must be evaluated by a quantitative value function that converts price in monetary unit to a score on an objective numerical scale. How prices are evaluated affects the final tender ranking.

A survey of literature indicated that research on price-value relationship for the purpose of tender evaluation is scarce. One simple quantitative value function that has been used by Karsak [1] for the evaluation of flexible manufacturing systems is a price inverse model for scoring a cost-related attribute. The score synonymous with value, is derived from the price inverse, $\chi_i = x_i^{-1}$ where x_i is the price of the ith tender. The model's weakness is its tendency towards indifference and not having the means to assign a degree of preference for low prices. Thus, there is no flexibility for it to fully express the judgment of the evaluator and decision maker through a preference function.

A wider search in the subject of judgment and decision making [7,8,9,10] revealed the existence of value functions in prospect theory proposed by Tversky and Kahneman [2,3] since 1979. The theory replaces the notion of utility with value which is defined in terms of gains and losses from a reference point. They suggested that the value function defined over monetary gains is $\chi_i = x_i^p$ for x_i above a reference price(0) and over losses is $-\lambda(-x_i)^p$ for x_i below the reference price. Determined from experimental data, p is 0.88 and λ is 2.25, indicating diminishing marginal value and asymmetry between gains and losses. The application of the proposed value function has received attention recently [4,7,8,9] in a number of situations in which the norms and characteristics of decision makers are modelled.

Variations in a tender's overall value are contributed by the within-attribute variations and the between-attribute variations. A value function deals only with the within-price attribute variations while the weighting functions of the tender evaluation procedures in [5,6] provide the between-attribute variations. This paper presents a generalised price-scoring model that determines the within-price attribute variations from the prices of competing tenders. Because all judgments and decisions are context-dependent [8], the credibility of a generalised price-scoring model rests on its ability to capture an evaluator or decision maker's tendency for dominance or non-dominance and on its ability to express mathematically the decision maker's judgment that is translated into a continuous continuum of strong to weak emphasis of tender price. In a realistic model, the behavioural features in prospect theory have to combine with the cost objective to achieve a wide scope of application for situations in which the decision maker's behaviour varies. Prospect theory is helpful up to this point after which the preference factor is dependent on behaviour that has to be approximated by information in a tender.

To achieve this objective, it borrows from prospect theory some behavioural features that are not found in multi-attribute utility theory and applies it to tender price judgment:

- Evaluators and decision makers are more sensitive to cost overrun than cost saving in the sense that they will reject tenders that have prices exceeding the project budget.

- If there are sufficient tender proposals to select from without cost overrun, they will view the tender's lowest price as indicative of the fair market value and the average price plus margin as the budget's upper bound.

019-026·price scoring 9/20/05 12:12 PM Page 20

- If the tender prices are significantly less than the project budget, they become strongly gain-seeking so as to accrue larger cost savings and to compensate for the original over-estimate.
- If the tender prices are close to but below the project budget, their gain-seeking tendency is weaker because with lesser cost saving, attention is shifted to the non-price attributes of the tender to accrue higher non-price gains.

This paper is organised as follows. First, a generalised price-scoring function of a similar form as the value function of prospect theory is proposed. Next, the project budget acting as the reference price is defined and its implications discussed. A preference function is developed for strong to weak gain-seeking, the strength of which is determined by the tender price coefficient of skewness and tender participation rate. A survey of tender prices elicits the two statistics which together with the evaluator's preference limits, are used to determine the constants of two generic classes of models. Within each generic class, comparison between price difference and price ratio functions as gain measures is made to illustrate the model's general applicability. Finally, appropriate applications of the two generic classes are suggested.

PRICE VALUE FUNCTIONS

In general, the mathematical function of a price-scoring model that captures the essence of how a score, A relates to a price gain variable, X must have the following properties.

(i) A monotonically increases with X

(ii) $0 \le \mathbf{A} \le 1$ for $0 \le X \le 1$

(iii) $\dfrac{dA}{dX} \ge 0$ for $0 \le X \le 1$

From prospect theory [2,3], the value/score, A_i derived from the price gain X_i, of the ith tender price out of m tender prices is suggested below for two generic classes of models.

Un-normalised class: $A_i = X_i^{\,p}$ (1a)

Normalised class: $A_i = \dfrac{X_i^{\,p}}{\sum_{i=1}^{m} X_i^{\,p}}$ (1b)

where generally $-\infty < p < \infty$. Equation 1b also ensures that $\sum_{i=1}^{m} A_i = 1$ as a result of normalisation. When p is negative, a price closer to the maximum price will result in a higher score because the negative root of a small price gain produces a score close to unity. Because this is contrary to the tender evaluation rule of low price-high score, the price-scoring model must not consider values of p that are negative. With this exclusion, the preceding properties are still satisfied but additional properties are required to define the variable, p for various behavioural states as follows.

(i) $A(X)$ is constant for $p = 0$

(ii) $A(X)$ is proportional to X for $p = 1$

(iii) $A(X \ne 1) = 0$ for $p = \infty$

(iv) For Equation 1a, $0 \le p \le 1$

The evaluator or decision maker's behaviour can be approximated by the preference factor, p which defines the gain-seeking tendency in the shape of the price-scoring curve. With Equations 1a and 1b, there is no effect caused by price gain on the scores when $p = 0$ i.e. they all have the same unity score for the un-normalised class and $\frac{1}{m}$ for the normalised class. When p increases from 0, the model starts to exhibit a lower price-higher score characteristic, initially still having the tendency to be price indifferent. When $p = 1$, it scores linearly with price gain and is not adjusted by preference (judgment). With Equation 1b, when $p = \infty$, the lowest price attains the maximum score of 1 unit while the rest of the prices are scored zero irrespective of their gain value. Thus, as p moves from 0 to ∞, the price-scoring characteristic moves from one that is insensitive to price gain, hence eliminating price competition, to one that exhibits the strongest preference for the lowest price, hence creating the stiffest competition that results in only one possible contender. In other words, the price-scoring model inherently allows for a range of effects to be accommodated, namely indifference, linear and non-linear dependence on price gain through the specification of p.

THE PROJECT BUDGET AS A REFERENCE PRICE

Before tenders are called, a value of the project cost $\hat{x}$ is estimated. Based on this value, a project budget is given taking into account an assigned contingency cost which is provided to mitigate situations of cost overrun caused by residual project risk. If the contingency cost allocated is c, the project budget, x_B is $\hat{x} + c$. When tender submissions are received, their prices are compared with either the project cost estimate or the budget allocation. Evaluators prefer not to risk cost overrun and will be reluctant to recommend award of a contract whose price exceeds the project cost estimate or the budget. As a means of control, a price-scoring model must assign the lowest price score, usually zero, to prices exceeding the budget i.e. the value function for losses is set to zero for exclusion purpose and is restricted to coding of price gains. The budget is a reference price on an objective scale and has the same meaning as that of prospect theory discussed in [2,3,4,7].

If cost overrun is limited by x_B, then the price gain has a range $x_B - x_{min}$. If the tender prices are ordered in ascending value in the sequence, $x_{(1)}, x_{(2)}, .., x_{(j)},.., x_{(m-1)}, x_{(m)}$, then $x_{min} = x_{(1)}$. Any price, $x_{(q)}$ that exceeds x_B should either be assigned an evaluation-adjusted value equal to x_B or should be automatically excluded from the evaluation. If $x_{(1)}$ exceeds x_B, it will be the only price allowed to participate in the evaluation with gain equal to zero. This requirement ensures that in the event that all tender prices exceed the budget value, the lowest price tender will be the only alternative worthy of any consideration as far as tender price evaluation is concerned. By accurate estimation, an under-budget situation can be avoided most of the time.

PRICE-SCORING CURVES

The exponent, p in Equations 1a and 1b determines the shape of the price-scoring curve. Strong gain-seeking means a

019-026·price scoring 9/20/05 12:12 PM Page 21

high preference ($p > 1$) for low price. In zero (neutral) preference cases ($p = 1$), it would exhibit a straight line obtained by joining the lowest price score with the score at x_B over the price difference range, $x_B - x_{min}$. Weak gain-seeking means a tendency to de-emphasise price preference ($0 < p < 1$). At the limit when $p = 0$, all prices are treated equally and the scores are impartial to price difference.

To illustrate the price-scoring curve, the highest score, A_{max} from Equation 1b is given by

$$A_{max} = A_{(1)} = \frac{X_{(1)}^{p}}{\sum_{i=1}^{m} X_i^p} = \frac{(1-\|P_{(1)}\|)^p}{\sum_{i=1}^{m}(1-\|P_i\|)^p} \qquad (2)$$

where the normalised price is for simplicity, expressed as $P_i = 1 - X_i$.

If the highest score $A_{(1)}$, is set to unity, $A_{(1)}$ is expressed as follows:

$$A_{(i)} = \frac{A_{(i)}}{A_{max}} = \left(\frac{1-\|P_{(i)}\|}{1-\|P_{(1)}\|}\right)^p \qquad (3)$$

A continuous plot of $A_{(i)}$ against P_i is shown in Figure 1 for various value of $p > 0$ to illustrate the shape of the price-scoring curves. Using the curves, the evaluator and decision maker can selected the degree of preference to match their judgment.

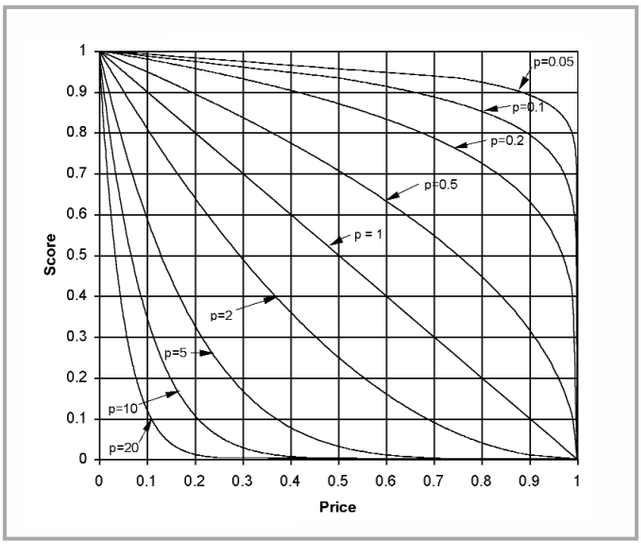

Figure 1: Normalised score against normalised relative price

DISTRIBUTION OF PRICES

Information about the tender can be extracted from the price distribution statistics. In an ideally competitive environment, the coefficient of variation and the variance are indicative of the degree of dissimilarity of the pricing characteristics of the tenderers. Price skew is an asymmetry arising out of either legitimate reasons or collusion [11,12]. It is not the purpose here to determine its cause but to use it to determine preference. The existence of a low price located to a distant left of a central bunch of prices (Figure 2a) gives rise to left asymmetry and a negative coefficient of skewness. If the prices are ideally symmetrical about their mean (Figure 2b), then the coefficient of skewness is zero. The existence of a high price located to the distant right of a central bunch of prices (Figure 2c) gives rise to a right asymmetry and a positive coefficient of skewness.

The coefficient of skewness, υ is proposed as a measure of the degree of gain-seeking. It qualifies by having the following properties.

(i) Its magnitude monotonically increases with skew
(ii) For a positive (right) asymmetry, it is positive and it must represent a strong gain-seeking characteristic that favours the lowest price from the bunch of prices by making the scores reduce very quickly to zero for exceptional prices that are located much higher than the lowest price.
(iii) For symmetry of prices, it is zero and it must not contribute to any preference by being neutral.
(iv) For a negative (left) asymmetry, it is negative and it must represent a weak gain-seeking characteristic that still favours the lowest price but the scores of the bunch of prices are not reduced too quickly.

The lowest price is distant from the central bunch of prices because the pricing of the lowest tender is either made under a different condition or with a different strategy from those of the central bunch. The lowest tenderer may have a legitimate advantage over the rest because of technology, available capacity, resources and location which can be evaluated outside the price domain as in [4,5]. Or in an attempt to win the contract, the lowest price tenderer may resort to higher risk-

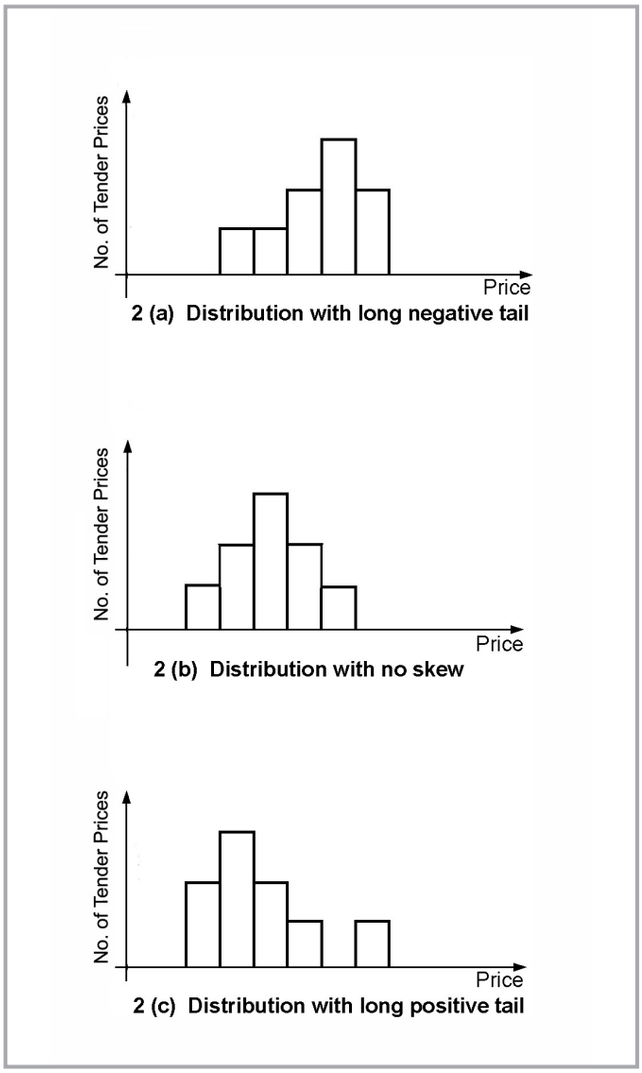

Figure 2: Illustration of skewness in frequency distribution

019-026·price scoring 9/20/05 12:12 PM Page 22

taking and cutting profit margin, a strategy that the others may not be willing to adopt. If the determination of the project budget is accurately done, such extreme price deviation from the cost estimate must signal the need for extra caution during the evaluation and to uncover the hidden project risks. While giving the highest score, the evaluator is risk-averse and must prudently limit the emphasis of the lowest price. A similar effect may also be created from strategies that defeat fair competition by many forms of cartel collusion. Non-competing cartel prices are increased and the cartel-promoted tenderer's price is raised to just below the next-lowest price [12,13] as illustrated in the comparison between Figures 2a and 2b. If such strategies are revealed in the skew, they are penalised through exclusion by the budget limit as well as by price de-emphasis. When automatic action could not be taken effectively by the software program, pre-assignment of p (<1) is the way to counter this problem.

If behaviour is expressed in the preference factor p, the distribution's coefficient of skewness υ, is a behaviour variable that induces a preference such that the relation between p and υ meets the following:

(i) $p > 0$ for $-\infty < \upsilon < \infty$
(ii) $p = \infty$ if $\upsilon \to \infty$
(iii) $p = 1$ if $\upsilon \to 0$
(iv) $p = 0$ if $\upsilon \to -\infty$

A possible general polynomial expression that satisfies these properties is the skewness factor, k_1 given as follows:

$$k_1 = \sum_{i=1}^{L1} \alpha_{2i-1} \upsilon^{2i-1} \quad (4)$$

where α_{2i-1}'s are positive constants to be determined for L_1 terms. υ is zero if the number of tenders evaluated is less than 3.

TENDER PARTICIPATION RATE

If there are sufficient tender proposals to select from without incurring cost overrun, the price-scoring model should allow for increase in its price selectivity under a situation of high tender participation rate. When υ is very negative, p is near zero. The scores tend to equalise and lose their discriminative ability. In Equation 1b, high tender participation rate decreases the absolute scores by the effect of a larger denominator. The consequence is that when the price scores are brought into the aggregation process with other non-price factors, they become less contributory from their low score values and the lack of discrimination. This effect is counteracted by increasing the value of p with tender participation rate. One way is to include in p, a separate tender participation factor, k_2 which is a function of the number of tenderers, m being evaluated. It should have p increasing monotonically with m i.e. $\frac{dp}{dm} > 0$ for $m > 0$.

It is suggested that k_2 adopts a general positive polynomial function of m in the form

$$k_2 = \beta_0 + \sum_{j=1}^{L2} \beta_j m^j \quad (5)$$

where β_0 is a constant and β_j's are positive constants to be determined for L_2 terms. When $m = 1$, there is no competition and k_2 can be set to zero thus, $\beta_0 = -\sum_{j=1}^{L2} \beta_j$.

GENERAL PREFERENCE FUNCTION

How k_1 and k_2 should be combined to obtain p does not have a unique approach. It must be application dependent and satisfy practical and intuitive requirements. One approach is to add the effects of distribution skew, k_1 and the effects of tender participation rate, k_2 i.e. $k_1 + k_2$. An additive effect has advantage over the multiplicative one ($k_1 \bullet k_2$) because it would not nullify the effect of tender participation rate if the skewness were zero. However, addition alone cannot satisfy all the properties of p. A non-nullifying and property-complying expression for p as a function of k_1 and k_2 is suggested as follows:

$$p = \exp(k_1 + k_2) \quad (6)$$

This expression restricts the value of p to > 0 and thus, satisfies the required properties of p. k_1 contributes to p by ensuring the possibility of specifying a strong preference for low price with positive skew or a de-emphasis of preference for low price with negative skew. It ensures that when $\upsilon = 0$, zero (neutral) preference results from it. The tender participation rate, m contributes positively to p through k_2. Exponentiation ensures a positive p all the time and it amplifies the combined effects, thus making the influence of p stronger. Flexibility is given such that without the aid of these two factors, the evaluator and decision maker can still assign the value of p independently.

At this point, it is seen that the price-scoring model combines the ideas of price gain measure, X and of the degree of preference p, which is a function of the skewness of the price distribution and the number of tenders evaluated, to calculate the price scores, either un-normalised or normalised respectively.

ANALYSIS OF TENDER PRICES

If the purpose of tender evaluation is to select an optimum tender, then the information that reveal price relativities should be put into good use for decision making. A survey was conducted to gather data on tender participation rate and tender prices with the aim of obtaining statistics on tender participation rate and on tender coefficients of variation and skewness. The range of values of m and υ can then be established for use in the price-scoring model. From a total of 75 data sets from past tender exercises, the coefficients of variation (deviation/mean) and skewness for each data set were calculated. From their distributions, the coefficients' means, medians and deviations were obtained from statistical analysis and are summarised in Table 1. The coefficient of skewness is expected to vary from negative values to positive values while the coefficient of variation is always positive.

95% of the tenders has a participation rate below 10 and the median is 4. The price coefficient of variation's mean and median are close to each other at 0.1274 and 0.1221 respectively while its deviation is small at 0.0752. The survey data are indeed from tenderers who shared similar localised

019-026·price scoring 9/20/05 12:12 PM Page 23

Table 1: Analysis of tender participation rate and tender prices

Tender Price Coefficients' Statistics	Tender Participation Rate, m	Price Coefficient of Variation, σ/μ	Price Coefficient of Skewness, υ
Mean	4.933	0.1274	0.2828
Median	4	0.1221	0.4682
Deviation	2.124	0.0752	0.9764
5th Percentile	3	0.02637	-1.5570
95th Percentile	9.3	0.2850	1.6301

characteristics [13] and quoted prices with small deviations from the mean price. 95% of the coefficients of variation is below 0.2850. A budget up to 1.285 times the project cost estimate will capture most tender prices for evaluation. The mean of the coefficient of skewness, μ_υ is 0.2828 and its deviation, σ_υ is larger at 0.9764. 90% of its variations lies within the range of –1.5570 and 1.6301 with a median of 0.4682. The large σ_υ is an indication of the sensitivity of skewness to extreme values and υ can be suitably employed to vary the preference over a wide range.

SPECIFIC PREFERENCE FUNCTION

A specific preference function for the price-scoring model adopts the first order functions of $k_1 = \alpha\upsilon$ from Equation 4 and of $k_2 = \beta(m\text{-}1)$ from Equation 5, where α and β are the positive constants in the expression of p as follows:

Thus, $p = \exp[\alpha\upsilon + \beta(m\text{-}1)]$ (7a)

or $q = ln\ \mathrm{p} = \alpha\upsilon + \beta(m\text{-}1)$ (7b)

The price-scoring model is to work within the specified limits determined by:

- The maximum tender participation rate, m_{max} and the minimum, which is 1.
- The upper and lower percentiles of the coefficient of skewness (υ_{max} and υ_{min}) of the tender distribution.
- The upper and lower limits (p_{max} and p_{min}) of the preference factor

The tender participation rate can be estimated from the number of tender documents collected and thus a maximum can be set. A minimum of 1 is set to ensure that the effect of tender participation rate could be felt at 2 onwards according to Equation 7a.

Equation 7b shows that the variation of the model constants, α and β are dependent on the logarithm of the preference limits. They are less sensitive to the variations of p and can accommodate the fuzziness of subjective judgments without large changes in value. Figure 1 provides the evaluator and decision maker a means of specifying the limits by inspection.

Thus, $q_{max} = ln\ p_{max} = \alpha\upsilon_{max} + \beta(m_{max} - 1)$ (8a)

$q_{min} = ln\ p_{min} = \alpha\upsilon_{min}$ (8b)

Solving for α and β,

$$\alpha = \frac{q_{min}}{\upsilon_{min}} \tag{9}$$

$$\beta = \frac{q_{max}\upsilon_{min} - q_{min}\upsilon_{max}}{\upsilon_{min}(m_{max} - 1)} \tag{10a}$$

If $\beta' = \beta(m_{max}\text{-}1)$,

then, $$\beta' = \frac{q_{max}\upsilon_{min} - q_{min}\upsilon_{max}}{\upsilon_{min}} \tag{10b}$$

To ensure that α is positive (> 0), then v_{min} and q_{min} must have the same sign.

For $\beta \geq 0$, $(q_{max}\,\upsilon_{min} - q_{min}\,\upsilon_{max})/\,\upsilon_{min} \geq 0$ (11a)

$$\frac{\ln p_{max}}{\ln p_{min}} \geq \frac{\upsilon_{max}}{\upsilon_{min}} = \kappa \tag{11b}$$

$$p_{max} \geq p_{min}\,\kappa \tag{11c}$$

$$p_{min} \geq p_{min}\,\kappa \tag{11d}$$

The choice of p is guided by the intuitive requirement that the effect of υ should be greater than that of m.

Thus, $\alpha > \beta'$ and $p_{max} < p_{min}^{\lambda}$ (12)

where $\lambda = \frac{1+\upsilon_{max}}{\upsilon_{min}} = \kappa + \upsilon_{min}^{-1}$.

For a given p_{min}, combining Equations 11c and 12 gives the range of p_{max}.

$$p_{min} < p_{max}^{\kappa} < p_{min}^{\lambda} \tag{13a}$$

Similarly given p_{max}, $p_{max}^{\frac{1}{\lambda}} > p_{min} > p_{max}^{\frac{1}{\kappa}}$ (13b)

From the price survey, $\hat{\upsilon}_{min}$, $\hat{\upsilon}_{max}$ can be obtained for specified percentile limits of its distribution. κ can be calculated. $\hat{p}_{min}$ is specified to calculate α. p_{max} is then selected so that β and β' are kept positive. In this paper, the range of the skewness coefficient is fixed at –1.5567 and at 1.6301 to give κ equals to –1.0472. To cater for at least 95% of tender cases, m_{max} is fixed at 11. The corresponding values of α and β' are shown in Table 2 for each pair of p_{min} and p_{max}. The effect of tender participation can be nullified ($\beta = 0$) by either p_{min} or p_{max} determined from Equations 11c and 11d. For a given p_{min}, the evaluator and decision maker can choose the strength of tender participation rate from the range of values of p_{max} determined from Equation 13a. Nullification will not occur if p_{max} is larger than the lower extreme value. With 3 parameters fixed, the preference function p, is determined from p_{min} and p_{max} for $\lambda = -1.6896$ as follows. Given $p_{min} = 0.2$, $5.395 < p_{max} < 15.167$ and given $p_{max} = 5.0$, $0.3857 > p_{min} > 0.2151$.

019-026·price scoring 9/20/05 12:12 PM Page 24

Table 2: Values of α and β' for the preference function ($\hat{\upsilon}_{max}$ = 1.6301 and $\hat{\upsilon}_{min}$ = –1.5567)

p_{min}	p_{max}	α	β' (m_{max} = 11)
0.3	5.0	0.7733	0.3489
0.25	5.0	0.8904	0.1581
0.2151	5.0	0.9871	0.0000
0.2	7.5	1.0337	0.3300
0.2	5.395	1.0337	0.0000

PRICE GAIN FUNCTIONS

Only price gains are of interest. At this point, the model excludes the coding of losses which is done in prospect theory. In an integrated tender evaluation procedure, price gain must be dimensionless. When price is in monetary unit, it must be evaluated separately because it is not compatible with other dimensionless attributes. One property of a price gain function is that for prices, $x_i > x_j > x_k$, the price gains derived from these prices must satisfy the condition $X_i < X_j < X_k$. Transitivity of price gains must be assured.

The qualitative ordinal scale commonly used cannot be adopted here because it fails to preserve the numerical information of price. Value scores must be made on quantitative scales. From experience, both price difference and price ratio have been use in tender evaluation. Price difference is a comparison of prices in an interval scale whereas price ratio represents relative value comparison in a ratio scale.

PRICE DIFFERENCE MODEL SUB-CLASS

For the price difference model, the price gain variable is a measure of the distance of a price from an upper price limit and is expressed as follows.

$$X_i = \frac{x_{max} - x_i}{x_{max} - x_{min}} \tag{14}$$

where x_{max} is the reference price on the interval scale and x_{min} is the lower price limit in the tender and x_i is the tender price of the ith tender alternative. The price gain, $0 \le X_i \le 1$ is a normalised measure of price difference. It is small if x_i is close to the reference price, x_{max} and it is largest (unity) when $x_i = x_{min}$. With the project budget x_B, the price gain in dimensionless unit is adjusted to

$$X_i = \frac{x_B - x_{(i)}}{x_B - x_{min}} \tag{15a}$$

such that $x_{min} = x_{(1)}$ and if $x_{min} > x_B$, all X_i's = 0.

An un-normalised price gain in monetary unit is given by

$$X_i = x_B - x_{(i)} \tag{15b}$$

This is a straightforward relation that equates price score with price difference. It is a useful measure for evaluation methods that compare marginal benefit with price and evaluate price separately from the other criteria. Although it does not satisfy the condition $0 \le X \le 1$, it can be included in the generalised model as a special case in which the price gain value is equated with the price difference.

Correspondingly from Equation 15a and 15b, the ordered price gain sequence, $X_{(1)}, X_{(2)},.., X_{(j)},.., X_{(m-1)}, X_{(m)}$ in descending price difference, is obtained for calculating their scores, $A_{(i)}$. Thus, this method is a comparison based on ordered absolute values with reference to an artificial zero at x_B. It also satisfies the transitivity property.

PRICE RATIO MODEL SUB-CLASS

If X is allowed to assume other non-linear functions of price, it is possible to incorporate $X_i = \chi_i = x_i^{-1}$, Karsak's value function, into the generalised price-scoring model. Although p equals to unity, its scoring curve is strictly not linear. If $x_i = x_{min} + \Delta x_i$, where Δx_i is a small positive difference of the ith price above the minimum price, x_{min}, then the value function is given by

$$X_i = \frac{1}{x_{min} + \Delta x_i} \approx \frac{1}{x_{min}}\left(1 - \frac{\Delta x_i}{x_{min}}\right) \tag{16}$$

If normalisation is done, the value function represents a ratio as follows:

$$X_i = \frac{x_{min}}{x_{min} + \Delta x_i} \approx \left(1 - \frac{\Delta x_i}{x_{min}}\right) \tag{17}$$

Both Equations 16 and 17, when substituted into Equation 1b produce identical effects. Both differ from the price difference function. The generalised model accepts both these two price ratio functions but Equation 16 can only be used in the normalised class of models because on its own it is not dimensionless. Cost control is implemented by excluding prices that exceed x_B from evaluation. The largest price does not necessarily have a low value because Equations 16 and 17 work in an ordered ratio scale with natural zero. Thus, a restriction to good discrimination is imposed. From the price survey, the standard deviation of price is small, making Δx_i of Equations 16 and 17 small relative to x_{min}. X_i is thus closer to unity than to zero. These two price gain functions satisfy the transitivity property but not the referencing property required in prospect theory. They represent a specific sub-class that works on ratio comparison.

COMPARISON BETWEEN PRICE DIFFERENCE AND PRICE RATIO MODELS

Discrimination and cost control are the bases of comparison between the two model sub-classes. One set of tender prices for low-price bunching and one set for high-price bunching are used to illustrate the characteristics of the price ratio and price difference models. The two tender sets have the same minimum and maximum prices. Their statistics are tabulated in Tables 3 and 4 for both tenders. The higher price tender naturally has the higher mean price. When the large extreme prices are eliminated by cost control, the mean prices are reduced slightly but they remain relatively robust enough to continue to indicate the market norm. The behaviours of their standard deviations and coefficient of skewness are less predictable because they are dependent on the price distribution after cost control action. A more reliable indication of the direction of change is seen in the reductions in the coefficients of variation after cost control. The tender with low-price bunching has coefficient of skewness of 1.721 for 8 prices and decreases to 1.324 for 7 prices after cost control. The corresponding values of *p* are 5.169 and 3.573 respectively. For the set with high-price bunching the coefficient of skewness is –1.170 for 8 prices and increases to –1.274 for 7 prices after cost control. The skew has

019-026·price scoring 9/20/05 12:12 PM Page 25

Table 3: Statistics from low-price bunching tender

Tender Prices, RM Million (Low-Price Bunching)	Statistics	Values (Cost-Controlled Values in Brackets)
5.973	Mean	6.079 (5.952)
5.713		
5.899	Standard Deviation	0.4119 (0.2201)
6.012		
6.386	Coefficient of Variation	0.0678 (0.0370)
5.926		
5.758	Coefficient of Skewness	1.721 (1.324)
6.965		

Table 4: Statistics from high-price bunching tender

Tender Prices, RM Million (Low-Price Bunching)	Statistics	Values (Cost-Controlled Values in Brackets)
6.673	Mean	6.515 (6.451)
5.713		
6.689	Standard Deviation	0.3998 (0.3846)
6.512		
6.788	Coefficient of Variation	0.0614 (0.0596)
6.226		
6.465	Coefficient of Skewness	-1.170 (-1.274)
6.965		

increased for high price bunching because the extreme (lowest) price is not eliminated by cost control in this case. The corresponding values of p are 0.3942 and 0.3538 respectively.

For a set of tender prices, 3 sets of normalised scores and 2 sets of un-normalised scores are calculated using a common preference function, p whose coefficients α and β determined earlier were adopted. The price scores from these 5 models are shown in Table 5 for low-price bunching and in Table 6 for high-price bunching. All 5 models show some degree of score bunching corresponding to price bunching. In Karsak's model, p equals to 1(α and β equal to zero) without cost control. Its scores are smaller compared with those of the price ratio model in the next column. Tables 5 and 6 show that the price ratio models do not convey significant score differences if the price differences are small when compared to their absolute values. As illustrated in Table 6, they more effectively provide information in terms of relative differences but are particularly weak in discriminating prices when there is high-price bunching. Comparatively, the price difference models are more discriminating because they enhance the scores of the low prices and reduce the scores of the high prices. As a result, they will tend to strengthen the effect of price when an overall tender evaluation is made together with the other non-price attributes.

By cost control, the over-priced scores of both the price ratio and the price difference models are set to zero, effectively eliminating over-priced tenders from consideration. To a small extent, cost control increases the normalised scores because the sum of scores is reduced by the elimination of the over-priced tender. The weakness of the price ratio model in not being able to score the budget price to zero is obvious here.

Normalisation makes the sum of scores equals to 1 and the individual scores less than 1. An un-normalised model enhances all price scores by making the score of the lowest price equal to 1. The larger score magnitude in the un-normalised price-scoring model has a greater ability to create price dominance in the evaluation because it always starts with a score of 1 irrespective of the number of tender prices.

PRICE-SCORING MODELS

From the generalised price-scoring model, a number of possible models for particular applications are derived as shown in Figure 3.

The un-normalised class using the un-normalised price-difference function with $p = 1$ is perhaps the simplest model and has attracted the widest application, especially in the 2-envelope system of tender evaluation in which price is separated from the non-price attributes. This model suits direct price comparison methods. Price difference in the mind of the evaluator is a straight forward and logical means of comparing prices in common monetary units. One would expect that a procedure by price difference is attractive because evaluators naturally judge and rank on the basis of price difference. By assigning $p = 0.88$, it becomes the original value function of prospect theory.

Table 5: Comparison among the price ratio models and the price difference models in low-price bunching case

Tender Prices, RM Million	Karsak's Model (α=0, β=0)	Normalised Price Scores Price Ratio Model (x_B = RM6.88million) (α=0.8904, β=0.01581)	Price Difference Model (x_B = RM6.88million) (α=0.8904, β=0.01581)
5.973	0.1267	0.1398 (*0.8530*)	0.1100 (*0.4063*)
5.713	0.1325	0.1639 (*1.0000*)	0.2708 (*1.0000*)
5.899	0.1283	0.1462 (*0.8918*)	0.1456 (*0.5378*)
6.012	0.1259	0.1366 (*0.8334*)	0.0940 (*0.3473*)
6.386	0.1185	0.1101 (*0.6717*)	0.0126 (*0.0464*)
5.926	0.1278	0.1438 (*0.8774*)	0.1318 (*0.4867*)
5.758	0.1315	0.1594 (*0.9724*)	0.2353 (*0.8689*)
6.965	0.1087	0.0000 (*0.0000*)	0.0000 (*0.0000*)

Note: Price scores in bracketed italic are un-normalised scores using Equation 1a.

Table 6: Comparison among the price ratio models and the price difference models in high-price bunching case

Tender Prices, RM Million	Karsak's Model (α=0, β=0)	Normalised Price Scores Price Ratio Model (x_B =RM6.88million) (α=0.8904, β=0.01581)	Price Difference Model (x_B =RM6.88million) (α=0.8904, β=0.01581)
6.673	0.1216	0.1410 (*0.9465*)	0.1247 (*0.5423*)
5.713	0.1421	0.1490 (*1.0000*)	0.2300 (*1.0000*)
6.689	0.1213	0.1409 (*0.9457*)	0.1212 (*0.5271*)
6.512	0.1246	0.1423 (*0.9547*)	0.1529 (*0.6648*)
6.788	0.1180	0.1395 (*0.9364*)	0.0242 (*0.1050*)
6.226	0.1303	0.1446 (*0.9700*)	0.1874 (*0.8147*)
6.465	0.1255	0.1426 (*0.9572*)	0.1595 (*0.6936*)
6.965	0.1165	0.0000 (*0.0000*)	0.0000 (*0.0000*)

Note: Price scores in bracketed italic are un-normalised scores using Equation 1a.

019-026·price scoring 9/20/05 12:12 PM Page 26

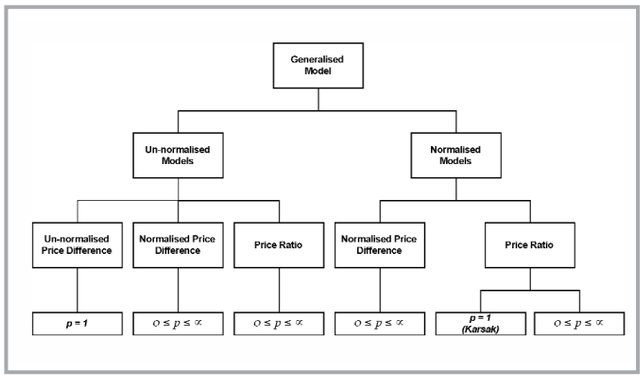

Figure 3: Particular price-scoring models from the generalised model

The un-normalised class using normalised price gain functions are suitable for integrated evaluation of both price and other non-price attributes in a computer program. Because of their larger score values compared with those of the normalised class, they have price dominant tendencies. The price-difference function can be adopted if dominance by a single price is desired. On the other hand, the price-ratio function will tend to move the scores away from single-price dominance. When price bunching occurs, collective dominance exists in the un-normalised function. The normalised class using normalised price gain functions have different characteristics compared with those of the un-normalised class of models. They produce an effect that tends not to emphasise on price nor discriminate between prices thus, allow the other attributes to play more influential roles in the evaluation. Their smaller scores are controlled by the number of tenders evaluated. The more tenders, the smaller the scores and the lesser the ability to dominate.

The choice of any of the above models should be made by matching their characteristics with the evaluation objective. If the lowest price is to dominate, then an un-normalised class of price-difference scoring model is appropriate. If price dominance is not intended, then a normalised class of price-ratio scoring model is more effective. Both the un-normalised and normalised classes that use a dimensionless price gain function based on either price difference or price ratio meets the requirement of dimensionless attribute scores in Thum's fuzzy tender evaluation model [5].

CONCLUSION

A generalised price-scoring model is developed by incorporating two price gain functions, one based on price difference on an interval scale and the other on price ratio on a ratio scale. It attempts to prevent cost overrun by eliminating over-priced tenders by comparison with the project budget. The behaviour of evaluators and decision makers is modelled in the preference factor which is a function of the tender participation rate and its price distribution skew. In the presence of unusual influences or when fair competition is threatened, the model will attempt to counteract the negative strategies adopted by tenderers, failing which a pre-assignment option built into the program allows the evaluator to make judgment outside the model.

The generalised price-scoring model produces two generic price model classes. The un-normalised class tend to produce price dominant effects while the normalised class tends to allow non-price attributes to have more influence in the overall evaluation. These two classes produce their own price ratio sub-class using a price gain derived from the ratio of the minimum tender price to a price, and their price difference sub-class derived from the price gain measure of a price with reference to the project budget. A survey of tender prices provides data for estimating the tender participation rate and the range of variations of the price distribution's coefficient of skewness to be used in the preference function. By appropriate choice of price gain function and of the preference function, 5 particular price-scoring models are derived. Price difference models are found to be better at discriminating prices than price ratio models. Price ratio models are more suitable for matching tender evaluation objectives that do not emphasise price. The combination of the value functions and the price gain functions with built-in cost control produces a diverse number of models for specific applications in a tender evaluation computer program.

Further investigation is required to test them with the non-price attributes in order to define their application in a tender evaluation procedure. The generalised price-scoring model hence, provides a means of studying the existing methods of tender evaluation by computer simulation. For example, comparisons can be made between an integrated approach in which price and other attributes are combined in a 1-stage evaluation procedure, and one in which price is evaluated after the evaluation of other non-price attributes is completed in a 2-stage evaluation procedure. ■

REFERENCES

[1] E. E. Karsak, Fuzzy MCDM Procedure for Evaluating Flexible Manufacturing System Alternatives, *Proceedings of the 2000 IEEE Engineering Management Society*, pp. 93-98, Albuquerque, New Mexico, USA, 2000.

[2] D. Hahneman and A. Tversky, Prospect theory: An Analysis of Decision Under Risk, *Econometrica Vol.74, pp.263-291, 1979*.

[3] A. Tversky and D. Hahneman, Advances in Prospect Theory: Cumulative Representation of Uncertainty, *Journal of Risk and Uncertainty Vol. 5, pp. 279-323, 1992*.

[4] W. S. Neilson and J. Stowe, A Further Examination of Cumulative Prospect Theory Parameterizations, *Journal of Risk and Uncertainty Vol. 24(1), pp. 31-46, Jan. 2002*.

[5] P. C. Thum, A Fuzzy Multiple Attribute Decision-Making Approach to Tender Evaluation, Journal, *The Institution of Engineers, Malaysia, Vol.64, No. 3, pp. Sept. 2003*.

[6] P. C. Thum and K. S. Rao, A Multi-level Implementation of a Fuzzy Tender Evaluation Procedure, *Journal, The Institution of Engineers, Malaysia, Vol.65, No.4, pp. Dec. 2003*.

[7] R. Hastie and R. M. Dawes, Chapter 13, Rational Choice in an Uncertain World: The Psychology of Judgment and Decision Making (Book), *Sage Publication, 2001*.

[8] S. Plous, The Psychology of Judgment and Decision Making (Book), *McGraw Hill, 1993*.

[9] T. Connolly, H. R. Arkes and K. R. Hammond, Judgment and Decision Making: An Interdisciplinary Reader (Book) 2nd Edition, *Cambridge University Press, 1999*.

[10] C. Starmer, Development in Non-Expected Utility Theory: The Hunt for a Descriptive Theory of Choice under Risk, *Journal of Economic Literature Vol. XXXVIII, pp.332-382, June 2000*.

[11] P. Bajari and L. Ye, Competition Versus Collusion in Procurement Auctions: Identification and Testing, *Stanford University Working Paper, 2001*.

[12] P. Bajari and G. Summers, Detecting Collusion in Procurement Auctions, *Antitrust Law Journal Vol. 70, pp. 143-170, 2002*.

[13] L. M. Froeb and M. Shor, Auctions, Evidence and Antitrust *in The Use of Econometrics In Antitrust, edited by John Harkrider, American Bar Association, 2003*.

NUMERICAL MODELLING OF REVERSE PULSE CLEANING ON RIGID CERAMIC FILTERS

T. G. Chuah[1], J. P. K. Seville[2] and C. J. Withers[3]

[1]*Department of Chemical and Environmental Engineering, Faculty of Engineering, Universiti Putra Malaysia, 43400 UPM, Serdang, Selangor.*

[2]*School of Chemical Engineering, The University of Birmingham, Edgbaston, Birmingham B15 2TT, UK*

[3]*Caldo Environmental Engineering Ltd, 1 Shire Business Park, Wainwright Road, Worcester, WR4 9FA, UK*

ABSTRACT

Many industrial processes involve the generation of waste gases and particulates. Environmental legislation enacted as a result of government policy has compelled industry to pay a serious attention to the air pollution issue. It has driven to the need to install air pollution control equipment. Rigid ceramic filters have proved themselves as highly efficient gas filtration devices in particles emission control. However, the filter cleaning mechanisms are still not fully understood. A computer program is developed to model the flow of the reverse pulse air from the cleaning bar nozzle to the dusty side of the filter. The program uses an iterative calculation mode of Microsoft Excel and allows variables such as reverse pulse pressure and filter geometry to be changed. Predictions are carried out on various pulse tube distances, temperatures of gas flow and various friction factors in order to study their effects on pressure distribution. The simulation is validated by data obtained from previous experiment works and fair agreement is achieved.

Keywords : *Gas Filtration, Ceramic Filter, Pulse Cleaning, Modelling, Flow Dynamics*

1.0 Introduction

Malaysia possesses a great potential market for hot gas cleaning technology. The country has made great strides in economic development during the last two decades. It is endowed with rich natural resources, such as oil and gas which provide the nation's energy requirements and a feedstock for the development of manufacturing and industry. Although Malaysia can be considered as one of the least polluted urban environments in Asia, rapid urbanisation and sustained economic growth together with the high demand for transportation have contributed towards air pollution issues. With the shift in the nation's strategy from that of agriculture towards manufacturing and heavy industries, a rapid increase in the generation of pollutants and wastes, which will result in the deterioration of air and water quality can be foreseen. The goal of the country to achieve industrial country status by the year 2020 and the associated industrial and urban expansion will further strain the environment in Malaysia. The problem of air pollution is particularly critical in urban industrial areas like Klang Valley. The deteriorating state of air quality in this area has been due to the presence of suspended particulates or dust generated by disposal of industrial, municipal and agricultural waste through open burning. Apart from these, the problem is also worsened by the emission from the power generation plants and by industrial combustion.

Rigid ceramic filters represent the most promising technology for particulate removal from process gases at high temperature [1]. Ceramic filters are normally used in the form of "candles": cylindrical tubes with permeable walls. Two generic types are available, with granular and fibrous structures. Effective cleaning of the filter element is as important as the filtration process and it is important to study the gas flow dynamics in the reverse flow mode in order to achieve better filter cleaning. Several studies have been carried out on pulse gas cleaning [2, 3, 4, 5]. All these studies have shown that the reverse pulse pressure is not usually uniformly distributed along the filter element. It is generally agreed that the pressure is greatest at the closed end of the candle and at a minimum, or even close to zero, at the open end.

In this paper, a new simulation method for predicting the flow field during the filter cleaning process is proposed. A computer program has been written to model the flow of the reverse pulse air, from the cleaning bar nozzle to the dirty side of the filter. The program uses an iterative calculation mode and allows variables such as pulse pressure and filter geometry to be changed. The model has been used to investigate the effect of the operational parameters and filter properties such as pulse tube distance, friction factor, pulse gas temperature, reverse pulse pressure and reverse flow rate on the pressure difference over the candle wall and axial velocity profile. The results are compared with the experimental data obtained from Mai *et al.* [6] and Stephen *et al.* [7].

2.0 Description of the Model

The simulation program includes calculation of the contributions of the nozzle jet and the entrained flow at the filter inlet; it then computes the gas volume flow rate through the orifice and along the filter element.

Figure 1 shows the flow maldistribution in a filter during filtration operation. Airflow from the cleaning bar is a function of reservoir pressure and hole diameter. The jet entrains more gas as it fans out towards the top of the filter element. At the

027-033·numerical modelling 9/20/05 12:18 PM Page 28

top of the element the gas mixture has an axial velocity which is a function of the airflow from the cleaning bar and the distance between the leaning bar and the filter element.

At the very bottom of the filter element the axial velocity is zero. The internal pressure at this point is equal to the velocity head at the top of the element minus the friction loss between the two points. This internal pressure causes the gas to flow radially out through the filter wall. The gas flow rate is a function of the permeability of the filter medium and the internal pressure.

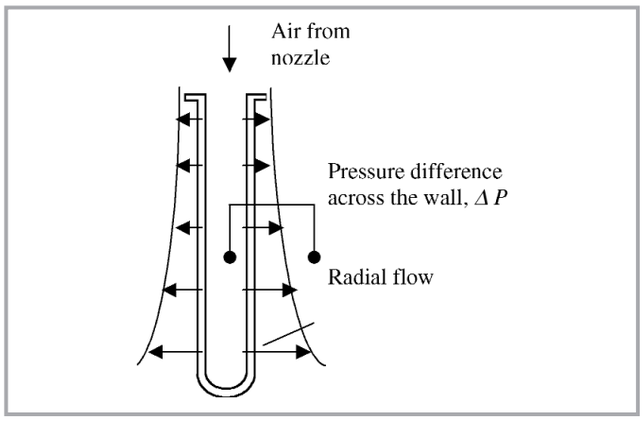

Figure 1: Flow maldistribution along filter during reverse pulse

The pressure drop across the wall is related to the resistance to flow of the filter medium and can be calculated using Darcy's Law for flow through a porous medium (in the appropriate form for a thick wall cylinder):

$$\Delta P = K\mu U\left[\ln\left(\frac{D_o}{Di}\right)\left(\frac{D_o}{2}\right)\right] \quad (1)$$

Where K is resistance of the filter medium, μ is the gas viscosity, D_o and D_i indicate the external and internal diameters of filter.

Just above the bottom of the filter, the axial velocity is greater than zero and the internal pressure is slightly less than at the very bottom. The internal pressure generates further radial flow, resulting in greater axial flow and a decrease in internal pressure at the next position up through to the top of element. The total radial flow is a function of the inlet velocity and medium permeability. Total radial flow cannot exceed the gas inlet flow. The mathematical description of this model is shown as follow.

a) Nozzle position and discharge rate

The optimum distance between the gas discharge orifice and the filter inlet, and the resulting gas flow rate through the orifice, are calculated based on basic fluid mechanics.

i) Distance from the nozzle to the filter element at optimum jet angle and perfect positioning (see Figure 2):

$$x = \frac{D_{or}}{2}\tan[((\alpha/2)/(360/2\pi))]^{1} \quad (2)$$

where jet angle, $\alpha = 20^{o}$ for $\frac{x}{D_{or}} < 100$

ii) Gas volumetric flow rate for sonic flow through orifice of cross-section area, A_o:

$$q = \frac{C_1 C A_{or}\rho_g}{\sqrt{T_g}} = \pi\frac{D_{or}^2 C_1 C\rho_g}{4\sqrt{T_g}} \quad (3)$$

where C, C_1 are dimensionless constants and T_g is the absolute temperature of the gas stream.

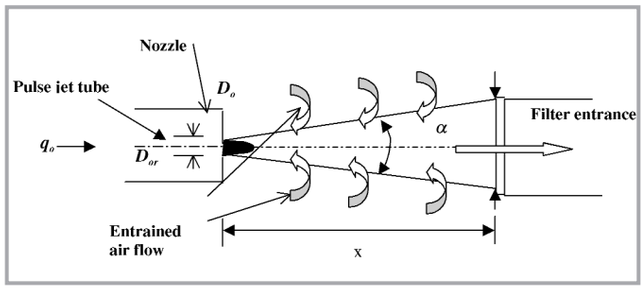

Figure 2: Schematic diagram of pulse gas flow for pulse jet tube and filter element

b) Filter inlet

The entrance flow rate and the gas velocity entering the element are calculated.

iii) Total gas flow Q_{total} at the entrance of the filter element:

$$Q_{total} = q_o(0.32)\frac{x}{D_o} \quad \text{for } 7 < \frac{x}{D_o} < 100 \quad (4)$$

where x is the distance from the nozzle to the filter entrance.

iv) Velocity at the entrance of the filter element:

$$U = \frac{Q}{A_f} \quad (5)$$

where A_f is the cross-sectional area at entrance of the filter.

v) Velocity head, static head equivalent of the kinetic energy in the stream of uniform velocity U_f (from Bernoulli's equation):

$$P_h = \frac{1}{2}U_f^2\rho_g \quad (6)$$

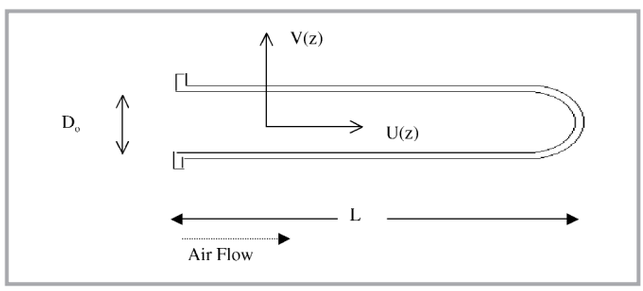

Figure 3: Schematic diagram of axial and radial directions flows in a filter

027-033·numerical modelling 9/20/05 12:18 PM Page 29

c) Filter tube

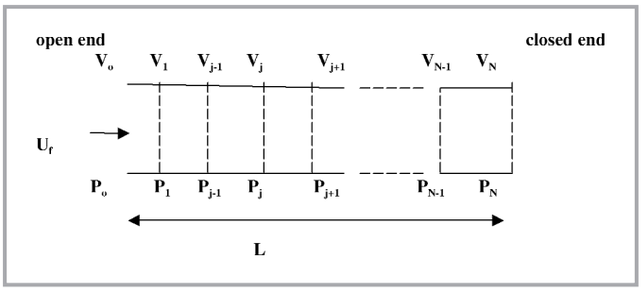

Figure 4: Description of flow in the filter element

The length of the filter L is divided into equally spaced nodes, N. Starting from Eq. (7) to Eq. (13), pressure distribution is estimated by iterative calculations of the parameters *V*, *U* and *P* along the filter element, taking into account element geometry and resistance. Boundary conditions, are (a) filtration pressure is provided at the inlet of the filter and (b) at the end of the filter, the volume flow rate is set to zero, i.e. no gas flow is permitted through the close end.

vi) Axial gas flow area, A_l:

$$A_{l,j} = \pi \frac{D_j^{\,2}}{4} \tag{7}$$

where D_j denotes the internal diameter of the filter at the position of the j-th node.

vii) Cylindrical surface area of radial gas flow at j-th node, A_R:

$$A_{R,j} = \pi l D_j \frac{L}{N-1} \tag{8}$$

viii) Gas differential volume flow rate through filter element wall, V:

$$V_j = \left[\frac{A_{R,j} \Delta P_j}{K} \right] \tag{9}$$

where subscript j denotes the variables are evaluated at node-j.

ix) Cumulative loss of gas flow rate through the filter element walls preceding node-j:

$$F_j = \sum_1^j V_j \tag{10}$$

since there is no flux through the end of the filter at $z=L$, $Q=\sum_1^N V_j$

x) Axial superficial gas velocity at j-th position

$$U_j = U - \frac{F_j}{A_{l,j}} \tag{11}$$

xi) Static equivalent velocity head at j-th position:

$$P_{h,j} = U_j^{\,2} \rho \tag{12}$$

xii) Static equivalent pressure head at j-th position

$$P_j = P_{hj} \tag{13}$$

3.0 Effect of Pulse Tube Distance

The model is used to investigate the effect of the pulse tube position, relative to the open-end of the filter candle, on the pressure difference along the filter element. Grannell [8] previously studied the optimisation of the pulse tube placement by experiments. Using this model, comparison with his data was carried out. For the purpose of this study, the Eq. (2) was neglected and a fixed value of the pulse tube distance, ***x***, was used in Eq. (4) for calculation of the total gas flow, Q_{total}, at the entrance to the filter element. Figure 5 shows the schematic diagram of the distance of the pulse tube position. ***x*** indicates the distance of pulse jet tube from the open end of the filter.

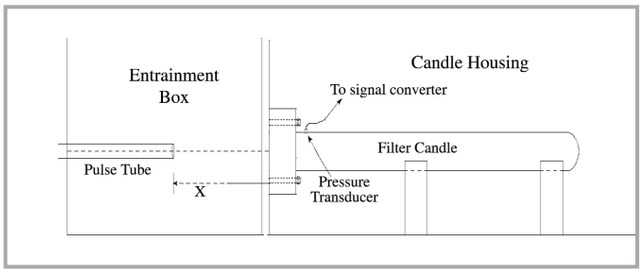

***Figure 5: Schematic diagram showing measurement of pulse tube distance* [8]**

Grannell [8] found that 13.5cm from the open end was the optimum distance for a 40 mm candle opening as this was the distance at which no "secondary" entrainment of gas occurred through the filter wall (for 4 bar cleaning pulse pressure).

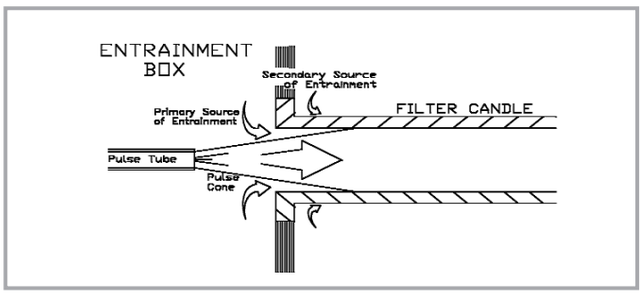

Figure 6: Pulse tube distance too short

Secondary entrainment is normally caused by the pulse tube being too close to the filter opening. As the gas was pulsed from the tube a large quantity of pulse gas extends into the filter. Secondary entrainment gas enters from the throat of the filter (Figure 6) in the opposite direction to the cleaning flow and will suck dusty gas through the round of throat of the filter. After several cycles of conditioning, dust cake will be retained around the open end of the filter and is difficult to detach [7].

Figure 7 shows the comparison between the simulation and the data obtained from Grannell's experiments. In his work, the

027-033·numerical modelling 9/20/05 12:19 PM Page 30

range of pulse tube distance over which the secondary entrainment occurred was between 8 and 14 cm.

Two pulse tube distances are used in this simulation, 12 and 13.5cm (optimum distance according to Grannell [8]). The simulation gave a good agreement with the experimental data. The model henceforth will be used to predict the effect of the tube distance on the pressure difference profile.

Figure 8 shows the effect of two different pulse tube distances, 8cm and 15cm, on the pressure difference profile. As the tube distance increases from 8cm to 12cm, the peak pressure at the closed end of the candle increased by 150%.

For a pulse tube distance of 15cm, the peak pressure increases by about 180% compared with the pressure at a pulse tube distance of 8cm. This increment in the pressure difference was due to a larger quantity of gas being forced into the filter flow at the greater tube distance. Larger axial velocities were converted into gas momentum and hence contributed to the pressure difference across the filter wall. However, as the distance increased, the rise of the pressure difference became less significant.

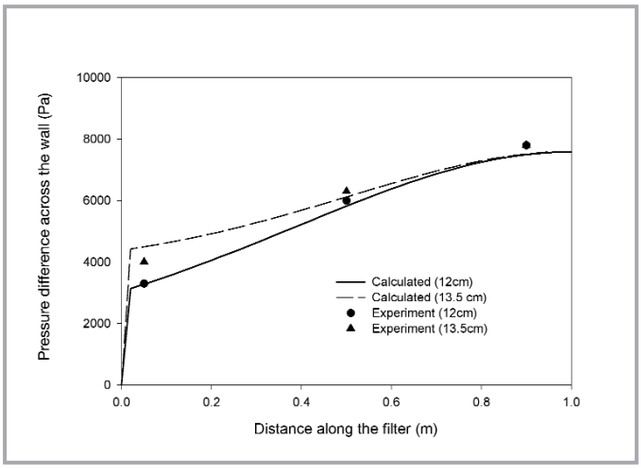

Figure 7:Comparison of the simulation and the experimental data with a pulse pressure of 4 bar

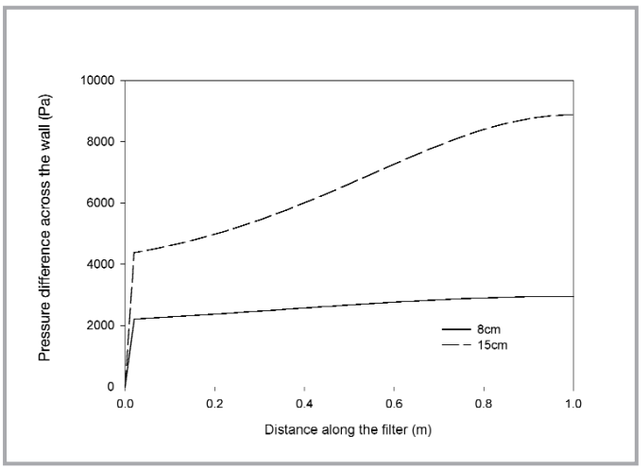

Figure 8:Effect of the pulse tube distance from the open end to the pressure difference with a pulse pressure of 4 bar

4.0 Effect of Friction Factor

Figure 9 shows the variation in the local pressure difference across the filter wall from the open end to the closed end using three different friction factors, 0.01, 0.05 and 0.1 respectively (corresponding to a surface roughness of 1mm, 6.5mm and 15mm respectively, calculated by Colebrook-White equation [9]. For the flow in the filter with a friction factor of 0.01, it can be seen that local pressure difference across the wall increases from the open end to the closed end. A different outcome was noticed for the case when the internal wall friction was 0.05; the local pressure difference across the wall now decreased with increasing distance from the open end of the filter. Increasing friction factor will hence reduce the pressure drop as described in Eq. (14).

$$\frac{dP}{dz}+\frac{1}{2}\frac{d}{dz}(\rho u_z^{\,2})=-4\frac{f}{D_i}\frac{1}{2}\rho u_z^{\,2} \qquad (14)$$

However, the profile of the decrement of the pressure difference was not continuous; it passes through a minimum before the closed end was reached. The effect of the friction was also noticed when the friction factor was increased to 0.1.

There was an initial decrease in the pressure difference across the wall at the open end; this reached a minimum at a distance 70cm from the open end. There was a slight increment in the pressure difference across the filter wall close to the closed end.

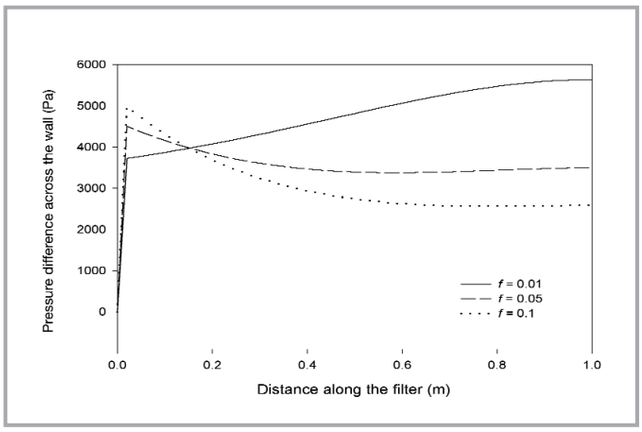

Figure 9: Effect of the friction factor on the pressure difference profile with a reverse pulse pressure 4 bar

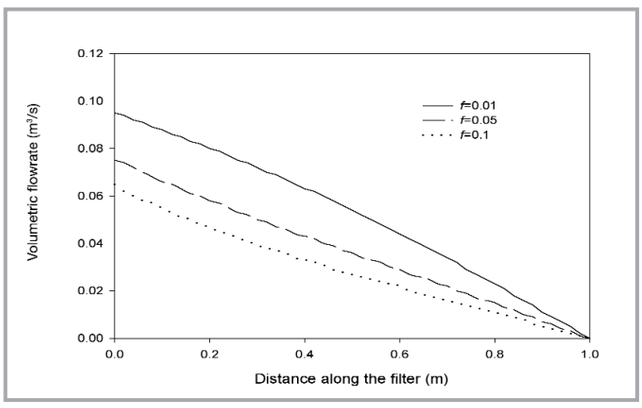

Figure 10: Effect of the friction factor on the pressure difference profile with a reverse pulse pressure of 4 bar

027-033·numerical modelling 9/20/05 12:19 PM Page 31

Figure 10 shows the changes of volumetric flowrate along the filter candle for different friction factors. At higher friction factor, greater volumetric flow rate decreased from the open end of the filter towards the closed end of the filter. As the gas flow travelled along the filter from the open end to the closed end of the filter, the axial velocity was recovered as static head, thus increasing the pressure difference across the wall. The volumetric flow rate was decreased monotonically to reach zero at the closed end. For friction factors of 0.05 and 0.1, with a large volumetric flowrate at the open end, the frictional effects are large and the pressure difference across the wall was decreased. However, at a distance of 60cm from the open end, the pressure drop caused by friction is reduced because the volumetric flow is then small and makes little contribution to the pressure difference across the wall. The loss of momentum of gas flow then dominates the axial pressure drop and pressure recovery occurs. The frictional pressure drop scales with Q^2. Hence, as Q decreases, the contribution of the frictional terms reduces strongly.

5.0 Effect of Temperatures

An important concern in filter cleaning is the progressive loss in filter strength with use. The thermal stress set up during pulse cleaning will weaken the ceramic substrate of the filters. For the cleaning process, a high temperature jet of gas can be reverse pulsed through the hot ceramic filter, this should be at a temperature greater than ambient. This is to avoid the thermal stresses set up during pulse cleaning which will weaken the ceramic substrate. Research at University of Aachen [10] has confirmed that a severe temperature transient occurs during pulse cleaning when using `cold' pulse gas. To reduce this problem, Biffin *et al.* [11] has carried the experiments by re-entrained filtered hot gas to use for filter pulse cleaning by introducing a venturi educer.

Figure 11 shows the effect of the pulse jet gas temperature on the pressure difference profile along the filter element. When the temperature of the jet gas was increased, from 20ºC to 200ºoC, the pressure difference increased by 23% at the open end and 15% at the closed end of the filter. However, at the higher temperatures, 300ºC and 400ºC, the open end pressure differences were 32% and 38% respectively higher than at 20ºC, with very little increment in the pressure difference at the closed end.

At 20ºC, the local pressure increased with increasing distance from the open end of the filter candle, but the change of local pressure was reduced at higher temperatures and was not significant. At a temperature of 20ºC, the pressure difference increased 63% from the open end to the closed end, whist at 300ºC and 400ºC the pressure difference at the closed end was only 35% and 30% higher from the open end respectively.

Increasing temperature will increase the gas viscosity and hence will increase the pressure drop across the filter wall. But at the same time the gas density will decrease with increasing temperature and hence reduce the pressure changes along the filter candle, which are largely due to momentum effects. The combination of these effects tends to reduce non-uniformity, as shown in Figure 11.

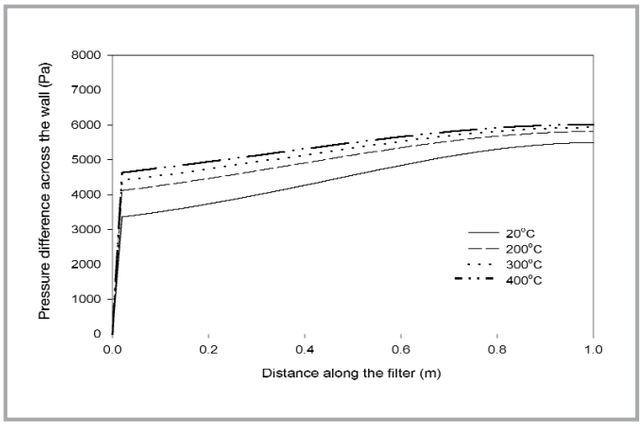

Figure 11: Effect of pulse jet temperatures on pressure difference profile

6.0 Comparison with Previous Work

In order to assess the accuracy of the model, the results were compared with experimental data obtained from previous studies [6, 7].

6.1 Comparison with the DIA-Schumalith F40 Filter Candle [6]

The pressure distribution in the candle elements is shown in Figure 12 in which the pulse cleaning pressure was 5 bar. Inside the filter candle, continuous outflow in a radial direction reduces the axial velocity. Kinetic energy is then converted into pressure energy, so that the pressure increases approaching the closed end of the candle. The simulation shows good agreement with the measurements for the positions 15 and 50cm, but overestimated the pressure at the closed end, presumably because not all the kinetic energy was recovered as pressure.

One factor here is that the Excel simulation neglects pressure loss due to frictional effects. Inadequate fitting of the model near the closed end could also be the result of the influence of the unequal distribution of porosity and resistance along the filter candle elements. Strong local pressure fluctuations during the measurements can also lead to errors, usually reducing the accuracy of the measured pressure difference. Only 3 measurement points were used in these studies; more data should be provided in order to get a better comparison.

6.2 Comparison with Cerafil-S Filter Candles [7]

Figures 13 shows the pressure profiles along the filter elements with pulse cleaning pressures of 4 bar at an initial (pre cleaning) filtration pressure difference of 550 Pa. The pressure difference predicted from the simulation was lower than the experimental data obtained from Stephen *et al.* [7]. The difference could be because of the experimental set up, *e.g.* the distance of the pulse tube from the open end of the filter and the filter resistance may be different from the current simulation.

027-033·numerical modelling 9/20/05 12:19 PM Page 32

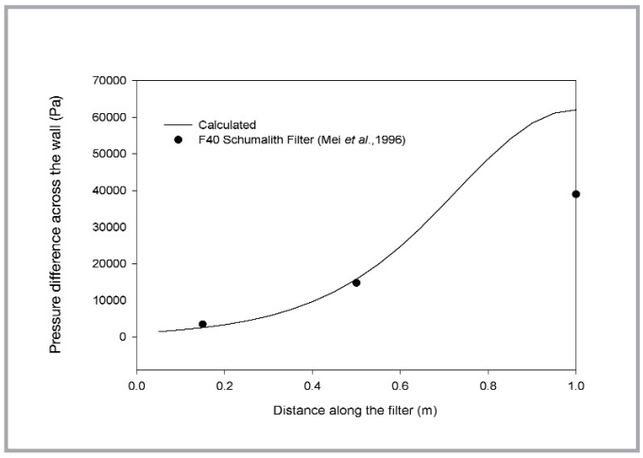

Figure 12: Distribution of cleaning pressure in a DIA-Schumalith F40 filter

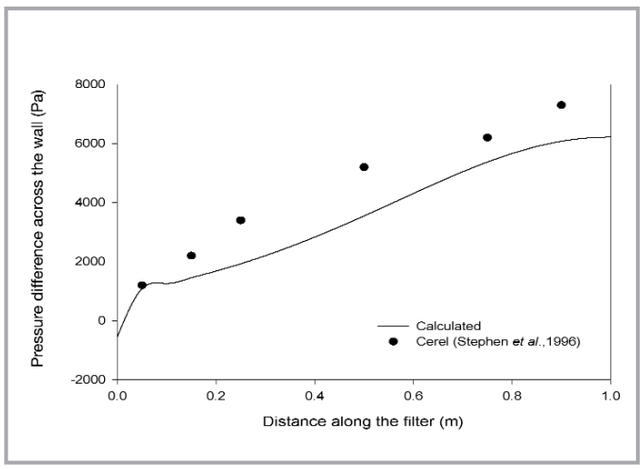

Figure 13: Pressure distribution on a Cerafil filter candle with a 4 bar pulse pressure (filtration pressure 550Pa)

7.0 Conclusions

The mathematical model seems able to predict the pressure drop and velocity profile along a filter element during reverse flow cleaning. Simulations showed the distance of the pulse tube had an effect on the cleaning pressure distribution. A large pulse tube distance will increase the pressure difference in the filter due to the larger volumetric gas flow that has been converted into gas momentum and contributes to the pressure difference across the filter wall. At larger distances, the increment of the pressure difference became less significant.

The simulation also showed that at higher friction factors, the pressure difference across the filter wall did not decrease continuously; it passed through a minimum before the closed end was reached. For higher friction factors, with a large volumetric flowrate at the open end, the friction dominated and the pressure difference across the wall was decreased.

Increasing temperature increases the gas viscosity, thus, the pressure drop across the filter also increased. However, the gas density decreased with increasing temperature, hence reducing the pressure changes along the filter candle. The combination of effects makes the pressure difference across the wall more uniform. ■

Nomenclatures

A_l : Axial gas flow area (m^2)
A_{or} : Cross section area of nozzle (m^2)
A_R : Cylindrical surface area of radial gas flow (m^2)
C : Coefficient of discharge, normally taken as 0.99
C_l : Dimensional constant, 0.0405 (SI units)
D_i : Filter internal diameter (m)
D_o : Filter external diameter (m)
D_{or} : Nozzle diameter (m)
F : Cumulative flow rate through filter element (m^3)
K : Resistance to flow (m^{-1})
L : Length of filter element (m)
P : Pressure (Pa)
P_h : Velocity head (Pa)
P_o : Ambient pressure from surrounding filter element (Pa)
ΔP : Pressure difference (Pa)
Q_{total} : Total gas volumetric flow rate into the filter (m^3s^{-1})
q_o : Gas volumetric flow rate through nozzle (kgs^{-1})
T_g : Absolute gas temperature, (K)
U : Gas velocity (ms^{-1})
V : Gas volume flow rate (m^3s^{-1})
x : Distance from orifice to filter element (m)
z : Position along the candle
ρ : Gas density (kgm^{-3})
α : Jet gas angle, ^{o}

Subscripts

f : filter element
g : gas (air)
j : position along filter element
N : position along filter element

REFERENCES

1. Seville J. P. K. (1997). "Rigid Ceramic Filters" in "Gas Cleaning in Demanding Applications". Seville, J. P. K. (editor), Blackie Academic and Professional, Glasgow, pp. 96-129.
2. Berbner, S., Löffler, F.(1993). "Pulse Cleaning of Rigid Ceramic Filter Elements at High Temperatures" in "Gas Cleaning at High Temperature" R.Clift and J.P.K. Seville (Eds.), Blackie Academic & Professional, Glasgow, pp. 225-243.
3. Laux, S., Giernoth, B., Bulak, H., Renz, U. (1993). "Aspects of Pulse-Jet Cleaning of Ceramic Filter Elements" in "Gas Cleaning at High Temperatures" R.Clift and J.P.K. Seville (Eds.), Blackie Academic & Professional, Glasgow, pp.203-224.
4. Ito, S. (1993). "Pulse Jet Cleaning and Internal Flow in a Large Ceramic Tube Filter", in "Gas Cleaning at High Temperatures", R.Clift and J.P.K. Seville (Eds.), Blackie Academic & Professional, Glasgow, pp. 266-279.
5. Chuah, T. G., Withers, C. J., Burbidge, A. S., Seville, J. P. K.(1999). "Numerical Modelling of Reverse Pulse Cleaning" in "High Temperature Gas Cleaning", A. Dittler, G. Hemmer, G. Kasper (Eds.), Institut für Mechanische Verfahrenstechnik und Mechanik der Universität Karlsruhe (TH), Karlsruhe, Glasgow, pp. 185-199.

027-033·numerical modelling 9/20/05 12:19 PM Page 33

6. Mai, R., Fronhöfer, M. and Leibold, H. (1996). "Flow Charcteristics of Filter Candles During Recleaning" in "High Temperature Gas Cleaning", Schmidt, Gäng, Pitt, Ditter (eds.), Institut für MUM, Universität Karlsruhe(TH), Karlsruhe, pp.194-206.
7. Stephen, C.M., Grannell, S.K., Seville, J.P.K. (1996), "Conditioning and Pulse-Cleaning of Rigid Ceramic Filters", in "High Temperature Gas Cleaning", E. Schmidt, *et al.* (eds), Institut für Mechanische Verfahrenstechnik und Mechhanik der Universität Karlsruhe (TH), Karlsruhe, pp. 207-218.
8. Grannell, S. K. (1998). "The Industry Application of Low Density Rigid Ceramic Filters for Hot Gas Cleaning". PhD Thesis, University of Birmingham.
9. Kay, J. M. and Nedderman, R. M. (1985). "Fluid Mechanics and Transfer Processes". Cambridge University Press, Cambridge, pp. 544-547.
10. Schiffer, H. P., Renz, U. and Tassicker, O.J. (1989). "Hot Gas Filtration Research at RWTH Aachen PFBC Facilities". Trans. ASME, 1, pp. 487-494.
11. Biffin, M., Panagiotidis, P. and Pitsillides, C. (1997). "Velocity Measurements in a Ceramic Filter Element Undergoing Pulse Cleaning". Proceeding of the Institute of Mechanical Engineers, Part E: Journal of Process Mechanical Engineering, 211, E1, pp.11-16.

Appendix 1

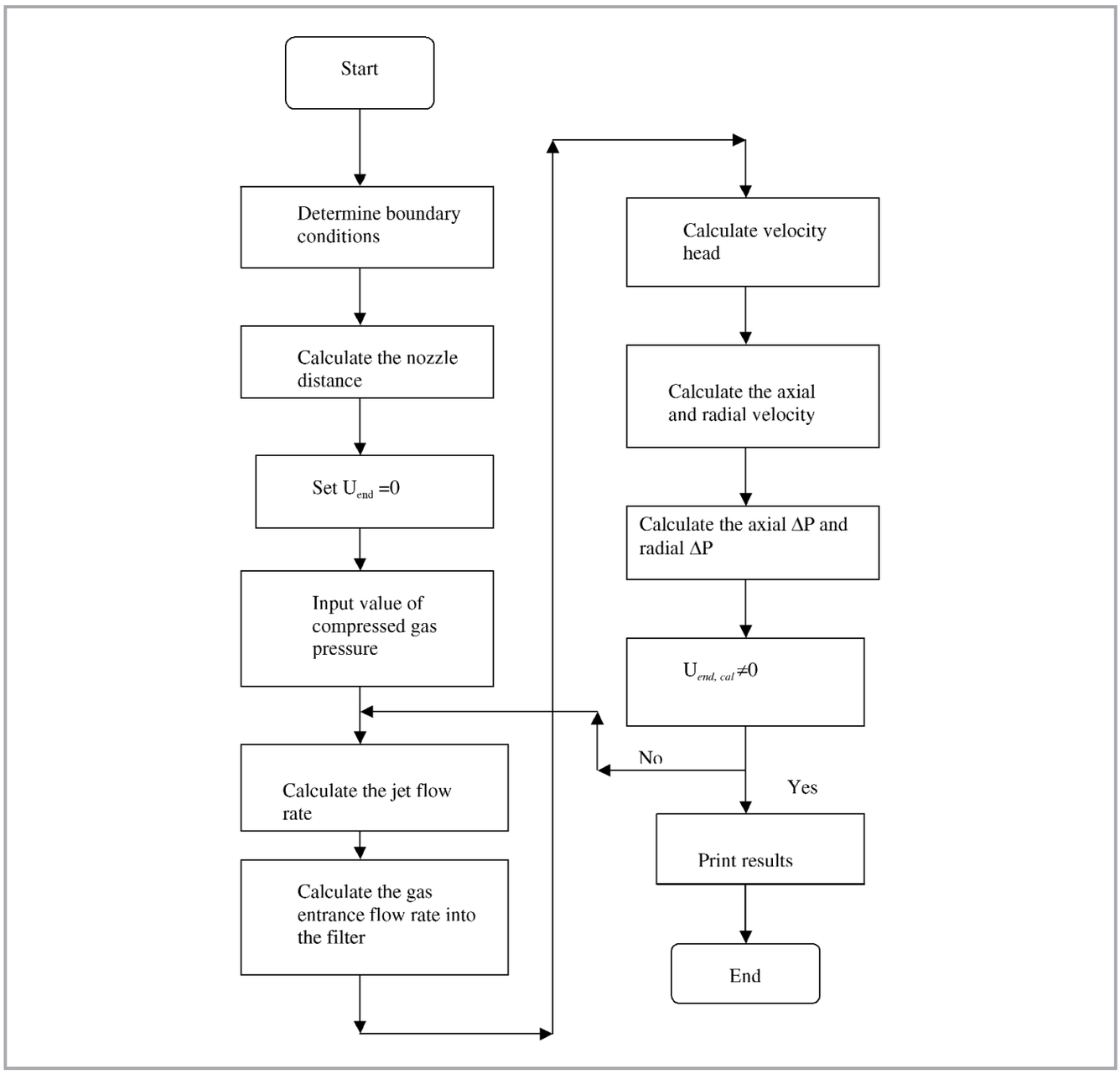

Figure A-1: Flow chart of the model

A METHODOLOGY TO EVALUATE DESIGN EFFICIENCY BASED ON ASSEMBLY CRITERIA IN SUPPORT OF DESIGN FOR MODULARITY

A. B. Abdullah, Z. M. Ripin and M. Mokhtar
School of Mechanical Engineering, Universiti Sains Malaysia, Engineering Campus, 14300 Nibong Tebal, SPS, Penang

ABSTRACT

The objective of this paper is to develop a new methodology for evaluating design efficiency based on assembly criteria. The new methodology can be utilised to support the design for modularity approach. The verification of the new approach was carried out by redesigning an electrical table fan parts and components. A modularity design approach which focuses on the seven main mechanical assembly and seven assembly criteria was exploited. The result indicates an improvement of the overall design efficiency of the table fan. The paper emphasises that through modularity approach, complexity of the product can be reduced.

Keywords: *Assembly Criteria, Design for Modularity, Design Efficiency*

1.0 INTRODUCTION

Companies are striving to produce high quality and reliable product at the lowest cost to remain competitive in the market. Several approaches, methodologies and tools were developed to fulfill this objective. The most important and crucial stage in the product design is the efficiency evaluation and validation phase. Rating the products allows efficiency to be evaluated, so that the potential of product improvement can be identified. Most of the current evaluation methods are not taking into consideration types of assembly or joining method used on a product. The type of assembly method or joining technique used has a significant effect on the product rating. In manual assembly, only the number of components and type of assembly can be directly known, whereas assembly time cannot be measured consistently.

Assembly typically constitutes 40% – 60% of overall production time [1]. Boothroyd and Dewhurst [2] listed several ideal assembly characteristics such as minimise assembly direction and allow simple aligning, orientation and handling of parts. They also had proposed a free-tools assembly that excludes fixtures during the assembly [2]. Although the characteristics of the assembly are fulfilled, there is an influence of the tools fixtures during the disassembly process as indicated by Lily and Flowers [3]. Complete disassembly depends on material used, assembly direction, type of mechanical joint and tool used either in assembly or disassembly processes [4], hence the need to evaluate design efficiency based on assembly criteria can be considered as an important factor for the assembly process.

The objective of this paper is to develop a new methodology to evaluate design efficiency based on assembly criteria such as tools used, cost of the tools, assembly direction, orientation and other related factors. In this work, seven main mechanical assemblies are presented and seven assembly criteria are taken into considerations for product redesigning purposes. As a result a new simpler methodology that can evaluate design efficiency effectively was developed.

The paper is organised into few sections, where section one outline the overview of the assembly process. Section two provides some literature review and the motivation of the research. The methodology of the research is presented in section three and in order to implement the approach an illustration example is discuss in section four. Section five discusses the results of the developed approach and the paper ends with a conclusion and some suggestions for future work.

2.0 MECHANICAL ASSEMBLY

One of the potential benefits from modularity is the characteristics of sharing assembly structure [5]. Assembly can be described as a process of joining together several components to create a final product [6] by mechanical, cohesive or adhesive methods. Components generally need assembly to complete the system. For example, a typical automobile has more than 15,000 parts, which are all assembled by using several joining methods as shown in Figure 1.

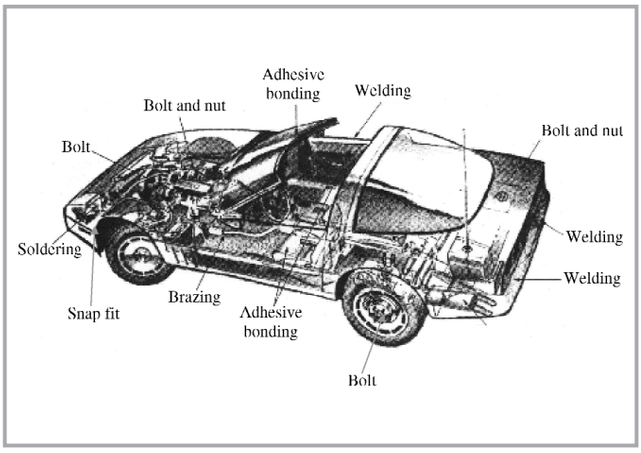

Figure 1: Thousand of assembly needed for automobile [7]

There are several factors to be considered in selecting types of mechanical assembly. The factor involve is whether the components are join permanently or some times need to be dissembled for servicing, repair or recycling. Another factor is simplifying the product and component assembly such as designing components with uni-directional assembly is preferable than multi-directional assembly. Strength of the assembly must also be able to withstand forces. For example components assembled on the compressor tank must have the capability to withstand internal force of compressed air in order to ensure production of compressed air. In assembly process, tool is commonly used, but assembly without the aid of the tool is better because tool setup time can be reduces thus reduce assembly time.

Generally there are ten types of mechanical assembly as shown in Figure 2, but in this work, they are clustered into seven groups. This clustering is possible because welding, soldering and brazing which have similar characteristics can be grouped into one namely cohesive, while spring clip and metal stitching can be grouped as stitch.

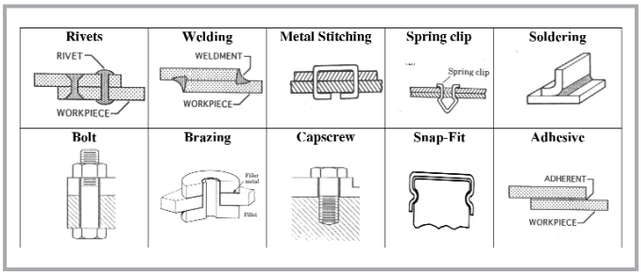

Figure 2: Ten types of conventional mechanical joint [6, 7]

3.0 METHODOLOGY

The methodology consists of three main steps, which are problem definition, assembly criteria and design evaluation.

3.1 Problem Definition

In design process, problem definition is very important, so that the root of the problem can be understood clearly [6]. Decomposition is one of the best methods to identify problem. Decomposition of physical or structure of the component tends to make the identification of the problem easier.

3.2 Definition of Assembly Criteria

From the literature [1,2,3], there are seven assembly criteria that have been identified.

All these criteria are listed and weighted based on the mechanical joint listed in section 2.0. The seven assembly criteria that have been identified are;

1. Tooling – Assembly operation requiring tools, such as for attaching snap rings, springs or cotter pins. The types of tools utilised could either be standard tools, special tools or no tools required.

2. Assembly direction – Ideal assembly orientation is parts which are inserted from the top of the assembly direction or z-axis assembly. By using z-axis assembly for all parts, the assembly would not to be inverted, gravity will help to stabilise the partial assembly and the operator can easily access the assemble parts.

3. Costing - Cost involved are the cost of typical tools used, for example assembly using welding technique requires expensive equipment compare to the other mechanical assembly such as mechanical stitch, rivet or bolt and nut which are more cheaper.

4. Durability – This criterion is related to the capability of the assembled parts to withstand during application, for example cylinder head, which needs higher strength joint.

5. Recycleability – The characteristics of material such as recyclable, toxic, cost etc. are being considered here. Normally disassembled parts can be recycled completely. The similarities of the component material in the assembly also give advantages to the product.

6. Perpetualability – Mechanical assembly such as bolted joint is a semi-permanent joint, whereas adhesive and cohesive is considered as a permanent joint. For ease of parts removal, semi-permanent joint is more preferable.

7. Manufacturability – This criterion is related to the type of device used in the assembly process, whether standard or custom-made. For example bolt and screw is a standard device but for the mechanical stitch or spring clip, it needs to be specially designed for certain snap-fit assembly or application.

Score of 1, 3 and 5 are given for the assembly criteria to represent the weightage for the assembly types in Table 1. The score for each assembly criteria is given as shown in Table 1(a) – 1(g). This weightage depends on where the joining method is applied and so that the designer can justify and make decision on which type of assembly should be selected.

3.3 Design Evaluation

Expressions are derived to measure the design efficiency by relating number of components, number of assembly and total score. A calculation formula for design efficiency (E) is as follows:

$$\text{Design Efficiency, } E = \frac{1}{V_n}\left(\frac{\sum_{N_A}^{i=1} W_T}{N_c}\right) \qquad (1)$$

(Note that $N_A \geq 1$, number of assembly criteria depends on the design requirement, which is usually more than one). V_n is number of criteria, for this case $V_n = 7$.

The total score can be expressed as follows:

$$\text{Total Score, } W_T = \sum_{i=1}^{A_n} r_i \qquad (2)$$

Where A_n = Number of assembly

r = Score for each sub-assembly

P_n = Number of components,

Number of components, N_c and number of assembly, N_A are directly obtain from the disassembly and the total score, W_T of each component assembly is the result of product assembly.

034-040·methodology 9/20/05 12:24 PM Page 36

Table 1: Assembly characteristics and generalise weightage

Type of Assembly	Costing	Tooling	Perpetualability	Durability	Recycleability	Direction	Manufacturability
Capsrew	Low	Common	Semi-permanent	High	Recyclable	Uni-direction	Standard
Bolt	Low	Common	Semi-permanent	High	Recyclable	Uni-direction	Standard
Rivet	Low	Special tool	Permanent	Medium	Recyclable	Uni-direction	Standard
Snap fit	Low	No	Semi-permanent	Medium	Recyclable	Uni-direction	Custom-made
Stitch	Low	No	Semi-permanent	Medium	Recyclable	Uni-direction	Standard
Cohesive	Medium	Special tool	Permanent	High	Non-recyclable	Multi-direction	Standard
Adhesive	Low	No	Permanent	High	Non-recyclable	Multi-direction	Standard

Table 1 (a)

Cost	Rating
Low	1
Medium	3
High	5

Table 1 (b)

Tool	Rating
No tool required	1
Common tool	3
Special tool	5

Table 1 (c)

Joining	Rating
Semi-permanet	1
Permanent	3

Table 1 (d)

Strength	Rating
High	1
Medium	3
Low	5

Table 1 (e)

Manufacturing	Rating
Standard	1
Custom made	3

Table 1 (f)

Direction	Rating
Uni-direction	1
Bi-direction	3
Multi-direction	5

Table 1 (g)

Material	Rating
Recyclable	1
Non-recyclable	3

4.0 IMPLEMENTATION

Case Study – Table Fan

Table fan is one of the commonly devices used by most of the people to blow air to a targeted area. The schematic diagram of a table fan is shown in Figure 3. It has 19 components including the oscillation knob and motor, which are not shown in the diagram.

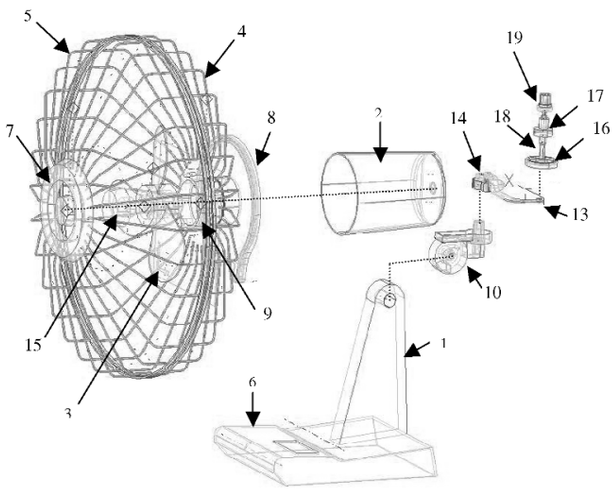

Components	Material	Components	Material
1. Stand	Plastic	11. Switch Panel	Plastic + Steel
2. Motor housing	Plastic	12. Motor	Steel
3. Fan blade	Plastic	13. Oscillator control device	Plastic
4. Rear guard grill	Steel	14. Oscillator control plate	Plastic
5. Front guard grill	Steel	15. Spinner	Plastic
6. Base cover	Plastic	16. Oscillator gear 1	Plastic
7. Decorative face plate	Plastic	17. Oscillator gear 2	Plastic
8. Guard lock nut mounter	Plastic	18. Oscillator gear 3	Plastic
9. Guard lock nut	Plastic	19. Knob control	Plastic
10. Neck	Plastic		

Figure 3: An exploded view of table fan with components and material listing

034-040·methodology 9/20/05 12:24 PM Page 37

Figure 4 illustrates the components mapped in the form of assembly digraph to show the interaction and joining method between each component. Arrows devotes the assembly direction, numbers in bracket indicate number of screws and bolt used in joining the components. Note that identical parts assembled at the same time and having the same assembly characteristics (e.g. four screws need to fasten a single component to another) are assigned as different number of assembly.

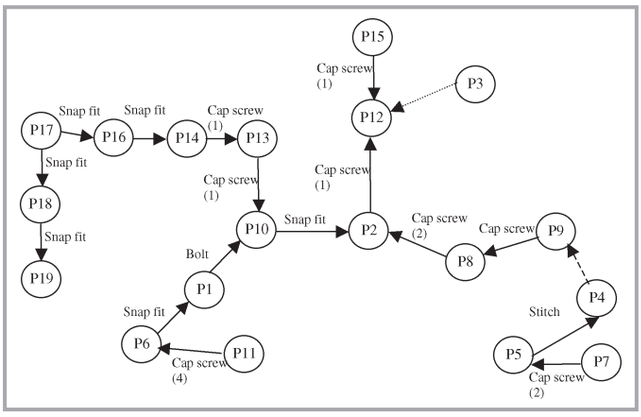

Figure 4: Assembly digraph of the tale fan

5.0 REDESIGN PROCESS

Similar to the original design, redesign also includes the process of gathering customer needs, planning and development, concept generation, embodiment design and the final phase is testing and prototyping. Here one additional step, which is reverse engineering [9], is introduced. In redesign process, a product is predicted, observed, disassembled, analysed, tested, experienced and documented in terms of its functionality, form, physical principles, manufacturability and assemblability [10].

In this work, redesign is carried in order to verify the design efficiency. Through reducing part number, modifying/changing the required operations such as joining method it can increase the design efficiency [11]. The modularity approach is introduced in order to clustering the components at the higher interaction and separating from the loose interactions component to easily identification of detached modules that could assist recycle, redesign or service purposed. For example, components in a product that are made from different material, which have different life duration and required different recycling and disposal methods. By using modular approach, components of similar material can be grouped into same module. The disassembly process flow chart is shown in Figure 5.

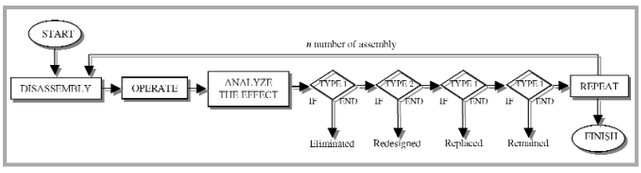

Figure 5: The extended substrate operate procedure (SOP) flow chart

The redesign process is based on the Subtract Operate Procedure (SOP) developed by Lefever and Wood [11]. In this procedure every single component in the product is disassembled one by one to find the effect of disassembling towards the product. From the analysis, components that can be eliminated, redesigned or remained can be identified. Note that components must be reassembled after analysing the effect. For the components that cannot be disassembled are considered as single components. Table 6 simplifies the result from the SOP procedure. In the disassembly analysis, there are three levels of effects, which are no effect, effect and strong effect. The three level of effect is based on the effect, which reflects to the product or system functionality when it is being disassembly, for example front and rear guard grill, there are no effect due to the disassembly to the product or system. The components is consider to have an effect to the system, but not the functionality of the product, for example control knob can only effect the oscillation system of the fan but not the main function of the fan. Strongly effected parts can led to the overall system of the fan to malfunction due to removal of the parts.

(A) Extended SOP Algorithm

There are eight steps involve in the SOP process.

Step 1: *Disassembly*, can be defined as the process of systematic removal of desirable constitute parts from an assembly while ensuring that there is no impairment of parts due to the process [12]. In this case one component is disassembling while constraint 1 must be fulfilled. If not, constraint 2 can be considered as other alternatives.

Step 2: *Operation*, The product is tested through full range of customer needs and engineering requirements.

Step 3: *Analyse*, The effects can be completed through visual analysis or tools for the case of non-obvious effects based on the four types of classifications.

Step 4: *Elimination*, If fulfilling type 1.

Step 5: *Redesigned*, If fulfilling type 2.

Step 6: *Replacement*, If fulfilling type 3.

Step 7: *Remained*, If fulfilling type 4.

Step 8: *Repetition*, Repeat the procedure in *n* times, where *n* is number of components in the products.

Two conditions of the assembly that taken into considerations.

Condition 1: The functionally dependent components must be reassembled.

Condition 2: The component that cannot be disassembled is considered as one component.

Types of effect are listed as followed;

Type 1: Those components causing no change in the Degree of Freedom (DOF) as well as no other effects can be eliminated from the design.

Type 2: Those components causing no change in the Degree of Freedom (DOF), but can effects due to their removal, can be parametrically redesigned to compensate for these effects.

034-040·methodology 9/20/05 12:24 PM Page 38

Table 2: SOP Worksheet

Disassembly Sequence	Qty.	Components Name	Effect	Comment
1	1	Decorative face plate	No effect	Change front guard grill design
2	1	Front guard grill	No effect	Unsafe to used
3	1	Spinner	Strongly Effected	Mounting fan blade
4	1	Fan blade	Strongly Effected	Generate comfort air
5	1	Guard lock nut	No effect	New joining method to mount rear guard grill
6	1	Rear guard grill	No effect	Unsafe to used
7	1	Guard lock nut mounter	No effect	New joining method to mount guard lock nut
8	1	Knob Control	Effected	Oscillation system
9	1	Motor housing	No effect	Motor open to air (unsafe)
10	1	Oscillator gear 2	Effected	Oscillation system
11	1	Oscillator gear 3	Effected	Oscillation system
12	1	Oscillator gear 1	Effected	Oscillation system
13	1	Oscillator control device	Effected	Oscillation system
14	1	Oscillator control plate	Effected	Oscillation system
15	1	Motor	Strongly Effected	Motoring system
16	1	Neck	Strongly Effected	Connect body to stand
17	1	Switch Panel	Strongly Effected	Switching system
18	1	Stand	Strongly Effected	Main structure
19	1	Stable base	No effect	Shift switch panel location

Type 3: Those components causing changes in the Degree of Freedom (DOF) but has as no other effects can be replaced by another components.

Type 4: Those components causing changes in the Degree of Freedom (DOF) and have other effects must be remained in the design.

From Table 2, there are seven components, which have no effect (disassembly sequence 1,2,5,6,7,9,19), six components with effect (disassembly sequence 8,10,11,12,13,14) and six components with strong effect (disassembly sequence 3,4,15,16,17,18). Only not effected components are now focused without contemplating the safety factor.

As a result three components out of seven not affecting the components are selected as a potential component to be redesigned, the guard lock nut, decorative faceplate and base. Figure 8, shows the guard lock nut before and after redesigning the guard lock nut mounter. The mounter is eliminated resulting in changing of joining method of rear guard grill from screw to snap fit. There are three options in selecting new joint method, and based on the assembly weightage discussed before, the snap-fit joining method gives better result in terms of ease of disassembly. Similarly to the case of the decorative face-plate where screws is change into snap fit assembly method. Base ground cover was also found to be unimportant and does not affect the overall product functionality, so that it can be eliminated. Other changes are on the location of switch panel, which is shifted to the stand that allows for better product commonality.

(B) Design for Modularity Approach

The emphasis of modular design is to identify module and various modular design methods have been proposed quantitatively and qualitatively. Many researchers have discussed on these topics and it will not be repeated. In this work, two approaches are presented as a combination to fulfill the material compatibility and assembly criterion, which are done by Gershenson et al. [13] and Huang and Kusiak [14]. The former defines modularity in life-cycle point of view and modules are developed based on components-process similarity and dependency and the latter focus on the assembly incidence and interaction between components to identify modules.

Based on methodology developed by Gershenson et al. [13], modules can be identified from material similarity and dependency. Due to its length, the steps involved in module identification are not discussed. Components are mapped in interaction matrix (Figure 6). As a result, four modules are identified as shown in Figure 7 after rearrangement.

	1	2	3	4	5	6	7	8	9	10	11	12	13	14	15	16	17	18	19
1	x					1				1									
2		x						1		1		1							
3			x									1			1				
4				x	1				1										
5				1	x		1												
6	1					x					1								
7					1		x												
8		1						x	1										
9				1				1	x										
10	1	1								x			1						
11						1					x								
12		1	1									x			1				
13										1			x	1					
14													1	x		1			
15			1									1			x				
16														1		x	1		
17																1	x	1	
18																	1	x	1
19																		1	x

Figure 6: Interaction matric, M_A

034-040·methodology 9/20/05 12:24 PM Page 39

	1	2	6	10	11	4	5	7	8	9	12	15	13	14	16	17	18	19	3
1	x		1	1															
2		x		1					1		1								
6	1		x		1														
10	1	1		x									1						
11			1		x														
4						x	1			1									
5						1	x	1											
7							1	x											
8		1							x	1									
9						1			1	x									
12		1									x	1							1
15											1	x							1
13				1									x	1					
14													1	x	1				
16														1	x	1			
17															1	x	1		
18																1	x	1	
19																	1	x	
3											1	1							x

Figure 7: Modularity matrix, M_M

Module 1: Front guard, rear guard and decorative plate.

Module 2: Neck, stand, switch panel and base.

Module 3: Oscillating controls device, oscillator control plate, gear 1, gear 2, gear 3 and control knob.

Module 4: Guard lock nut, motor and housing
Standard parts: Fan blade and spinner.

6.0 RESULTS AND DISCUSSION

The overall result shows that the percentage of the overall design efficiency has increased. This can be interpreted as an improvement of the product efficiency as shown in Table 3. Although the reduction of parts count was quite small (only two components), but due to the changes of the fastening method, product efficiency can be improvement a lot. Numbers of modules are increase leading to a reduction of component complexity and the number of standard parts is also increase as the base is removed from the stand module.

Table 3: New table fan design improvement

Parameter	New Approach		
	Old design	New design	Improvement
Parts Number	19	17	10.5%
Number of Assembly	23	18	21.7%
Module Number	4	6	-50.0%
Total Score	184	165	10.3%
Overall Efficacy	6	17	28.0%

For the new design, the base and stand are separated due to the elimination of the ground base cover, the location of switch panel is on the stand. After redesign, number of modules is then recalculated using similar algorithm and the results shown that the number of module increased to six and number of standard component increase to three. Overall score for the product has changed due to the reduction of components and changes in joining method. By using this, product efficiency can be calculated. The result of product efficiency before and after redesign is discussed afterwards. The assembly digraph shown in Figure 8 illustrates the redesigning process of the fan. Figure 9 illustrates the joining methods alternatives for guard lock nut mounter changes. Here the snap fit joint is selected due to the easier disassembly factor and strength required for the assembly. Figure 10 shows an old design of the base and the stand and Figure 11 shows the schematic diagram of the new design of both the base and the stand.

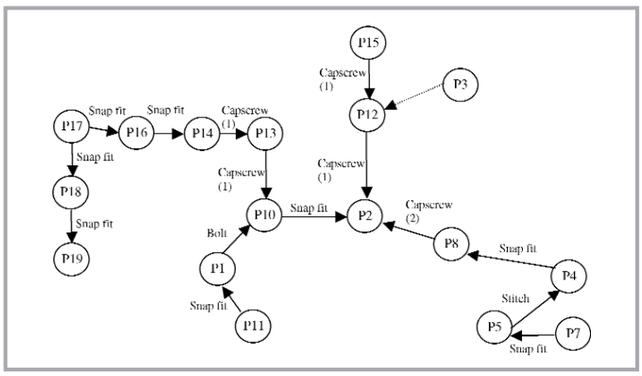

Figure 8: New assembly digraph of the table fan after redesign

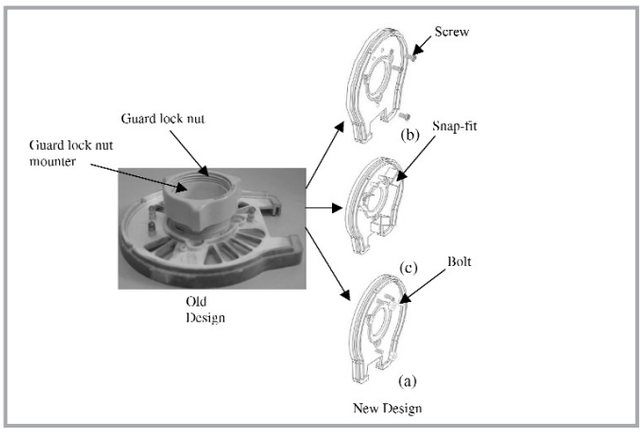

Figure 9: Three possible joining method due to elimination of guard lock nut mounter

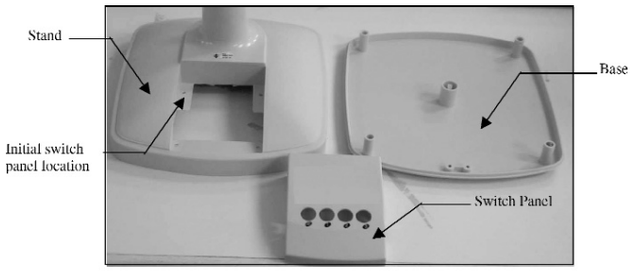

Figure 10: Old design of stand with base and switch panel

To validate the result using this method, a comparison to the published method is carried out, as shown in Table 4, a method that developed by Ehud et al. [15]. The result shows the similar pattern as indicated by proposed approach, where efficiency increase about 50% and the difficulty score reduce more than 33%.

034-040·methodology 9/20/05 12:24 PM Page 40

Table 4: The result of the new table fan design from other approach

Parameter	Ehud et al. Method [3]		
	Old design	New design	Improvement
Number of Parts	19	17	10.5%
Non-required Parts	4	2	50%
Number of Tasks	23	18	21.7%
Value-added Tasks	4	1	75%
Number of Tools	5	3	40%
Number of Tools Changes	13	9	30.8%
Difficulty Score	247	165	33.1%
Efficiency Rating	8.1%	12.1%	49.4%

Finding from this study are compared to the other tools developed by Boothroyd and Dewhurst [2], which emphasis more on the complexity factor of the design assembly to measure the design efficiency. The result is summarised in Table 5.

Table 5: Method by Boothroyd and Dewhurst (1996) for comparison

Other Evaluation Method	Reference	Before Redesign	After Redesign	Improvement
Complexity factor = $\sqrt{N_p + N_t + N_i}$	Boothroyd and Dewhurst, (1996)	8.18	7.42	9.3%

Where;

N_p = Number of parts

N_i = Number of interfaces

N_t = Number of part types

This approach is also applied to other existing consumer products in the market. The result indicates that most of the products initially have quite high design efficiency for example 66% for the flour mixer, 76% for an electric blender and 54.5% for the juice extractor. The reason is that most of the product gives high score due to the fact that more than 70% of the parts are plastic molded components and used snap fit assembly method. It is anticipated that by applying the new approach proposed in this paper, the result could be further improved.

7.0 CONCLUSIONS

The main objective of the methodology is to evaluate design efficiency by taking assembly criteria as a consideration. In this work, seven assembly criteria are presented, and weighted based on their performance reflected to the seven types of mechanical joint considered in this approach. The result from the case study indicates that through redesign with the guide of the modular product design approach, the efficiency of the design can be increased. The result also indicates that through modular approach, complexity of the product can be reduced. In future works, this approach will be used in redesigning more complex products or systems in order to verify the significant and interaction of each parameter in evaluating design efficiency. Besides that a computer based method will be developed for systematic design evaluation.

ACKNOWLEDGEMENT

The authors would like to thank School of Mechanical Engineering, Universiti Sains Malaysia Engineering Campus and Universiti Sains Malaysia for their sponsorship of this work. (AC 073486) ■

REFERENCES

[1] Andreasen, M., Kahler, S., Swift, K. and Lund, T., *Design for Assembly*, 2nd Edition, IFS Publications Ltd., UK and Springer-Verlag, New York, 1988.

[2] Boothroyd, G. and Dewhurst, P., *Product Design for Assembly*, Mc Graw Hill, Inc. New York, 1989.

[3] Lily, H. S. and Flowers, W. C., "Application of a Design for Remanufacture framework to the selection of product life-cycle fastening and joining methods", *Robotic and Computer Integrated Manufacturing*, 15, pp. 179- 190, 1999.

[4] Tsai, C. K., "Disassembly sequence and cost analysis for electromechanical product", *Robotic and Computer Integrated Manufacturing*, Vol. 16, pp. 43-54, 2000.

[5] He, D. W. and Kusiak, A., "Design of Assembly for modular products", *IEEE Transaction on robotics and Automation*, Vol. 13 No. 5, pp. 646-655, 1997.

[6] Lindbeck, J. R., Product Design and Manufacturer, New Jersey: Prentice Hall, Inc., 1995.

[7] Kalpakjian, S., *Manufacturing Engineering and technology*, 3rd Edition, Addison Wesley Publishing Company, New York, 1995.

[8] Kusiak, A., Larson, N. T. and Wang, J., "Reengineering of design and manufacturing processes", *Comp. Ind. Eng*., Vol. 26 No. 3, pp. 521-536, 1994.

[9] Ingle, K., *Reverse Engineering*, Mc Graw Hill, Inc. New York, 1994.

[10] Otto, K. and Wood, K., "Product evolution: a reverse engineering and redesign methodology", *Research in Eng. Design*, Vol. 10 No. 4, pp. 226-243, 1998.

[11] Lefever, D. and Wood, K., "DFA techniques into Reverse Engineering and Redesign", *ASME DTM*, 1996.

[12] Brennan, L., Gupta, S. M. and Taleb, K. N., "Operations Issues in assembly/disassembly environment". *Int. J. Operational and Production Management*, Vol. 14 No. 9, pp. 57-67, 1994.

[13] Gershenson, J. K., Prasad, G. J. and Allamneni, S., "Modular product design: A life cycle view", *Journal of Integrated Design and Process Science*, Vol. 3, No. 4, 1999.

[14] Huang, C. C. and Kusiak, A., "Modularity in design of products and systems", *IEEE Trans. On Systems, Man and Cybernetics-Part A: Systems and Humans*, Vol. 28 No. 1, pp. 66-77, 1998.

[15] Ehud, K., Brent, B. and Antony, P., "Methodology to evaluate ease of disassembly for product recycling", *IIE Transactions*, Vol. 28, Issue 28, pp. 837-845, 1996.

BED LOAD TRANSPORT MODEL FOR FIELD CONDITIONS – USING CHARACTERISTIC DIAMETER APPROACH

Muhammad Ashiq

JSPS Fellow, Department of Urban Management, Faculty of Engineering, Kyoto University, Yoshida, Sakyo-ku, Kyoto 606-8501, Japan. Formerly: Associate Professor, Civil Engineering Dept., University of Engineering and Technology Lahore, Pakistan

ABSTRACT

A deterministic bed load transport model based on mixed-size (non-uniform) bed material (MBB) has been developed using characteristic particle diameter and published laboratory and field data from the North American and European continents (slope ranges from 0.0023 to 0.047 m/m and bed material size, D_{50} from 0.033 to 0.106 m) and excess discharge theory. Before developing the model performance of the existing bed load transport models was tested and was generally found to be poor, though discharge based models performed relatively better. In this model fitted values of the relationship exponent (β) were used instead of considering a fixed value, as in the existing models. Performance of the model was found satisfactory when tested with the field data and compared with another existing model. Subsequently, the model has been extended through the involvement of an active bed width function for non-uniform cross-sectional flow depth (single channel) rivers and for the braided rivers.

Keywords : *Characteristic Diameter, Excess Discharge Theory, Deterministic Model, MBB Model*

INTRODUCTION

The transport of bed load in mountain rivers with gravel, cobble and boulder bed material formations is difficult/complex to deal with, not only because of the sites' remoteness, large slopes, and lack of gauging stations but primarily due to the non-uniform and unpredictable flow conditions, non-uniformity of bed material formations and the interdependence of various parameters. The complexity of bed load transport phenomenon, in coarse bed material rivers compared with sand bed rivers, is due to their typical features like wider size distribution of bed material and bed load, movement of bed load (generally) for a short period of time (i.e. during high flows), less susceptibility to aggradation and degradation, slow response to modest changes in discharge and discharge duration, and presence of riffle/pool or step/pool type bed formations.

In order to relate different parameters of the bed load transport process, relationships between sediment, fluid, flow, and channel parameters are developed and are usually named sediment transport models/functions/equations. For bed load initiation and transport rate computation in fluvial streams such models have been developed, generally, using four basic theories of 1) discharge [22], 2) shear stress [10], 3) stream power [6], and 4) velocity [9], in conjunction with different calculation approaches (i.e. empirical, semi-empirical, probabilistic, deterministic and dimensional analysis). However, the existing sediment transport models for the mountain rivers are not accurate/efficient and reliable enough as investigators originally thought them to be.

As a large variety of characteristic size based bed load transport models exist a question arises why is it necessary to develop another model using the same approach. It has been developed because: a) computed results from different existing models often differ drastically from each other and from measurements; b) some of the models' results are contradictory partly because the ranges of measured data upon which these models are based were limited; c) they have been developed mostly using data collected under laboratory conditions (commonly with uni-size bed materials) while they are being applied to the field conditions (with mixed-size bed materials); d) models have been developed (mostly) using shear stress and stream power theories, which are less practical compared with the discharge theory (as proved by the recent studies); e) existing discharge theory based models, which are few in number, have been developed assuming a value of the relationship exponent, β taken as 1 in the Schoklitsch [22] model, and 2 in the Milhous [18] model, rather than using the fitted exponent values; and f) some of the models have been developed without (directly) involving the bed material relative size effects. Owing to these deficiencies/flaws with the existing bed load transport models it was required to develop a model for the field conditions.

To meet this requirement uni-size bed material data from the flume studies (i.e. CSU, Colorado State University; EPFL, Ecole Polytechnique Fédérale de Lausanne; and ETHZ, Eidgenossische Technische Hochschule Zürich) have been used to develop a philosophy and basis for the model development for the field conditions (i.e. for mixed size bed materials). For this purpose, first of all various individual empirical models (defining the relationship between the unit bed load discharge, qs and water discharge parameter, q-qc) have been developed. These use different slopes (S) and grain sizes (D_{50}), and assume four different cases for the relationship exponent β (β = fitted values; β = 1; β = 1.5; and β = 2). These

041-052·bed Load 9/20/05 12:29 PM Page 42

are then transformed into four models (i.e. one for each β value) by using an appropriate statistical technique. The performance of these four models has been tested with the data from the River Severn, Wales (UK) and North Fork of South Platte River at Buffalo, Colorado (USA) and with the computed results of the Milhous [18] model. On the basis of their performance a model (with β = fitted values) has been selected as a base for model development for the mixed-size bed material (field conditions). Using this base and mixed-size (non uniform) bed material data from different rivers/streams studies (i.e. Elbow, Oak, Aare, Little South Fork-stations C-F, Gaula, Roaring - two sites, and Pitzbach) a deterministic model has been developed for the field conditions. Subsequently the performance of this model has been tested with the observed data of the River Severn and North Fork of South Platte River and with the Milhous [18] model results and has been found to be satisfactory. Later on, the developed model has been extended for the non-uniform cross-sectional flow rivers (single channel) through the incorporation of the active bed width function (for determining active bed width parameter, which plays important role in the transport of bed load when channel cross-section is non-uniform). The developed model has also been extended for the braided rivers with multiple channels.

However, before developing the model the performance of four existing (characteristic size based) models, belonging to different theories/approaches, has been tested.

PERFORMANCE TEST OF EXISTING (CHARACTERISTIC SIZE BASED) BED LOAD TRANSPORT MODELS

For the purpose of performance testing, the following models were selected, representative of different approaches.

1- Milhous [18] model, excess discharge based;
2- Meyer-Peter and Mueller [17] model, excess shear stress based;
3- Bagnold [6] model, excess stream power based; and
4- Parker et al. [21] model, based on concept of equal mobility and similarity approach.

Their performance was tested with the observed data of the Middle Fork of Boulder Creek at Netherland (Colorado) and Williams Fork near Leal (Colorado). These streams were selected for testing because their slopes (S) and bed material sizes (D_{50}) covered the range commonly available in coarse bed material streams (i.e. S = 0.5 - 1.7 % and D50 = 27 - 67 mm). Performance test results of these models (depicted in Figure 1) in comparison with the observed data of Middle Fork of Boulder Creek show that the Milhous [18] model performed better as the data points are scattered close to the line of perfect agreement (LPA). The Parker et al. [21] model performed worse since the data points generated by this model are located at the farthest distance from the LPA. Similarly, test of these models with the Williams Fork data, depicted in Figure 2, show that the performance of the Milhous model was relatively better, while the Meyer-Peter and Mueller model's performance was the worst. Its worst performance in this study confirmed the results of Yang [29] when he ranked the model at the bottom end. Likewise USGS [25] ranked this model at number three, during a performance test of five bed load transport models. This poor performance of the Meyer-Peter and Mueller model may be due to the reason that sediment size used in the model development was finer (ranged from 0.4 mm to 28.65 mm) than the streams' sediment sizes with which it was tested. For the Williams Fork, the performance of the Parker et al. [21] model was relatively better as data points were situated relatively closer to the LPA, which is different from its performance for the Middle Fork of the Boulder Creek. The Parker et al. model may have performed poorly partly because it is based on subsurface material and the concept of equal mobility and the value of τ^*_{ri} (= 0.0876) parameter in the model is site specific. This showed the inconsistency of performance of the existing models'. These inconsistent results are similar to those obtained by Gomez and Church [12] when they stated that "no formula performs consistently well". The poor performance of the Bagnold model confirmed the findings of Carson and Griffiths [8] study, according to which this model needs extensive calibration. From these two tests, with the Middle Fork and Williams Fork, a better performance

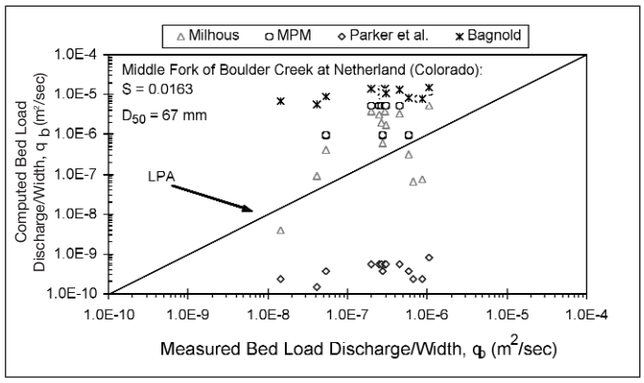

Figure 1: Comparison of measured bed load discharges of the Middle Fork of Boulder Creek at Netherland (Colorado) to the computed loads by four bed load transport models

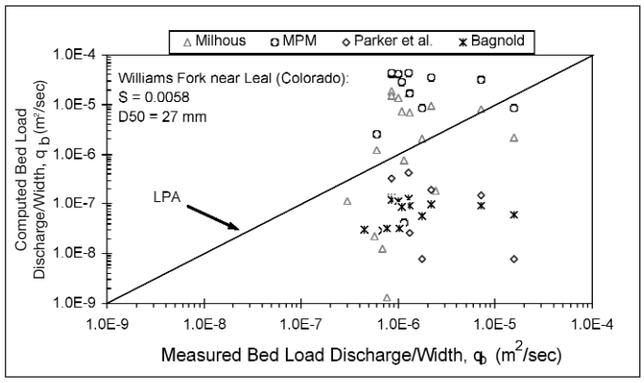

Figure 2: Comparison of measured bed load discharges of the Williams Fork near Leal (Colorado) to the computed loads by four bed load transport models

of the Milhous [18] model is evident, although it is not good. These results, in general, are in agreement with the results of the recent studies carried out by Bathurst et al. [7], USGS [25], Milhous [18] and Inpasihardjo [15] who found that the

041-052·bed Load 9/20/05 12:29 PM Page 43

performance of excess discharge theory based models is better than the other theories (i.e. shear stress and stream power) based models. The Milhous model performed better partly because the data used in the development of it generally covers the sediment size range available in the coarse bed material rivers.

MODEL DEVELOPMENT FOR BED LOAD TRANSPORT (FOR FIELD CONDITIONS)

Basis for Model Development

From the results of different recent studies as mentioned above and the results of this study the inconsistent and poor performance of the existing characteristic size based bed load transport models, in general, is evident. The excess discharge theory based models performed (relatively) better but even so their performance was not satisfactory. It is, therefore necessary to develop this theory further using a sufficiently large data base, so that optimum results may be obtained. For this purpose the following deterministic model, based on excess discharge theory, is proposed.

$$q_s = \alpha\,(q - q_c)^{\beta} \qquad (1)$$

where

q_s = bed load discharge/width (m^2/sec); α = coefficient; q = water discharge/width (m^2/sec); q_c = critical water discharge/width (m^2/sec).

So far as methodology is concerned values of α and β will first be determined by using the uni-size bed material data for each case and then it will be checked how α and β vary. After examining their variations a model for field conditions has been developed, using mixed-size (non-uniform) bed material data.

Developing Individual Empirical Models to Examine the Basic Relationships Using Uni-Size Bed Material Data and to Quantify Equation (1)

In the development of these models (from the flume data) critical discharges were required which were determined for each set of values (i.e. with one D_{50} value and different slopes, S) which are given in Table 1. The method of "back extrapolation" (in which a line is fitted to data and its coefficient with the x-axis is noted) followed for determining critical discharges (q_c) is illustrated in Figure 3; however, only three values of critical discharges are shown in this figure for demonstration purpose i.e. one case for each of the CSU, EPFL, and ETHZ studies having 4, 6, and 8 data points, respectively. Since in the figure there are not many data points, therefore in order to show the likely errors, standard error bars (i.e. both X and Y error bars, positive and negative) have been plotted. However, one thing should be remembered that the critical discharge values determined here by (regression) fitted lines can be and are usually determined by eye fitted lines (e.g. as done by Bathurst et al. [7] and Inpasihardjo [15]), therefore use of this regression is not important at all - that is why the

Table 1: Critical discharges for the uni-size bed material data (i.e. CSU, EPFL, and ETHZ studies data) and other relevant parameters

Study (1)	No of Data Points (2)	Bed Material Size (D_{50}) (m) (3)	Slope (S) (m/m) (4)	Critical Discharge (q_c) (m^2/sec) (5)
CSU	4	0.0088	0.02	0.051
	6	0.0088	0.05	0.010
	6	0.0088	0.08	0.0095
	6	0.034	0.08	0.046
EPFL	3	0.0222	0.01	0.265
	6	0.0222	0.03	0.105
	7	0.0222	0.05	0.065
	8	0.0222	0.07	0.035
	6	0.0222	0.09	0.025
	4	0.0443	0.03	0.225
	6	0.0443	0.05	0.127
	4	0.0443	0.07	0.092
	6	0.0443	0.09	0.072
	6	0.0115	0.005	0.171
	4	0.0115	0.0075	0.133
	4	0.0115	0.01	0.114
ETHZ	4	0.02865	0.0107	0.520
	8	0.0033	0.0027	0.105

041-052·bed Load 9/20/05 12:29 PM Page 44

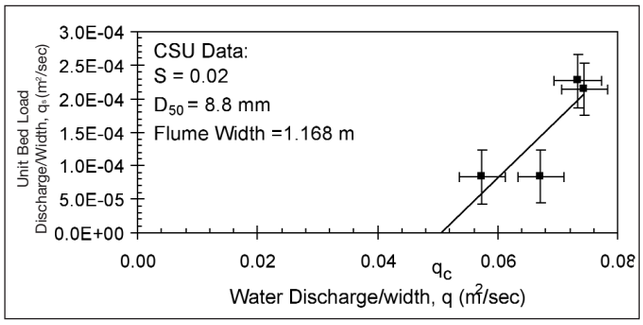

(a)

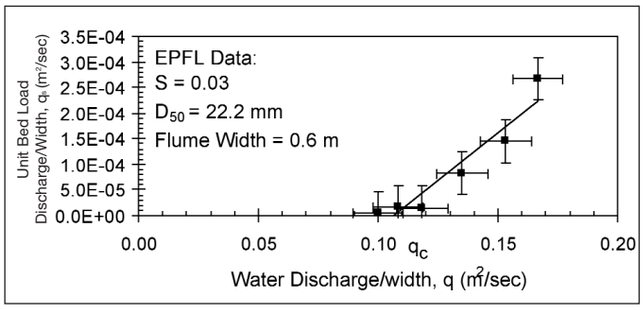

(b)

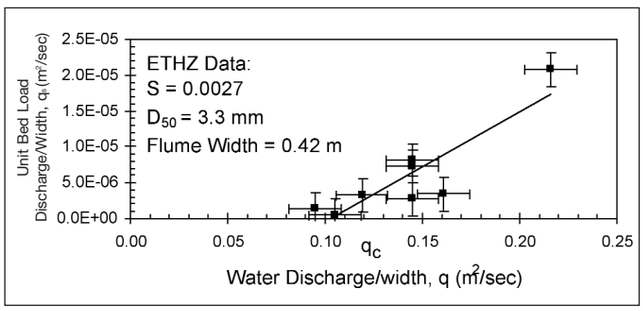

(c)

Figure 3: Critical discharge determination for uni-size bed materials; a) CSU data, b) EPFL data, and c) ETHZ data

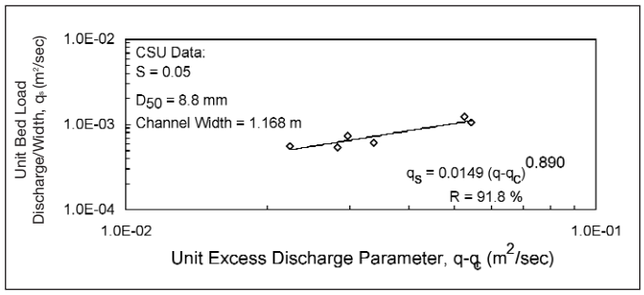

(a)

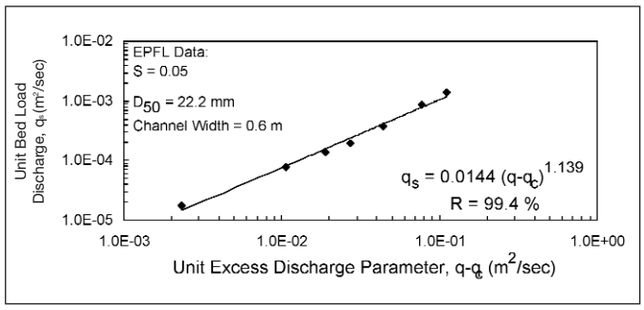

(b)

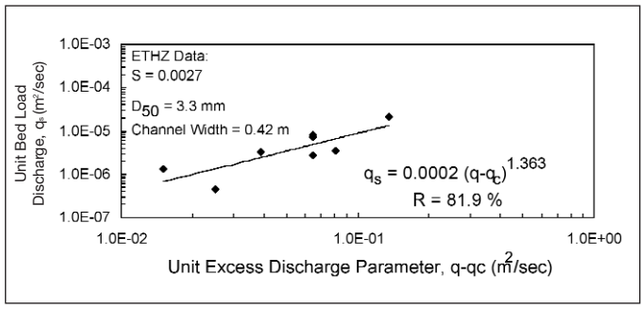

(c)

Figure 4: Individual empirical models for bed load discharge for uni-size bed materials; a) CSU data, b) EPFL data, and c) ETHZ data

correlation coefficient, confidence limit and other regression techniques are not investigated here. By using these critical discharges (given in Table 1) empirical models quantifying Equation (1) for each D50 data set (and respective slope) were developed which are given in Table 2. In the development of these models three data sets of CSU, EFPL and ETHZ were used. The statistical technique used was the Power Model as it was found best among all the six techniques (i.e. Linear, Power, Polynomial, Logarithmic, Exponential, Through Origin) that were tested. These models consist of 4 based on CSU data, 12 based on the EPFL data; and 2 based on ETHZ data (for detail see Table 2). Figure 4 illustrates the development of these models, taking one case for each flume, along with their respective correlation coefficient (R) values. These individual models were developed considering four different cases (conditions), which are:

1. first case: models were developed without any condition i.e. with the fitted exponent (β) and coefficient (α) and are given in column 6 of Table 2;
2. second case: comprises development of models when β was fixed equal to 1 and α was adjusted to the best fit under this constraint. These models are presented in column 7 of Table 2;
3. third case: in the development of these models β was fixed equal to 1.5 and α was adjusted to the best fit under this constraint. The models developed in this case are given in column 8 of Table 2; and
4. fourth and final case: includes models in which β was fixed equal to 2 and α was adjusted to the best fit under this constraint. Models developed for this case are given in column 9 of Table 2.

The reason for β =1, β =1.5, β = 2 (in the latter three cases) is that this is typical of the range in other models (i.e. existing models).

Transformation of Individual Models to Four Deterministic Models to Develop Basis for Model Development for Field Conditions.

After developing the individual empirical models (given in Table 2) there were different ways to combine them in one deterministic model that could be representative for all. One well known approach was the similarity approach but it involves graphical work which may introduce more error, as too many fitted lines have to collapse in this approach. Another

Table 2: Uni-size bed-material based sediment transport models (empirical) along with bed-material sizes and slopes for different flume studies including CSU, EPFL, and ETHZ studies

Data Set	No Of Data Points	Bed Material Size D_{50} (m)	Channel Width (W) (m)	Slope (S) (m/m)	Bed Load Discharge Empirical Models			
					with fitted slope and coefficient Case - 1	with constant slope of 1 and changing coefficient Case - 2	with constant slope of 1.5 and changing coefficient Case - 3	with constant slope of 2 and changing coefficient Case - 4
(1)	(2)	(3)	(4)	(5)	(6)	(7)	(8)	(9)
CSU								
	4	0.0088	1.168	0.02	$qs = 0.086 * (q-qc)^{0.284}$	$qs = 0.011* (q-qc)^{1}$	$qs = 0.004* (q-qc)^{1.5}$	$qs = 0.001* (q-qc)^{2}$
	6	0.0088	1.168	0.05	$qs = 0.0149 * (q-qc)^{0.890}$	$qs = 0.013* (q-qc)^{1}$	$qs = 0.003* (q-qc)^{1.5}$	$qs = 0.0005* (q-qc)^{2}$
	6	0.0088	1.168	0.08	$qs = 0.057 * (q-qc)^{1.001}$	$qs = 0.061* (q-qc)^{1}$	$qs = 0.011* (q-qc)^{1.5}$	$qs = 0.002* (q-qc)^{2}$
	6	0.034	1.168	0.08	$qs = 0.095 * (q-qc)^{0.842}$	$qs = 0.070* (q-qc)^{1}$	$qs = 0.026* (q-qc)^{1.5}$	$qs = 0.095* (q-qc)^{2}$
EPFL								
1	6	0.0222	0.6	0.01	$qs = 1.632E-05 * (q-qc)^{1.797}$	$qs = 0.0005* (q-qc)^{1}$	$qs = 0.00004* (q-qc)^{1.5}$	$qs = 0.000003* (q-qc)^{2}$
	3	0.0222	0.6	0.03	$qs = 8.532E-05 * (q-qc)^{1.808}$	$qs = 0.001* (q-qc)^{1}$	$qs = 0.0002* (q-qc)^{1.5}$	$qs = 0.00002* (q-qc)^{2}$
	7	0.0222	0.6	0.05	$qs = 0.0144 * (q-qc)^{1.139}$	$qs = 0.008* (q-qc)^{1}$	$qs = 0.001* (q-qc)^{1.5}$	$qs = 0.0002* (q-qc)^{2}$
	8	0.0222	0.6	0.07	$qs = 0.007 * (q-qc)^{1.297}$	$qs = 0.016* (q-qc)^{1}$	$qs = 0.0021* (q-qc)^{1.5}$	$qs = 0.0003* (q-qc)^{2}$
	6	0.0222	0.6	0.09	$qs = 0.045* (q-qc)^{0.932}$	$qs = 0.028* (q-qc)^{1}$	$qs = 0.004* (q-qc)^{1.5}$	$qs = 0.0006* (q-qc)^{2}$
2	4	0.0443	0.6	0.03	$qs = 4.859E-07 * (q-qc)^{2.625}$	$qs = 0.0004* (q-qc)^{1}$	$qs = 0.00004* (q-qc)^{1.5}$	$qs = 0.000004* (q-qc)^{2}$
	6	0.0443	0.6	0.05	$qs = 5.512E-08 * (q-qc)^{3.343}$	$qs = 0.002* (q-qc)^{1}$	$qs = 0.0001* (q-qc)^{1.5}$	$qs = 0.00001* (q-qc)^{2}$
	4	0.0443	0.6	0.07	$qs = 0.0004 * (q-qc)^{1.796}$	$qs = 0.007* (q-qc)^{1}$	$qs = 0.0007* (q-qc)^{1.5}$	$qs = 0.00008* (q-qc)^{2}$
	6	0.0443	0.6	0.09	$qs = 0.003 * (q-qc)^{1.517}$	$qs = 0.016* (q-qc)^{1}$	$qs = 0.0018 * (q-qc)^{1.5}$	$qs = 0.0002 * (q-qc)^{2}$
3	6	0.0115	0.6	0.005	$qs = 4.801E-05 * (q-qc)^{1.429}$	$qs = 0.0005* (q-qc)^{1}$	$qs = 0.00008 * (q-qc)^{1.5}$	$qs = 0.000015 * (q-qc)^{2}$
	4	0.0115	0.6	0.0075	$qs = 1.181E-04 * (q-qc)^{1.273}$	$qs = 0.0006* (q-qc)^{1}$	$qs = 0.0001* (q-qc)^{1.5}$	$qs = 0.00002* (q-qc)^{2}$
	4	0.0115	0.6	0.01	$qs = 1.577E-05 * (q-qc)^{1.801}$	$qs = 0.0009* (q-qc)^{1}$	$qs = 0.00014* (q-qc)^{1.5}$	$qs = 0.00002* (q-qc)^{2}$
ETHZ								
1	4	0.02865	2	0.0107	$qs = 0.0005 * (q-qc)^{1.462}$	qs = 8.2*10-8* $(q-qc)^{1}$	qs = 1.7*10-12* $(q-qc)^{1.5}$	qs = 5*10-17* $(q-qc)^{2}$
2	8	0.0033	0.42	0.0027	$qs = 0.0002 * (q-qc)^{1.363}$	qs = 8.5*10-8* $(q-qc)^{1}$	qs = 3*10-11* $(q-qc)^{1.5}$	qs = 4*10-14* $(q-qc)^{2}$

NB: With a few exceptions the values of correlation coefficient (R) for all these models were greater than 85%.
q, qc and qs are unit water discharge, critical water discharge and bed load discharge (m3/sec/m), respectively.

041-052·bed Load 9/20/05 12:29 PM Page 46

approach was to develop a representative empirical model for each data set (i.e. one for each CSU, EPFL and ETHZ) and then plot α and β versus slope (S, average value) and particle size (D_{50} , average value) - two variables that play important role in the transport of bed load. This approach (partly statistical and graphical) was tried up to the very last stage but due to the insufficient data points for slopes and particle sizes it was rejected. Finally, a decision was taken to combine the individual models (in terms of α and β) through multi-variate analysis (a statistical technique in which a response variable is related to more than one predictor variables - using the statistical package of MINITAB).

A combined representative function (dimensionless) for the exponent, β (= f [S, D_{50}/W]) was obtained with a reasonable value of correlation coefficient, R (i.e. 77.3%). Nonetheless, the combined representative function for the coefficient, α (= f[S, D_{50}/W]) gave a poor value of correlation coefficient. Therefore for combining coefficients, α (= f[S]) a power model approach was used which provided a high value of the correlation coefficient. On the other hand the relationship between β values and slopes (S) was also explored and was found very poor. The representative functions for α and β for the above mentioned four cases are

Case - I

β = fitted values

Combining β (individual) values for one function (R = 77.3 %)

$$\beta = 1.02 - 7.16S + 22.5\frac{D_{50}}{W} \qquad (2)$$

Combining α (individual) values for one function (R = 50 %)

$$\alpha = 0.113 * S^{1.490} \qquad (3)$$

Case - II

β = 1 (R = 84 %)

$$\alpha = 9.85 * S^{2.375} \qquad (4)$$

Case - III

β = 1.5 (R = 77 %)

$$\alpha = 12.698 * S^{3.125} \qquad (5)$$

Case - IV

β = 2 (R = 74 %)

$$\alpha = 10.34 * S^{3.711} \qquad (6)$$

where

S = slope and ranged between 0.003 and 0.09 (m/m); D_{50} = characteristic size of the bed surface material (m) and ranged between 0.003 m and 0.045 m; and W = channel width (m) ranging between 0.6 and 2 m. In Equation (3) though there is not a strong relationship between α and S (slope), however, it should be remembered that the performance of Equation (1) (subsequently converted into Equations (7) to (10) depends not only upon the α parameter (function of S) but also upon the combined effect of the α and β parameters. This is best in the case of Equation (7), as proved by the performance test. On the other hand Equations (4) to (6) have good relationships also.

By substituting the values of α and β into Equation (1) the bed load discharge deterministic models for all the four cases can be obtained and are

when β = fitted values

$$q_s = 0.113 * S^{1.490}(q - q_c)^{1.02 - 7.16S + 22.5\frac{D_{50}}{W}} \qquad (7)$$

when β = 1

$$q_s = 9.82 * S^{2.375}(q - q_c) \qquad (8)$$

when β = 1.5

$$q_s = 12.698 * S^{3.125}(q - q_c)^{15} \qquad (9)$$

when β = 2

$$q_s = 10.34 * S^{3.711}(q - q_c)^{2} \qquad (10)$$

The above mentioned models (Equations (7) to (10) are based on the assumption that sediment is moving over the whole flow width of the channel cross-section (i.e. surface flow width = active bed width). The values of α and β vary significantly between data sets (and the data are anyway limited). The attempt to fit single α and β relationships is therefore in the context of a study, to investigate possible links between flow rate and sediment discharge.

Model Performance

To check the performance of the developed models (Equations (7) to (10)) they were applied to the River Severn and North Fork of South Platte River at Buffalo (Colorado) data to compute bed load discharges. These two streams were particularly selected for the test because their bed material sizes (D_{50}) were almost in the same range as that of the materials used in the flume studies, whose data were used in the development of the models. The computed bed load discharges by the developed models were plotted against the observed bed load discharges from the rivers and results are depicted in Figures 5 and 6, respectively. As evident from

041-052·bed Load 9/20/05 12:29 PM Page 47

Figure 5 (for River Severn) data points by Equation (7) (i.e. β = fitted values) are mostly located either on or in the close proximity of the line of perfect agreement (LPA), whereas data points generated by Equations (8) to (10) are located below the LPA which shows underestimation of computed loads by these models, nevertheless, among these models (Equations (8) to (10) results of Equation (8) (β=1) were better.

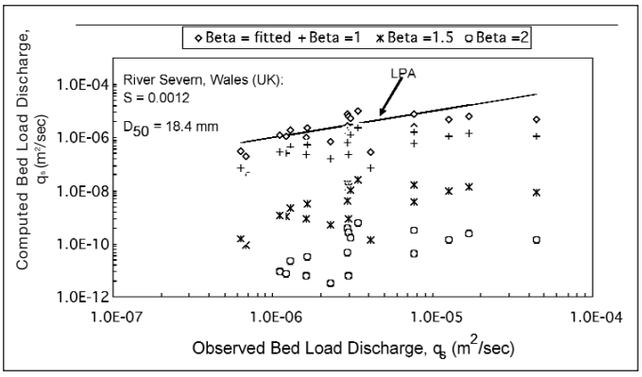

Figure 5: Comparison of bed load discharges computed by the four deterministic, uni-size based, models (Equations 7-10) with the observed loads of River Severn (UK)

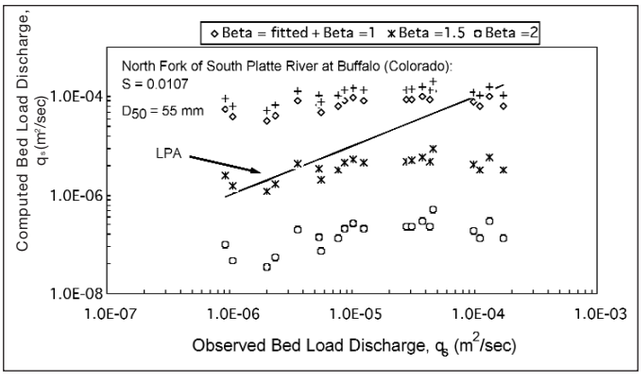

Figure 6: Comparison of bed load discharges computed by the four deterministic, uni-size based, models (Equations 7-10) with the observed loads of North Fork of South Platte River at Buffalo, Colorado (USA)

On the other hand, for the North Fork of South Platte River, Equation (7) performed better at the higher observed load discharges, compared with the lower discharges when it overestimated the computed loads. The performance of this equation was somewhat similar to Equation (8). However, Equation (8) overestimated the computed loads. Equation (9) (β = 1.5) performed better at the lower discharges but it underestimated the computed loads at the higher discharges. In other words it can be said that performance of Equation 7 improved with the increase in load discharges while performance of Equation 9 got worse with the increase in discharge, especially at the higher discharges. Thus, based upon these results, for River Severn and North Fork of South Platte River, it is not difficult to rank performance of the models in the following descending order:

Equation (7), with β = fitted values
Equation (8), with β =1
Equation (9), with β =1.5; and
Equation (10), with β = 2.

Since, the model with the fitted values of β (Equation (7)) performed better than the other models, it will be used as the basis for developing a (forthcoming) mixed-size bed-material model for the field conditions.

DEVELOPMENT OF MIXED-SIZE (NON UNIFORM) BED-MATERIAL BASED MODEL (MBB MODEL) FOR FIELD CONDITIONS

Development of Individual Models

Based on the uni-size bed material model's philosophy for development of these models only the fitted value case was followed. For developing the individual empirical bed load discharge models for different rivers the values of critical discharge were required for these rivers which were determined by back extrapolation of q_s/q and are given in Table 3. Then by using the same approach as used in the case of the uni-size bed-material based empirical models various empirical models were developed for the Elbow River, Oak Creek, Aare River, Little South Fork (Station C-F), River Gaula, Roaring River (two sites) and Pitzbach site. In the case of the Elbow and Gaula rivers two models for each river were developed, one for the surface flow width and other for the active bed width data. For demonstration purpose a surface flow width based model for the Elbow River is presented in Figure 7. Similarly, two models were developed for the Little South Fork Station-C since it has two values of critical discharge, qc as the data were into two separate groups (i.e. non linear variation). So far as all the other rivers are concerned only one model was developed for each river. The developed models for each river site are presented in column 6 of Table 4.

Generating a Single Deterministic Model

The individual empirical models given in Table 4 were combined (except active bed width based models) in terms of single α and β functions by using the multi-variate analysis approach (a statistical approach with which a response variable can be related to more than one predictor variables). The reasons why to use this approach have been explained under an earlier article "Transformation of Individual Models to…..". The statistical analysis package used for the multi-variate analysis was MINITAB. This approach was opted for both α and β as it provided higher correlation coefficient (R) values of 86% and 85% respectively, unlike the uni-size bed-material when it worked well only for the β function. The developed functions for α and β are

$$\alpha = Exp\left[-11.8 - 36.3S + 131\,\frac{D_{50}}{W}\right] \qquad (11)$$

041-052·bed Load 9/20/05 12:29 PM Page 48

Table 3: Critical discharges for the field studies data (i.e. for rivers) along with other relevant parameters

Study (1)	No. of Data Points (2)	Bed Material Size (D_{50}) (m) (3)	Slope (S) (m/m) (4)	Critical Discharge (q_c) (m^2/sec) (5)
Elbow River	23	0.076	0.00745	0.95
Oak Creek	12	0.054	0.01	0.29
Aare River	34	0.070	0.0023	3.20
Little South Fork Station - C	23	0.033	0.02	0.04
				0.24
Station - D	20	0.042	0.014	0.46
Station - E	22	0.042	0.0105	0.34
Station - F	12	0.038	0.015	0.295
River Gaula	52	0.080	0.0024	4.4
Roaring River a) Alluvial Fan Road Bridge Site (1985).	30	0.077	0.047	0.142
b) Ypsilon Lake Trail Bridge Site (1985).	22	0.106	0.037	0.163
Pitzbach (1991)	33	0.098	0.0395	0.138

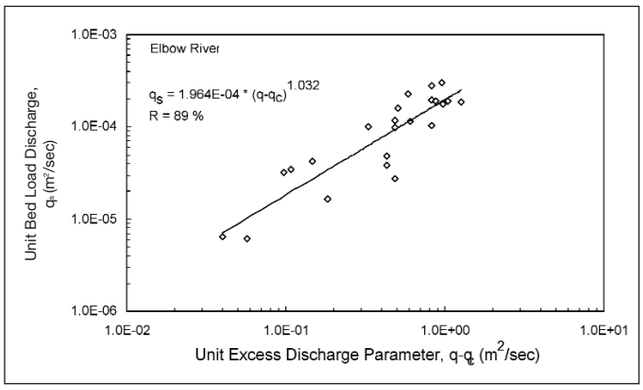

Figure 7: Individual empirical model development (for bed load discharge) for the Elbow River (Canada), using surface flow width of the channel

$$\beta = 1.01 - 14.5S + 51.2\,\frac{D_{50}}{W} \qquad (12)$$

where

S = slope, ranged between 0.2% and 5%; D_{50} = median size of the bed surface material (m) and ranged between 0.033 m and 0.106 m; and W = channel width, ranging between 6 and 120 m.

By substituting the values of α and β functions from Equations (11) and (12) into Equation (1) the generated deterministic model (i.e. MBB model) is

$$q_S = Exp\left[-11.8 - 36.3S + 131\,\frac{D_{50}}{W}\right] * \left\{q - q_C\right\}^{1.01-14.5S+51.2\,\frac{D_{50}}{W}} \qquad (13)$$

Performance Test of MBB Model

The relative performance of the developed model (Equation (13)) was investigated. First, unit bed load discharges were computed by using the model and data from the River Severn and North Fork of South Platte River. Then these computed loads were compared with the observed loads of the River Severn and North Fork and with the loads computed by the Milhous [18] model, a model that performed best in the performance test. The loads computed by the MBB and Milhous models were plotted against the observed loads recorded from both of the streams which are depicted in Figures 8 and 9. Figure 8 shows that sediment loads computed by the MBB model are situated close to the line of perfect agreement (LPA) for River Severn compared with the Milhous [18] model. Nevertheless, a trend of overestimation is dominant that is in-contrast to the Milhous model results that underestimate the loads, especially at lower flows. Therefore, it can be said that the overall performance of the model (i.e. MBB model) was better than that of the Milhous model. For the North Fork, data points generated by the model (MBB model) are almost horizontal and the model is therefore not very sensitive to whatever the change is which causes the measured data to vary. Nonetheless, these data points are mostly scattered close to the LPA, though at higher flows some data points are located lower than the LPA, indicating underestimation of loads at the higher flow rates. On the other hand the Milhous model overestimates the sediment loads at lower flows, as the data points lie above the LPA, and underestimated the

041-052·bed Load 9/20/05 12:29 PM Page 49

Table 4: Mixed-size bed-material based bed load transport models along with bed-material sizes and slopes for different rivers

Site (1)	No. of Data Points (2)	Bed Material D_{50} (m) (3)	Channel Width (m) (4)	Slope S (m/m) (5)	Bed Load Discharge Models (6)
Elbow River	23	0.076	43	0.00745	$q_s = 1.964E\text{-}04 * (q-q_c)^{1.032}$ (surface width based) $q_s = 2.367E\text{-}05 * (q-q_c)^{1.609}$ (active width based)
Oak Creek	12	0.054	3.66	0.01	$q_s = 4.868E\text{-}05 * (q-q_c)^{1.709}$
Aare River	34	0.070	14.8	0.0023	$q_s = 4.6271E\text{-}05 * (q-q_c)^{1.5}$
Little South Fork Station -C	23	0.033	6.54	0.02	$q_s = 1.607E\text{-}06 * (q-q_c)^{0.84}$ (using lower limit of q_c) $q_s = 5.915E\text{-}06 * (q-q_c)^{0.94}$ (using upper limit of q_c)
Station - D	20	0.042	12.64	0.014	$q_s = 1.831E\text{-}06 *(q-q_c)^{0.744}$
Station - E	22	0.042	11.34	0.0105	$q_s = 2.92E\text{-}06 * (q-q_c)^{1.39}$
Station - F	12	0.038	15.8	0.015	$q_s = 7.127E\text{-}06* (q-q_c)^{0.946}$
River Gaula	52	0.080	119.93	0.0024	$q_s = 1.491E\text{-}06* (q-q_c)^{0.663}$ (surface width based) $q_s = 8.580E\text{-}09 * (q-q_c)^{3.79}$ (active width based)
Roaring River a) Alluvial Bridge Site	30	0.077	6.1	0.047	$q_s = 5.165E\text{-}05* (q-q_c)^{1.403}$
b)- Ypsilon Lake Trial Bridge Site	22	0.106	6.25	0.037	$q_s = 6.553E\text{-}06* (q-q_c)^{1.006}$
Pitzbach	33	0.098	8	0.0395	$q_s = 4.23E\text{-}06* (q-q_c)^{0.883}$

NB: With a few exceptions the values of the correlation coefficient (R) for all these models were greater than 85%.
q, q_c and q_s are unit water discharge, critical water discharge and bed load discharge (m^3/sec/m), respectively.

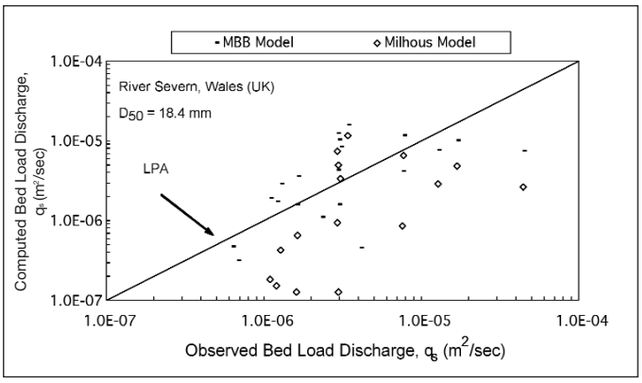

Figure 8: Comparison of observed and computed bed load sediment discharges by MBB and Milhous Models for the River Severn, Wales (UK)

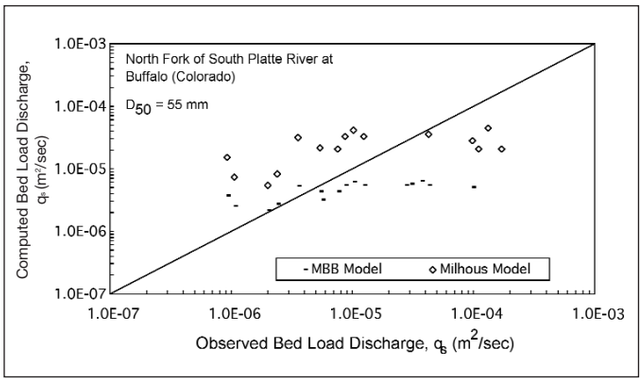

Figure 9: Comparison of observed and computed bed load sediment discharges by MBB and Milhous Models for North Fork of South Platte River, Colorado (USA)

041-052·bed Load 9/20/05 12:29 PM Page 50

loads at the higher flow rates. Generally, a trend of overestimation was found for this model, which is opposite to the MBB model results. Thus from both of the analyses (i.e. for River Severn and North Fork) a better performance of the developed model (i.e. MBB) is evident. However, while applying this model the critical discharge (qc) value should be determined carefully as a minor error in it could affect the computed loads considerably. The Milhous model's unsatisfactory performance for the North Fork stream is contrary to its performance for the Middle Fork and Williams Fork, which could be due to variation among the channel characteristics (i.e. D50 and S etc.). This varying performance of the Milhous model for different streams is in accordance with the study results obtained by Ashiq et al. [2] and Gomez and Church [12] who found that no formula (model) perform consistently well under varying field conditions. During these performance tests it has been found that the bed material size and slope were the two significant parameters that affected the models' performance.

MBB MODEL EXTENSION FOR NON UNIFORM CROSS-SECTIONAL CHANNELS

If a river channel cross-section is non uniform then transport of bed load does not take place uniformly across the width i.e. only some part (or parts) of the flow width (i.e. active bed width) acts as a sediment transport carrier while remaining part (or parts) acts just as a flow passage. For such rivers bed load transport computation by using surface flow width will lead to overestimation of the loads. To compute true amount of bed load discharge passing in a river it is therefore necessary to know how much width of the channel is active or transporting bed load (i.e. active bed width), which can be computed by Equation (1) developed by Ashiq [3].

$$Log\left(\frac{W_A}{W}\right) = -0.173\ (1 + 0.54\ q) \qquad (14)$$

where

q = unit water discharge (m^3/sec/m); W_A = Active bed width (m); and W = surface flow width (m).

The computed active bed width parameter, W_A than be used to replace the surface width parameter, W in the MBB model (Equation (13)) which then may be used to compute bed load discharge for rivers with non uniform cross-sectional flow depth channels (i.e. surface flow width ≠ active bed width). While using Equation (14) one should bear in mind that there is spurious correlation, as W is involved in both q (i.e. Q/W) and Wa/W parameters. The effect of the spurious correlation has not been investigated here. Details regarding spurious correlation may be seen in statistics books written by Hald [14] and Aitchison [1].

MBB MODEL EXTENSION FOR BRAIDED RIVERS

The model developed earlier for the field conditions for the uniform cross-sectional rivers (Equations (13)) and its application to non-uniform cross-sectional flow depth rivers in conjunction with Equation (14) is useful only when rivers have single channel. If the river is braided (i.e. water flows in multiple channels) then it is necessary to apply Equations (13) and (14) to each individual channel, according to the prevailing condition and then sum up all the loads. Thus the model for the braided rivers would be

$$Q_b = \sum_{i=1}^{n} W_i q_{si} + \sum_{j=1}^{n} W_{A\,J} q_{s\,(A)\,j} \qquad (15)$$

where

Q_b = total bed load discharge in a braided river (m^3/sec); W_i = water surface flow width for channel i (m); q_{si} = unit bed load discharge (m^3/sec/m) for channel i for which whole channel flow width acts as sediment carrier (surface flow width = active bed width) and can be computed by Equation (13); W_{Aj} = active bed width of channel j; and $q_{s(A)j}$ = unit bed load discharge (m^3/sec/m) for channel j (surface flow width ≠ active bed width) and can be computed by Equation 13 in conjunction with Equation 14.

RESULTS AND DISCUSSION

The performances of four existing bed load transport models (characteristic diameter based), belonging to different theories/approaches, were tested with the observed data of the Middle Fork of Boulder Creek at Netherland (Colorado) and Williams Fork near Leal (Colorado). It was found that the performance of the excess discharge theory based model is better. These results are in accordance with the results of the studies carried out by USGS [25], Milhous [18] and Inpasihardjo [15]. The poor performance of the Bagnold's model confirmed the viewpoint of Carson and Griffiths [8] who suggested a need of extensive calibration of the model. The performance of the Meyer-Peter and Mueller model was found poor perhaps because the data used in the model development was of finer size than that of the streams used for the testing purpose. The Parker et al. [21] model performed unsatisfactorily, probably because it is based on the subsurface material, concept of equal mobility, and the τ^*_{ri} (= 0.0876) parameter used in the model is site specific. These are reasons that could have pursued Parker [20] to develop his surface material based model. During the investigation, models generally performed inconsistently with different data sets in agreement with the study results of Schulits and Hill [23], White et al [26&27], Yang [29], Nakota [19], Gomez and Church [12], USGS [25], Woo et al. [28], Ashiq [2, 4 and 5], Sun and Donahue [24], Kleinhans and Rijn [16], Habersack and Laronne [13], Espinosa et al. [11] etc. The reasons why these models performed poorly have been mentioned earlier. Likewise, Carson and Griffith [8] have stated two main reasons for the

041-052·bed Load 9/20/05 12:29 PM Page 51

models' poor performance: a) shortage of data for coarse bed material rivers; and b) assumptions and boundary conditions used in the development of models. Bed load transport studies tend to be empirical and therefore are constrained by lack of data.

A deterministic model (Equation (13), MBB model) using the characteristic diameter approach and the excess discharge theory, based on the mixed size bed material (non uniform) and on the philosophy of the fitted exponents - developed from the uni-size bed-materials (using flume data), has been developed for field conditions. This model performed satisfactorily when tested with the observed data of the River Severn (Wales, UK) and North Fork of South Platte River (Colorado) and with the results of the Milhous [18] model- a model that performed best in the earlier test of models. However, when using this model one should be very careful about the computation of critical discharge value (q_c) as a small variation in it could considerably influence the computed bed load discharge. This model was tested with data that fell within the size range of bed material that was used in the model development; how it would behave outside this size range is still to be investigated. Therefore, before generalising the model for common use it should be tested with different data sets having a wide size range.

The MBB model has been extended for determining the bed load transport for channels with non-uniform cross-sections flow depths (i.e. surface flow width ≠ active bed width). Likewise, the model has also been further extended for the braided rivers. Owing to the lack of data, it was not possible to test the performance of the extended models' therefore they should be tested before further use. No other researcher has investigated this topic and the study here is therefore only an initial investigation of a possible relationship between bed load transport and water discharge for non-uniform cross-sectional flow depth channels.

SUMMARY

Performance of the existing bed load transport models, based upon different theories/approaches, was investigated. It was found that results from the excess discharge theory based models were relatively better though not satisfactory. To further improve this theory the MBB model (Equation (13)) for field conditions based on the mixed-size bed material data (published) has been developed by using the fitted exponent values (a new approach) instead of following the customary assumed exponent values approach. This model is based on the assumption that sediment is moving over the whole flow width of the channel cross-section (i.e. surface flow width = active bed width). Model's performance was tested with the observed data from the River Severn (Wales, UK) and North Fork of South Platte River at Buffalo (Colorado) and found satisfactory. Likewise, this model performed better when results were compared with the Milhous model. This model, later on, was extended for the non-uniform cross-sectional channels and braided channels.

ACKNOWLEDGEMENTS

Author gratefully acknowledges the help of Dr James C. Bathurst (Principal Research Officer, Water Resources Systems Research Unit) and Dr C. Nalluri (Reader) of the Civil Engineering Department (Newcastle University) during the study. The text of this paper has been reviewed by Dr B. Agnew of the Newcastle University, his contribution is therefore also acknowledged. ■

NOTATIONS

D_{50}	median size of bed surface material (m).
LPA	line of perfect agreement.
MBB	mixed-size bed material based model.
q	unit water discharge (m^3/sec/m).
q_c	critical unit water discharge (m^3/sec/m).
q_s	unit sediment discharge (m^3/sec/m).
$q_{s\,(A)j}$	unit bed load discharge (m^3/sec/m) for channel j.
q_{si}	unit bed load discharge (m^3/sec/m) for channel i.
Q_b	total bed load discharge (m^3/sec).
R	correlation coefficient.
S	channel slope (m/m).
W	mean channel (surface) width (m).
W_A	mean active bed width (m).
W_i	mean water surface flow width for channel i (m).
W_{Aj}	active bed width of channel j (m).
α	coefficient.
β	relationship exponent.
τ^*_{ri}	reference shear stress parameter used in Parker et al. (1982).

REFERENCES

[1] J, Aitchison, The statistical analysis of compositional data, New Yourk: Chapman and Hall Company, 1986.

[2] M. Ashiq, "Bed load transport models for coarse bed material rivers" Ph.D. Thesis submitted to the Department of Civil Engineering, University of Newcastle Upon Tyne, UK, pp. 402, 1997.

[3] M. Ashiq, "Role of active bed width in bed load transport - coarse bed rivers" Proceedings of Seventh International Symposium on River Sedimentation, Civil Engineering Department, The University of Hong Kong, Hong Kong, December 16 -18, 1998.

[4] M. Ashiq, "Bed load transport in coarse bed material rivers- a review" Journal- Institution of Engineers, Malaysia, Vol. 60, No.1, pp. 29 – 39, 1999.

[5] M. Ashiq, J. I. Finnie, and F. Watts, "Optimal sediment discharge computation formulas for a gravel and cobble bed

041-052·bed Load 9/20/05 12:29 PM Page 52

river-a comparative approach" Proceedings of an International conference, NILE 2000, Development of Nile and Other Major Rivers, Cairo, Egypt, Vol. II, February, 1992.

[6] R. A. Bagnold, "An empirical correlation of bed load transport rates in flumes and natural rivers" Proc. Roy. Soc. London, A372, pp. 453-473, 1980.

[7] J. C. Bathurst, W.H. Graf, and H. H. Cao, "Bed load discharge equations for steep mountain rivers" Sediment Transport in Gravel-Bed Rivers, C.R. Thorne et al.(eds), John Wiley and Sons Ltd. Chichester, UK, pp. 453 – 491, 1987.

[8] M.A. Carson, and G.A. Griffiths, "Bed load transport in gravel channels" Journal of Hydrology (N.Z) Vol. 26, No.1, 1987.

[9] B.R. Colby, "Practical computations of bed-material discharge" J. of Hydraulics Div., ASCE, Vol. 90, No. HY2, 1964.

[10] M.P. DuBoy, "Etudes du Regime et 1' Action Exercee par les Eaux sur un lit a Fond de Graviers Indefiniment affouilable" Annales de Ponts et Chausses, Ser. 5, Vol. 18, pp. 141-195, 1879.

[11] B. M. Espinosa, R.W. Osterkamp, and L.V. Lopes, "Bed load transport in alluvial channels" J. Hydr. Eng., ASCE, 129(10), pp. 783-795, 2003.

[12] B. Gomez, and M. Church, "An assessment of bed load transport formulae for gravel bed rivers" Water Resources Research, Vol. 25, No. 6, pp.1161-1186, 1989.

[13] H. M. Habersack, and J.B. Laronne, "Evaluation and improvement of bed load discharge formulas based on Helley-Smith sampling in an Alpine gravel bed river" J. Hydr. Eng., ASCE, 128(5), pp. 484-499, 2002.

[14] A. Hald, "Statistical theory with engineering applications" A Wiley Publication on Statistics, 1952.

[15] K. Inpasihardjo, "Bed load transport of nonuniform size sediment in mountain rivers" Ph.D. Thesis, Department of Civil Engineering, University of Newcastle Upon Tyne, UK, pp. 454, 1991.

[16] M.G. Kleinhans, and V. Rijn, "Stochastic prediction of sediment transport in sand-gravel bed rivers" J. Hydr. Eng., ASCE, 128(4), pp. 412-425, 2002.

[17] E. Meyer-Peter, and R. Mueller, "Formula of bed load transport" Proceedings of 2nd Meeting of IAHR, Stockholm, 1948.

[18] R.T. Milhous, "On the selection of sediment transport equations" Proceeding of International Symposium: Sediment Transport Modelling. Hydr. Div. ASCE, New Orleans, Louisiana (USA), 1989.

[19] T. Nakota, "Test of selected sediment transport formulas" J. Hydr. Div., ASCE, 116 (3), pp. 362-379, 1987.

[20] G. Parker, "Surface based bed load transport relation for gravel bed rivers" J. Hydraulic Research, 28(4), pp. 417-436, 1990.

[21] G. Parker, P.C. Klingeman, and D.G. McLean, "Bed load and size distribution in paved gravel-bed stream" J. Hydr. Div., ASCE, 108(HY4), pp. 544-571, 1982.

[22] A. Schoklitsch, Handbuch des Wasserbaues, 3rd. Springer-Verlag, Vienna, 1962

[23] S. Schulits, and R.D. Hill, "Bed load formulas, Part A: a selection of bed load formulas" The Pennsylvania State University, College of Eng., University Park, Pennsylvania, 1968.

[24] Z. Sun, and J. Donahue, "Statistically derived bed load formula for any fraction of nonuniform sediment" J. Hydr. Eng., ASCE, 126(2), pp. 105-111, 2000.

[25] USGS, "Summary and use of selected fluvial sediment-discharge formulas" Water Resources Investigation Report 89-4026, edited by Stevens. H.H. and Yang C. T., Denver, Colorado (USA), 1989.

[26] W.R. White, H. Milli, and A. D. Crabbe, "Sediment transport theories - a review" Proceedings of Institution of Civil Engineers, London, Part 2, No. 59, pp.265-292, 1975.

[27] W. R. White, H. Milli, and A. D. Crabbe, "Sediment transport; an appraisal of available methods" Rep. 119, Hydraulics Res. Stat., Wallingford, England, 1978.

[28] H. Woo, K. Yoo, and B. Seoh, "Performance test of some selected sediment transport formulas" Proceedings of ASCE, National Conference on Hydraulics Engineering, San Diego, California, Vol. 1, p. 694-699, 1990.

[29] C. T. Yang, "Unit stream power equation for gravel" J. Hydr. Eng., ASCE, 110(12), pp. 1783-1797, 1984.

053-060·highly reactive 9/20/05 12:38 PM Page 53

HIGHLY REACTIVE ELECTROGENERATED ZINC: PREPARATION AND ITS USE IN CROSS-COUPLING REACTIONS

Aishah Abdul Jalil[1], Sugeng Triwahyono[2], Kurono Nobuhito[3], Takasugi Shingo[3], and Tokuda Masao[3]

[1]*Department of Chemical Engineering, Faculty of Chemical and Natural Resources Engineering,*
[2]*Ibnu Sina Institute for Fundamental Science Studies, Universiti Teknologi Malaysia, 81310 UTM Skudai, Johor*
[3]*Division of Molecular Chemistry, Graduate School of Engineering, Hokkaido University, Sapporo 060-8628, Japan*

ABSTRACT

Highly reactive zinc metal was prepared by electrolysis of a N,N-dimethylformamide (DMF) solution containing naphthalene and a supporting electrolyte in a one-compartment cell fitted with a platinum cathode and a zinc anode. This highly reactive electrogenerated zinc (EGZn/Naph) was used for transformation of bromoalkanes into the corresponding organozinc bromides, which can not be achieved by the use of usual zinc metals. Reaction of the organozinc compounds were thus prepared with various aryl iodides in the presence of 5 mol% of palladium catalyst to give the corresponding cross-coupling products in high yields. Arylzinc iodides were also prepared by the use of this highly reactive zinc, and they were reacted with other iodides to give the corresponding cross-coupled biaryls in good yields.

Keywords : *Highly Reactive Zinc, Preparation, Cross-Coupling, Palladium Catalyst*

1.0 INTRODUCTION

Organozinc compounds are very useful organometallic compounds for the forming reaction of carbon-carbon bonds [1]. Organozinc halides can usually be prepared by direct insertion of zinc metal into organic halides, but commercially available zinc metal is generally poorly reactive [2]. Therefore, activation of the metal is necessary for preparation of organozinc halides. Various method of zinc activation, such as the reduction of zinc halide with alkaline metal or alkali metal naphthalenide, have been reported [3]-[5]. These methods, however, require high temperatures and long reaction times, or vigorous stirring during the reaction.

A new method for preparation of reactive zinc by electrolysis and its use in facile isoprenylation [6] and allylation of aldehydes and ketones was reported elsewhere [7],[8]. It was shown that this electrogenerated reactive zinc (EGZn) was an aggregation of very fine crystalline zinc particles with a large surface area [8]. A facile preparation of organic compounds from functionalized alkyl iodides by using EGZn and their cross-couplings with aryl halides (Scheme 1), was also reported [9].

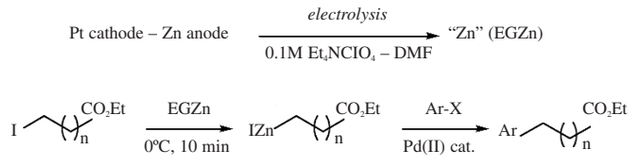

Scheme 1

However, no organozinc compounds have been obtained from alkyl bromides or were only obtained in very low yields from the corresponding organic bromides, even by the use of reactive EGZn. Recently, the authors have developed a new electrochemical method for preparation of more highly reactive zinc by using naphthalene as a mediator. Such methods for preparing reactive zinc are very convenient and useful in organic synthesis. In this paper, the authors report a new method for preparing highly reactive zinc by electrolysis and its use in cross-coupling reaction of bromoalkanes with aryl iodides as well as in aryl-aryl cross-coupling reaction.

2.0 EXPERIMENTAL

A. General methods

IR spectra were recorded on a JASCO IR-810 infrared spectrometer (neat between NaCl plates). ^{1}H NMR spectra were recorded on a JEOL JNM-EX270 (270 MHz) and JNM-LA400FT NMR (400 MHz). ^{1}H chemical shift is reported in ppm (δ) using tetramethylsilane as an internal standard. High and low resolution mass spectra were determined with a JEOL JMS-AX500 or JEOL JMS-SX102A spectrometer. Products were isolated by kugel rohr distillation or thin layer chromatograph and column chromatograph (Merck Kieselgel 60 PF_{254}).

B. Solvent and reagents

Commercially available anhydrous *N*,*N*-dimethylformamide (DMF) and tetrahydrofuran (THF) packed under a nitrogen atmosphere (Kanto Chemical) were used without further purification. Tetraethylammonium perchlorate was prepared according to the previous reported method [9]. The zinc plate (Nilaco) is commercially available in more than 99.9%

053-060·highly reactive 9/20/05 12:38 PM Page 54

purities, and was washed with 2N HCl, methanol, acetone and dried before electrolysis. Ethyl 4-bromobutanoate, ethyl 3-bromo-propanoate, 4-bromobutanenitrile, bromocyclohexane, bromohexane, iodobenzene are commercially available, and were purified by distillation prior to use. 4-Iodoacetophenone and 4-iodoanisole are also commercially available and were used without further purification. Naphthalene (Junsei Chemical, 99%) was used after recrystallisation from methanol.

C. Preparation of electrogenerated highly reactive zinc (EGZn/Naph)

A normal one-compartment cell equipped with a magnetic stirrer and a serum cap was used. Electrogenerated highly reactive zinc (6 mmol) was prepared by the electrolysis of a DMF solution (10 ml) containing 0.1M Et_4NClO_4 (230 mg) and naphthalene (12 mmol) in a one-compartment cell fitted with a platinum plate cathode (2x2 cm^2) and a zinc plate anode (2x2 cm^2). Electrolysis was carried out at -10ºC at a constant current of 60 mA/cm^2 under nitrogen atmosphere. The quantity of electricity passed was 0.012 F, which corresponded to 2 F per mol pf zinc metal. The amount of EGZn/Naph was calculated from the weight of dissolved zinc anode metal. A solution containing EGZn/Naph was directly used for the preparation of organozinc compound after the zinc anode was removed from the electrolysis cell.

D. General procedure for cross-coupling reaction using EGZn/Naph

To a DMF solution containing EGZn/Naph was added ethyl 4-bromobutanoate **(1a)** (5 mmol) and the mixture was stirred at 50°C under nitrogen atmosphere for 1 h. DMF solution (5 ml) of aryl iodide (4 mmol) and $Pd(P(o\text{-Tol})_3)_2Cl_2$ (0.11 mmol) was added, and the reaction mixture was stirred at 70ºC for 3 h. The resulting mixture was quenched with HCl solution and filtered. The filtrate was extracted with diethyl ether (50 ml x 3) and the combined organic layers were washed with water (100 ml x 3), saturated $Na_2S_2O_3$ solution (100 ml x 1) and saturated NaCl (100 ml x 1) and dried over $MgSO_4$. After evaporation of diethyl ether, the crude product was purified by column chromatograph on silica gel with ethyl acetate-hexane (1:4) to give ethyl 4-phenylbutanoate **4**.

3.0 RESULTS AND DISCUSSIONS

A. ELECTROCHEMICAL PREPARATION OF HIGHLY REACTIVE ELECTROGENERATED ZINC (EGZn/Naph)

Electrochemically generated highly reactive zinc (EGZn/Naph) was readily prepared by electrolysis of a *N*,*N*-dimethylformamide (DMF) solution containing naphthalene and 0.1M tetraethyl ammonium perchlorate (TEAP) in a one-compartment cell fitted with a platinum cathode and a zinc anode. Electrolysis at -10ºC at a constant current of 60 mA/cm^2 in a nitrogen atmosphere was found to give highly reactive zinc. However, other polyaromatic compounds such as biphenyl, phenanthrene, and pyrene could also be used as mediators to obtain activated EGZn/PA (PA: polyaromatic compound). The reactivities of these EGZn/PA are summarised in Table 1. They were effective for the formation of organozinc compounds except anthracene, but naphthalene was chosen in the present transformation from the point of view of availability.

Table 1. Effect of various polyaromatic compounds on the reactivity of EGZn/Naph[a]

Entry	Polyromatic	Conversion (%)[a]
1		52
2	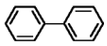	57
3	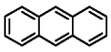	8
4	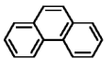	68
5	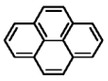	84

EGZn (6 mmol), Polyaromatic (12 mmol), Ethyl 4-bromobutanoate (5 mmol), 0.1M TEAP-DMF. [a] Conversion was determined by Gas chromatograph

At the cathode, a one-electron reduction of naphthalene molecule occurred to give naphthalene radical anion preferentially. The formation of the naphthalene radical anions was shown by the dark green color appeared on the surface of the cathode. On the other hand, at the anode, dissolution of the zinc metal occurred to give zinc ions, which were reduced by the naphthalene radical anions to give zero-valence highly reactive zinc, EGZn/Naph. The EGZn/Naph was an aggregation of very fine zinc particles with much smaller sizes than those of EGZn and was dispersed in the DMF solution [8]. Although the nature and the structure of EGZn/Naph are not clear at the present stage, it was found to be very reactive towards an oxidative addition to organic bromides.

The high reactivity of EGZn/Naph in the forming reaction of organozinc bromide (**2a**) from ethyl 4-bromobutanoate (**1a**) was compared with the reactivity of other zinc metals (Scheme 2). The results are summarised in Table 2.

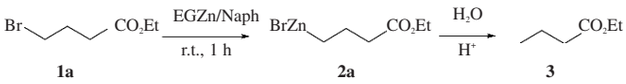

Scheme 2

These results show that the use of commercially available zinc or EGZn with the addition of naphthalene was not effective in terms of reactivity and that the presence of naphthalene molecules in the electrochemical reduction step is required for the preparation of much higher reactive zinc.

053-060·highly reactive 9/20/05 12:38 PM Page 55

Table 2. Transformation of bromoester 1a to organozinc 2a under various conditions[a]

Entry	Zn	Temperature (ºC)	Time (h)	Conversion of **1a** (%)[b]
1	Zn + Naph[c]	r.t.	18	0
2	Zn + Naph[c]	70	3	0
3	EGZn + Naph[d]	r.t.	3	37
4	EGZn/Naph	r.t.	1	95

[a]Ethyl 4-bromobutanoate (**1a**) (5 mmol) was reacted in DMF (10 ml) with zinc metal (6 mmol). [b]Determined by gas chromatograph analysis. [c]Commercially available Rare Metallic zinc (6 mmol) in the presence of naphthalene (12 mmol) was used. [d]EGZn (6 mmol) in the presence of naphthalene (12 mmol) was used

B. Cross-coupling of Functionalised Bromoalkanes with Aryl Iodides using EGZn/Naph

Ethyl 4-bromobutanoate (**1a**) can efficiently be transformed into the corresponding organozinc **2a** by a reaction with EGZn/Naph at 50ºC. Cross-coupling of **2a** with iodobenzene, 4-acetyliodobenzene or 4-methoxyiodobenzene at 70ºC for 2 h in the presence of 5 mol% $Pd(P(o\text{-}Tol)_3)_2Cl_2$ catalyst gave the corresponding cross-coupled products **4** in 75~97% isolated yields (Scheme 3) (Table 3, entries 1~3).

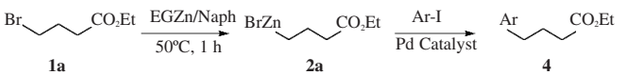

Scheme 3

Ethyl 3-bromopropanoate (**1b**), instead of ethyl 4-bromobutanoate (**1a**), was also transformed into the corresponding organozinc compound by a similar reaction with EGZn/Naph. Subsequent one-pot cross-coupling reactions of a DMF solution containing **2b** with various iodobenzenes in the presence of 5 mol% $Pd(P(o\text{-}Tol)_3)_2Cl_2$ catalyst at 70°C for 2 h gave the corresponding cross-coupled products **4** in 84, 81, and 63% isolated yields, respectively (Table 3, entries 4-6).

1-Bromobutanenitrile (**1c**) and bromohexane (**1d**) could also be converted into the corresponding organozinc bromides **2c** and **2d** by their reaction with EGZn/Naph. Palladium(II)-catalysed reaction of **2c** and **2d** with aryl iodide carrying electron-withdrawing or electron-donating substituents gave the corresponding cross-coupled product in almost high yields (Table 3, entries 7-9 and entries 10-12). The reaction of a secondary-alkyl bromide such as bromocyclohexane (**1e**) with EGZn/Naph also efficiently gave the corresponding alkylzinc bromide, which was reacted with aryl iodides in the presence of Pd(II) catalyst to give the corresponding cross-coupled products in good yields (Table 3, entries 13-15).

C. Aryl-aryl Cross-coupling using EGZn/Naph

Aryl iodides carrying a *p*-acetyl, *p*-methoxy-, or *p*-cyano group (**5**) can readily be transformed into the corresponding arylzinc iodides (**6**) by a reaction with EGZn/Naph. Preparation of arylzinc compounds is not readily achieved when usual zinc metal is used. This fact shows that the electrochemically generated EGZn/Naph has a very high reactivity. The reaction of arylzinc iodides (**6**) with other aryl iodides gave the cross-coupled biaryls (**6**) in good yields (Scheme 4).

Table 3. Cross-coupling of functionalised bromoalkanes (1a~1e) with Aryl Iodides using EGZn/Naph[a]

Entry	Bromide	ArI	Product	Isolated Yield (%)
1	$Br(CH_2)_3CO_2Et$ (**1a**)	C_6H_5I (**5a**)	$C_6H_5(CH_2)_3CO_2Et$) (**4a**)	97
2	$Br(CH_2)_3CO_2Et$ (**1a**)	$p\text{-}CH_3COC_6H_4I$ (**5b**)	$p\text{-}CH_3COC_6H_4(CH_2)_3CO_2Et$ (**4b**)	84
3	$Br(CH_2)_3CO_2Et$ (**1a**)	$p\text{-}CH_3OC_6H_4I$ (**5c**)	$p\text{-}CH_3OC_6H_4(CH_2)_3CO_2Et$ (**4c**)	75
4b	$Br(CH_2)_2CO_2Et$ (**1b**)	C_6H_5I	$C_6H_5(CH_2)_2CO_2Et$) (**4d**)	84
5	$Br(CH_2)_2CO_2Et$ (**1b**)	$p\text{-}CH_3COC_6H_4I$	$p\text{-}CH_3COC_6H_4(CH_2)_2CO_2Et$ (**4e**)	81
6	$Br(CH_2)_2CO_2Et$ (**1b**)	$p\text{-}CH_3OC_6H_4I$	$p\text{-}CH_3OC_6H_4(CH_2)_2CO_2Et$ (**4f**)	63
7	$Br(CH_2)_3CN$ (**1c**)	C_6H_5I	$C_6H_5(CH_2)_3CN$ (**4g**)	89
8	$Br(CH_2)_3CN$ (**1c**)	$p\text{-}CH_3COC_6H_4I$	$p\text{-}CH_3COC_6H_4(CH_2)_3CN$ (**4h**)	91
9	$Br(CH_2)_3CN$ (**1c**)	$p\text{-}CH_3OC_6H_4I$	$p\text{-}CH_3OC_6H_4(CH_2)_3CN$ (**4i**)	97
10	$Br(CH_2)_5CH_3$ (**1d**)	C_6H_5I	$C_6H_5(CH_2)_5CH_3$ (**4j**)	89
11	$Br(CH_2)_5CH_3$ (**1d**)	$p\text{-}CH_3COC_6H_4I$	$p\text{-}CH_3COC_6H_4(CH_2)_5CH_3$ (**4k**)	85
12	$Br(CH_2)_5CH_3$ (**1d**)	$p\text{-}CH_3OC_6H_4I$	$p\text{-}CH_3OC_6H_4(CH_2)_5CH_3$ (**4l**)	71
13	$C_6H_{11}Br$ (**1e**)	C_6H_5I	$C_6H_5C_6H_{11}$ (**4m**)	77
14	$C_6H_{11}Br$ (**1e**)	$p\text{-}CH_3COC_6H_4I$	$p\text{-}CH_3COC_6H_4C_6H_{11}$ (**4n**)	71
15	$C_6H_{11}Br$ (**1e**)	$p\text{-}CH_3OC_6H_4I$	$p\text{-}CH_3OC_6H_4C_6H_{11}$ (**4o**)	76

[a] Bromides **1a-1e** (5 mmol), except **1b** were reacted at 50ºC for 1 h with EGZn/Naph (6 mmol), and the resulting DMF solutions containing **2a-2e** were reacted with ArI (4 mmol) in the presence of 5 mol% $Pd(P(o\text{-}Tol)_3)_2Cl_2$ at 70ºC for 2 h. [b] Bromides **1b** (5 mmol) was reacted at 0ºC for 1 h with EGZn/Naph (6 mmol), and subsequent cross-coupling reaction is similar as above

053-060·highly reactive 9/20/05 12:38 PM Page 56

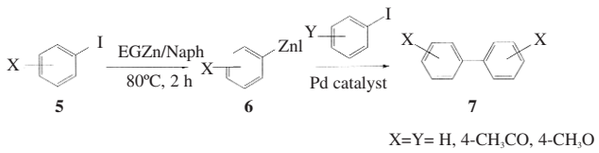

Scheme 4

The results are summarised in Table 4. Lower yield was observed from the reaction of organozinc compound of 4-methoxy-iodobenzene with iodobenzene (entry 3).

D. Reaction Pathways

Probable reaction pathways of the preparation of EGZn/Naph are shown in Scheme 4. Electrolysis of a DMF solution with a platinum cathode and a zinc anode results in anodic dissolution of zinc metal to give zinc ions. On the other hand, at the cathode, a one-electron reduction of naphthalene molecule occurs to give radical anion of naphthalene, which was shown by the appearance of the dark green color on the surface of the cathode [10]. Reduction of zinc ion with naphthalene radical anion would give zero-valent reactive zinc (EGZn/Naph).

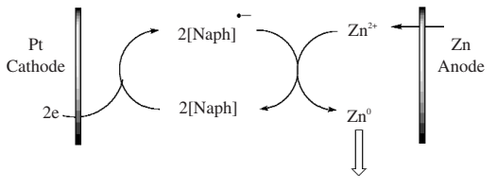

Scheme 4

Probable reaction pathways of the present cross-couplings are shown in Scheme 5. Oxidative addition of Pd(0) to aryl halides would give Ar-Pd-X, which undergoes metal exchange reaction with organozinc bromide **2** to give an intermediate Ar-Pd-R. Reductive elimination of Ar-Pd-R would give the cross-coupling product, ethyl 2-arylpropenoates **4**.

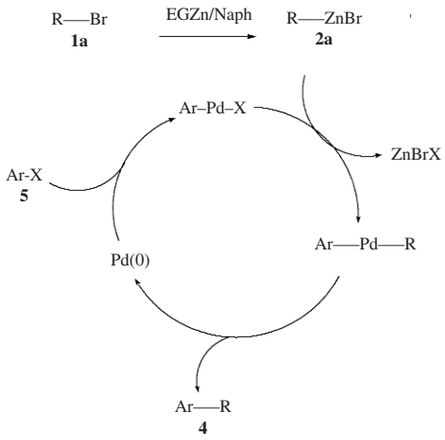

Scheme 5

4.0 CONCLUSION

A new electrochemical method for preparation of highly reactive zinc (EGZn/Naph) by using naphthalene as a mediator in the electrolysis was developed. The corresponding organozinc bromide could readily be prepared under mild conditions by the reaction of ethyl 4-bromobutanoate with EGZn/Naph. Subsequent cross-coupling reaction of the organozinc bromide with various aryl halides readily took place in the presence of a palladium catalyst to give the corresponding cross-coupled products in high yields.

ACKNOWLEDGEMENT

This work was supported by a Grant-in-Aid for Scientific Research (B) (No. 11450342) from the Ministry of Education, Science, Sports and Culture, Japan. ■

(Note: The spectral data of the products are shown in Table 5 on page 69)

Table 4. Paladium catalysed Aryl-aryl Cross-coupling reaction using EGZn/Naph[a]

Entry	ArI	ArI	Product	Isolated Yield (%)
1	C_6H_5I	*p*-$CH_3COC_6H_4I$	*p*-$CH_3COC_6H_4C_6H_5$	82
2	*p*-$CH_3COC_6H_4I$	*p*-$CH_3OC_6H_4I$	*p*-$CH_3COC_6H_4C_6H_4OCH_3$-*p*	70
3	*p*-$CH_3OC_6H_4I$	C_6H_5I	*p*-$CH_3OC_6H_4C_6H_5$	51[b]

[a] Iodobenzene, 4-acetyliodobenzene or 4-methoxyiodobenzene (5 mmol), were reacted at 80ºC for 2 h with EGZn/Naph (6 mmol), and the resulting DMF solutions were reacted with ArI (4 mmol) in the presence of 5 mol% $Pd(P(o\text{-Tol})_3)_2Cl_2$ at 70ºC for 2 h. [b] Cross-coupling was carried out in THF solution

053-060·highly reactive 9/20/05 12:38 PM Page 57

REFERENCES

[1] P. Knochel and P. Jones, *Organozinc Reagents. A Practice Approach*. Oxford University: New York, pp 157, 1999.

[2] A. Furstner, P. Knochel, and R. Singer, "A Convenient Preparation of Functinalized Arylzinc Compounds by the Reaction of Zinc/silver-graphite with Aryl Iodides," *Tetrahedron Lett.*, 35, pp 1047-1050, 1994.

[3] A. Furstner, "Chemistry of and with Highly Reactive Metals," *Angew. Chem., Int. Ed. Engl., 32*, pp 164-189, 1993.

[4] L. Zhu, R. M. Wehmeyer and R. D. Rieke, "The Direct Formation of Functionalized Alkyl(aryl)zinc Halides by Oxidative Addition of Highly Reactive Zinc with Organic Halides and Their Reactions with Acid Chlorides, "Unsaturated Ketones, and Allylic, Aryl, and Vinyl Halides," *J. Org. Chem. 56*, pp 1445-1453. 1991.

[5] M. V. Hanson and R. D. Rieke, "1,4-Addition of Secondary and Tertiary Alkylzinc Bromides to "Unsaturated Ketones without a Copper Catalyst," *J. Am. Chem. Soc., 117*, pp 10775-10776, 1995.

[6] M. Tokuda, N. Mimura, T. Karasawa, H. Fujita and H. Suginome, "New Preparation of Reactive Zinc Metal by Electrolysis and Its Use for A Facile Isoprenylation of Aldehydes and Ketones," *Tetrahedron Lett., 34*, pp 7607-7610, 1993.

[7] M. Tokuda, in *Novel Trends in Electroorganic Synthesis*, S. Torii, Editor, Kodanhsa Ltd., Tokyo, pp 241, 1995.

[8] M. Tokuda, N. Kurono and N. Mimura, "New Electrochemical Preparation of Reactive Zinc with a Large Surface Area," *Chem. Lett.,* pp 1091-1092, 1996.

[9] N. Kurono, K. Sugita, S, Takasugi and M. Tokuda, "One-step Cross-coupling Reaction of Functionalized Alkyl Iodides with Aryl Halides by the Use of an Eectrochemical Method," *Tetrahedron, 55*, pp 6097-6108, 1999.

[10] W.S. John and C.R. Richard, "Catalytic Electrochemical Reduction of the Carbon-chlorine Bond," *Tetrahedron Lett*., 6, pp 393-396, 1975.

Table 5. Spectral data of the products

Product	bp°C/ mmHg	^{1}H NMR (ppm)	IR (neat, cm^{-1})	MS (70 eV), m/e	Analysis
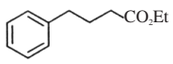 (**4a**)	97/4	7.23 (5H, m), 4.12 (2H, q, *J*=7.26 Hz), 2.65 (2H, t, *J*=7.59 Hz), 2.32 (2H, t, *J*=7.59 Hz), 1.96 (2H, quin, *J*=7.59 Hz), 1.25 (3H, t, *J*=7.26 Hz).	1734, 1498, 700	EIMS 192 (M^+, 60), 147 (76), 117 (18), 104 (100), 91 (85), 88 (79), 70 (25). HRMS Calcd for $C_{12}H_{16}O_2$ *m/z* 192.1124. Found *m/z* 192.1137.	$C_{12}H_{16}O_2$: C, 74.97; H, 8.39 Found: C, 74.75; H, 8.45
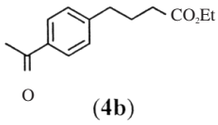 (**4b**)	126/0.2	7.89 (2H, d, *J*=8.42 Hz), 7.28 (2H, d, *J*=8.42 Hz), 4.13 (2H, q, *J*=7.26 Hz), 2.72 (2H, t, *J*=7.76 Hz), 2.59 (3H, s), 2.32 (2H, t, *J*=7.42 Hz), 1.99 (2H, m), 1.26 (3H, t, *J*=7.26 Hz).	1734, 1683, 1607, 1571, 1413	EIMS 234 (M^+, 58), 219 (19), 189 (12), 147 (100), 131 (26), 118 (7), 105 (6), 90 (9). HRMS Calcd for $C_{14}H_{18}O_3$ *m/z* 234.1274. Found *m/z* 234.1265.	$C_{14}H_{18}O_3$: C, 71.77; H, 7.74. Found: C, 71.83; H, 7.83.

053-060·highly reactive 9/20/05 12:38 PM Page 58

Product	bp°C/ mmHg	^{1}H NMR (ppm)	IR (neat, cm^{-1})	MS (70 eV), m/e	Analysis
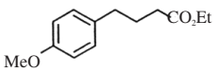 (**4c**)	99/0.2	7.09 (2H, dd, *J*=1.98, 4.61 Hz), 6.83 (2H, dd, *J*=1.98, 4.61 Hz), 4.12 (2H, q, *J*=7.10 Hz), 3.78 (3H, s), 2.59 (2H, t, *J*=7.43 Hz), 2.30 (2H, t, *J*=7.59 Hz), 1.92 (2H, m), 1.25 (3H, t, *J*=7.10 Hz).	1734, 1613, 1514, 1247, 1037	EIMS 222 (M^+, 30), 177 (20), 134 (100), 121 (63), 91 (10). HRMS Calcd for $C_{13}H_{18}O_3$ *m/z* 222.1198. Found *m/z* 222.1227.	$C_{13}H_{18}O_3$: C, 70.25; H, 8.16 Found: C, 70.22; H, 8.16
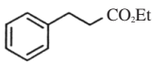 (**4d**)	85/2.6	7.24 (5H, m), 4.12 (2H, q, *J*=7.26 Hz), 2.95 (2H, t, *J*=7.59 Hz), 2.62 (2H, t, *J*=7.59 Hz),1.23 (3H, t, *J*=7.26 Hz).	1737, 1605, 1498	EIMS 178 (M^+, 48), 133 (16), 104 (100), 91 (53). HRMS Calcd for $C_{11}H_{14}O_2$. *m/z* 178.1046. Found *m/z* 178.1020.	$C_{11}H_{14}O_2$: C, 74.13; H, 7.92 Found: C, 73.91; H, 7.92.
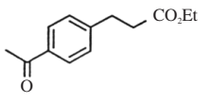 (**4e**)	108/0.25	7.89 (2H, d, *J*=8.29 Hz), 7.30 (2H, dd, *J*=8.29 Hz), 4.13 (2H, q, *J*=7.10 Hz), 3.01 (2H, t, *J*=7.76 Hz), 2.64 (2H, t, *J*=7.76 Hz), 2.58 (3H, s), 1.23 (3H, t, *J*=7.10 Hz).	1735, 1684, 1608, 1571, 1415	EIMS 220 (M^+, 49), 205 (100), 177 (11), 149 (9), 131 (18). HRMS Calcd for $C_{13}H_{16}O_3$ *m/z* 220.1151.	$C_{13}H_{16}O_3$: C, 70.89; H, 7.32 Found: C, 70.68; H, 7.36.
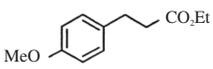 (**4f**)	79/0.16	7.12 (2H, d, *J*=8.29 Hz), 6.82 (2H, d, *J*=8.29 Hz), 4.12 (2H, q, *J*=7.26 Hz), 3.78 (3H, s), 2.89 (2H, t, *J*=7.76 Hz), 2.58 (2H, t, *J*=7.76 Hz), 1.23 (3H, t, *J*=7.26 Hz).	1736, 1613, 1515, 1248, 1037	EIMS 208 (M^+, 31), 134 (39), (100) 121 HRMS Calcd for $C_{12}H_{16}O_3$ *m/z* 208.1141. Found *m/z* 208.1120.	$C_{12}H_{16}O_3$: C, 69.21; H, 7.74 Found: C, 69.17; H, 7.80.

Product	bp°C/ mmHg	^{1}H NMR (ppm)	IR (neat, cm^{-1})	MS (70 eV), m/e	Analysis
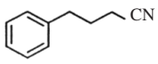 (**4g**)	75 /0.2	7.25 (5H, m), 2.78 (2H, t, *J*=7.26 Hz), 2.32 (2H, t, *J*=7.26 Hz), 1.98 (2H, qui, *J*=7.26 Hz)	2244, 1603, 1497	EIMS 145 (M^+, 36), 104 (25), 91 (100). HRMS Calcd for $C_{10}H_{11}N$ *m/z* 145.0879.	$C_{10}H_{11}N$: C, 82.72; H, 7.64; N, 9.65. Found: C, 82.72; H, 7.64; N, 9.61.
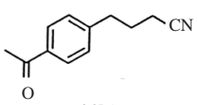 (**4h**)	120 /0.2	7.92 (2H, d, *J*=7.92 Hz), 7.30 (2H, d, *J*=7.92 Hz), 2.86 (2H, t, *J*=7.26 Hz), 2.60 (3H, s), 2.34 (2H, t, *J*=7.26 Hz), 2.01 (2H, qui, *J*=7.26 Hz).	2246, 1683, 1608, 1499, 1458	EIMS 187 (M^+, 18), 172 (100), 144 (7), 131 (4), 116 (9). HRMS Calcd for $C_{12}H_{13}ON$ *m/z* 187.0967.	$C_{12}H_{13}ON$: C, 76.98; H, 7.00; N, 7.48. Found: C, 76.43; H, 7.09; N, 7.48.
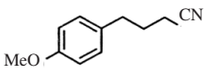 (**4i**)	95 /0.2	7.10 (2H, dd, *J*=2.97, 11.55 Hz), 6.84 (2H, dd, *J*=2.97, 11.55 Hz), 3.79 (3H, s), 2.72 (2H, t, *J*=7.26 Hz), 2.30 (2H, t, *J*=7.26 Hz), 1.95 (2H, qui, *J*=7.26 Hz).	–	EIMS 175 (M^+, 17), 121 (100), 91 (15), 77 (15). HRMS Calcd for $C_{11}H_{13}ON$ *m/z* 175.1023. Found *m/z* 175.1010.	$C_{11}H_{13}ON$: C, 75.40; H, 7.48; N, 7.99. Found: C, 75.20; H, 7.48; N, 7.95.
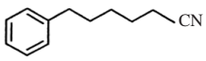 (**4j**)[a]	–	7.22 (5H, m), 2.60 (2H, t, *J*=7.59 Hz), 1.59 (2H, m), 1.32 (6H, m), 0.88 (3H, t, *J*=6.93 Hz).	1588, 1572, 1487, 1469, 1244, 1175	EIMS 162 (M^+, 36), 91 (100). HRMS Calcd for $C_{12}H_{18}$ *m/z* 162.2749. Found *m/z* 162.1394.	–
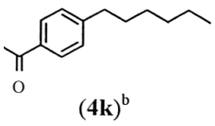 (**4k**)[b]	–	7.88 (2H, d, *J*=8.58 Hz), 7.27 (2H, d, *J*=8.58 Hz), 2.65 (2H, t, *J*=7.59 Hz), 2.58 (3H, s), 1.62 (2H, m), 1.30 (6H, m), 0.88 (3H, t, *J*=7.26 Hz).	1685, 1608, 1572, 1413, 1377,	EIMS 204 (M^+, 70), 189 (100), 148 (8), 133 (32), 91 (25), 43 (10). HRMS Calcd for $C_{14}H_{20}O$ *m/z* 204.3114. Found *m/z* 204.1517.	$C_{14}H_{20}O$: C, 82.30; H, 9.87. Found: C, 82.15; H, 9.97.

053-060·highly reactive 9/20/05 12:38 PM Page 60

Product	bp°C/ mmHg	^{1}H NMR (ppm)	IR (neat, cm^{-1})	MS (70 eV), m/e	Analysis
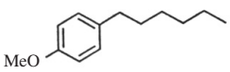 **(4l)**[c]	–	6.99 (2H, d, J=8.58 Hz), 6.72 (2H, d, J=8.91 Hz), 3.68 (3H, s), 2.44 (2H, t, J=7.59 Hz), 1.46 (2H, m), 1.20 (6H, m), 0.78 (3H, t, J=6.60 Hz).		EIMS 192 (19) 121 (100). HRMS Calcd for $C_{13}H_{20}O$ *m/z* 192.1514. Found *m/z* 192.1487	$C_{13}H_{20}O$: C, 81.20; H, 10.48. Found: C, 80.69; H, 10.54.
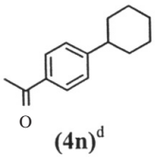 **(4n)**[d]	–	7.89 (2H, d, J=8.25 Hz), 7.29 (2H, d, J=8.25 Hz), 2.58 (3H, s), 2.56 (1H, m), 1.83 (4H, m), 1.39 (6H, m).	1690, 1610, 1461, 1267, 824	EIMS 202 (M^+, 83), 187 (100), 159 (13), 131 (49), 115 (26), 105 (17), 91 (29), 77 (13), 43 (13). HRMS Calcd for $C_{14}H_{18}O$ *m/z* 202.29. Found *m/z* 202.1353.	$C_{14}H_{18}O$: C, 83.12; H, 8.97. Found: C, 82.89; H, 8.99.
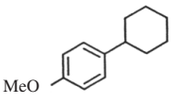 **(4o)**[e]	–	7.13 (2H, d, J=8.58 Hz), 6.84 (2H, d, J=8.58 Hz), 3.78 (3H, s), 2.44 (1H, m), 1.78 (5H, m), 1.32 (5H, m).	1515, 1461, 1249, 1045	EIMS 190 (90), 147 (100), 134 (17), 121 (72), 108 (7), 91 (13). HRMS Calcd for $C_{13}H_{18}O$ *m/z* 190.1358. Found *m/z* 190.1354.	$C_{13}H_{18}O$: C, 82.06; H, 9.53. Found: C, 82.04; H, 9.64.

[a-e] Separated by column chromatography on silica gel with hexane/ethyl acetate as eluant (5:1)

DETERMINATION OF PROBABILITY DISTRIBUTION FOR DATA ON RAINFALL AND FLOOD LEVELS IN BANGLADESH

M Ferdows*[1], Masahiro OTA[1], Roushan Jahan[1] , MNA Bhuiyan[2], Mubarak Hossain[3]

[1]*Department of Mechanical Engineering, Tokyo Metropolitan University, 1-1 Minami-osawa, Hachioji, Tokyo 192-0397, Japan*

[2]*Department of Mathematics, Dhaka University, Dhaka 1000, Bangladesh*

ABSTRACT

To evaluate flood (Discharge or water level) as well as rainfall frequency of given returns period, it is essential that one probability distribution function be used as a standard. In many countries one distribution function is used as a standard but in Bangladesh various frequency distribution function are in use. The main objectives of this study are to compare the probability distribution function for the application on flood and rainfall frequency analysis in Bangladesh. To compare it, three widely used distributions have been used namely: (1) Log Normal (Two parameters, LN2 and three parameters, LN3); (2) Extreme value Type-1 (EV1) or Grumbel and (3) Log-person type-3 (LP3) distributions. For this purpose, 5 set data of annual maximum runoff of different main rivers in Bangladesh and 3-days and 5-days rainfall data of Bhola Island (8 sets) have been used. The parameters of the distributions have been estimated by using the method of moments and method of maximum likelihood.

Keywords : *Flood frequency, Rainfall frequency, Probability distribution, Method of moments, Method of maximum likelihood*

INTRODUCTION

Knowledge of the magnitude and probable frequency of recurrence of floods and rainfall is necessary for the proper design of hydraulic structures such as dams, bridges, culverts, levees, highways, sewage disposal plants, industrial building etc. Return periods are find as per design policy of such structures viz. flood of 50 years return period are evaluated for embankments and bridges, that of return period 100 years for barrage and culverts

In 1880-1890, Herchel and Freeman first applied the frequency analysis of stream flow data to flood studies by means of graphical procedure using flow duration curves. A large number of papers on the application of Fisher - Tippet theory of extreme values to flood frequency analysis were published [6]. Later, many other hydrologists worked on the extreme value theory to flood frequency analysis, [3, 7, 10, 11, 14, 15, 16]

The frequency analysis of discharge data of West Bengal rivers by means of graphical procedures using flow duration curves has been studied by [2, 13] and discussed various issues related to section of probability distribution function for flood frequency analysis. In the various rivers discharge data in Bangladesh, MPO (1986), [1, 4, 12] have been used different probability distribution and suggested that LP3 distributions are suitable for Bangladesh for the frequency analysis of discharge data. It was found from all of the above study that they have used only discharge data but in our study discharge as well as rainfall data have been used.

The objective of this study is to compare the probability distribution function for the application of flood frequency as well as rainfall frequency analysis considering annul maximum runoff and rainfall data at different rivers and places in Bangladesh. In this study three widely used distributions have been compared by using 5 sets of annual maximum runoff data in different main rivers, 4 sets of 3-days rainfall data and 4 sets of 5-days rainfall data of Bhola Island in Bangladesh. For the literature survey we have visited Surface water modeling center (SWMC), Bangladesh water development board (BWDB), Institute of flood control and drainage research (IFCDR), Roorkee university (India) etc. for several times and collected important literature related to the work mentioned above.

METHODOLOGY

Probability distribution functions used:

Probability distribution functions of discrete and continuos random variables are used to fit distributions in hydrology. There are many distributions that are found useful for the hydrological frequency analysis. The Bangladesh water development board which designs and implements all large-scale flood control projects uses the Gumbel distribution. A few departments and consulting firms use the log normal (LN) distribution. The log-Pearson type-3 (LP3) distribution has been used in the preparation of a national water plan. Three widely used probability functions were compared in this study. These three probability distribution function and the parameters involved in each function are given below.

Log-normal distribution (LN)

The probability density function of this distribution in the case of three parameters (LN3) is

$$f(x) = \frac{1}{(x-\theta)\sigma_y\sqrt{2\pi}} \exp\left[-\frac{\{\text{In}\,(x-\theta)-\mu_y\}^2}{2\sigma_y^2}\right],\ x>\theta \qquad (1)$$

Where μ_y and σ_y are the mean and standard deviation of the natural logarithms of x and θ is a number.

The probability density function of this distribution in the case of two parameters (LN2):

$$f(x) = \frac{1}{x\sigma_y\sqrt{2\pi}} \exp\left[\frac{-(\text{In}\,x-\mu_y)^2}{2\sigma_y^2}\right] \qquad (2)$$

Where σ_y and μ_y are parameters stated above.

Extreme Value Type-1 or Grrmbel Distribution (EV1)

The probability density function of this distribution is

$$f(x) = \exp\left[-\exp\left(-\frac{x-\xi}{\alpha}\right)\right] \qquad (3)$$

Where $f(x)$ s the non-excedence probability for the value of x, ξ is a location parameter and α is scale parameter.

Log Pearson Type-3 Distribution (LP3)

The probability density function of Person Type-3 distribution is

$$f(x) = \frac{1}{\alpha x\Gamma(\beta)}\left[\frac{x-\nu}{\alpha}\right]^{(\beta-1)} \exp\left[-\frac{x-\nu}{\alpha}\right] \qquad (4)$$

Where α, β and ν are the shape, scale and location parameters to be estimated from the sample and $\Gamma(\beta)$ is the gamma function.

If the logarithm, lnx of a variable x are distributed as a Pearson Type-3 variable, then the variable x will be distributed as a Log Pearson Type-3 with probability density function

$$f(x) = \frac{1}{\alpha x\Gamma(\beta)}\left[\frac{\text{In}\,x-\nu}{\alpha}\right]^{(\beta-1)} \exp\left[-\frac{x-\nu}{\alpha}\right] \qquad (5)$$

Where α, β and Γ are the parameters as before.

1.2 Method of estimating distribution function parameters

The estimation methods techniques are used for estimating various parameters from sample values in such a way that they depart from the population parameters to a minimum. For estimating the parameters from the sample of data, method of moments (MM) and the method of maximum likelihood (MML) have been used in this study. The maximum likelihood method is a standard statistical procedure used in fitting a variety of hydrological data [5, 8].

1.3 Data Used in this analysis

The annual maximum discharge and 3 days and 5-days rainfall data have been used in this study. The data have been found from the Bangladesh water development board and Institute of flood control and drainage research. For the computation of statistical probability distribution a total number of 5 sets discharge data and 8 sets of rainfall data have been selected for this study on various types of rivers and places in Bangladesh. The discharge data record covers up to the year 2000 and rainfall data covers up to 2000 in some cases as given in table-1. The length of annual maximum discharge data lies between 25 to 63 years and rainfall data lies between 11 to 35 years as given in table-2. Though there is some break in the period of observation, the data are assumed to be continuous in this study.

Table-1: Discharge data (5 sets) of 5 different rivers in Bangladesh.

Serial Number	Station & River	Period of Record	Number of Years
1.	273Bhairab Bazar (Meghna)	1964 to 2000	29
2.	46-9L Bahadurabad (Brahmaputra)	1956 to 1992	36
3.	91-9L Baruria (Ganges)	1966 to 1992	25
4.	90 Hardinage Bridge (Ganges)	1964 to 2000	63
5	229-5LMymensingh(Old Brahmaputra)	1965 to 1992	26

Table-2: Rainfall data (8 sets) of 4 different rainfall station in Bhola (3-days and 5-days)

Serial Number	Rainfall Station	Period of Record	Number of Years
1.	Bhola city	1962 to 2000	35
2.	Burhanuddin	1962 to 1994	25
3.	Charfassion	1968 to 1978	11
4.	Daulatkhan	1961 to 1994	22

RESULTS AND DISCUSSION

For computations of the flood and rainfall frequency analysis by the distribution LN2, LN3, EV1 and LP3 have been developed and then used for this study. The application of above mentioned distributions have been used for the estimations of T year's events (viz. 2, 5, 10, 20, 50 and 100 years) through the method of moments and the method of maximum likelihood. All results are available in Appendices (in Appendix Al: Annual maximum discharge data of 5 sets in tabular from are given. In Appendix A2: Results of Discharge data are shown. B1: Rainfall data 3-days 4 sets and 5-days 4 sets in tabular form are given and Appendix B2: Results of Rainfall data are shown)

CONCLUSION

From this study, it is found that LP3 distribution give reasonably good results for the flood frequency as well as rainfall frequency analysis. It gives moderate or average results out of the other distributions.

It is conclude that one may use LP3 distribution for the flood as well as rainfall frequency analysis in Bangladesh. For the present study (only six months duration) the limited number of flood (maximum discharge) and rainfall data have been used. For more confirmation a large number of data can be used for the further study. ■

REFERENCE

[1] Chowdhury, J.U and Karim, M.A. (1993), Selection of Probability Function for Flood Frequency Analysis in Bangladesh. Institute of Flood Control and Drainage Research, BUET, Dhaka Final Report, RO1/93.

[2] Cunnane, C. (1989) Statistical Distribution for Flood Frequency Analysis, World Meteorological Organization, Operational Hydrology Report No. 33, WMONo. 718, Secretarial of the World Meteorological Organization Geneva, Switzerland.

[3] Chow V.T. David R Maidment, and Larry W. Mays (1992), Hand book of Applied Hydrology, McGraw-Hill book company, U.S.A., Chapter 12.

[4] Flood Hydrology study (1992), AFP-25: Flood Medelling and Management, Report of Kruger Consult and ECOM. Flood Plan coordination Organization.dhaka.

[5] Farago, T., and R.W.Katz., 1990. Extremes and design values in climatology. World Meteorological organization, TD-No.386, Geneva, Switzerland.

[6] Gumbel, E.J (1941), Probability Interpretation of the Observed Return Periods of Floods, Trans. American Geophysics unions, vol. 22.

[7] Johnson, N, L and Lotz, S. (1970), Distribution in Statistics, Continuous Univariate Distribution-1. A Wiley- and Son. New-Yorkk.

[8] Kite,G.W,1977. Frequency and risk analysis in Hydrology. Water resource publications, Fort collins, co,224 p.

[9] Master Plan Organization (1986), Floods and Storms, Technical Report, No. 11

[10] Mutreja. K.N. (1986) Applied Hydrology, Chap-3 and Chap-13, Tata McGraw-Hill Publishing Company Limited, New Delhi.

[11] Nash. J.E and Amoracho, J. (1986), The Accuracy of Predication of Flood of High return Period. Water Resources Research vol. 2 No. 2.

[12] Rahman. M.R. and Ahmed. S.M.U. (1986), A Comparative Study of Flood Frequency Analysis in Bangladesh. Journal of the Institution of Engineer, Bangladesh. vol. 14 No.-2.Page 31-37.

[13] Roy, S.K. (1985), Flood Frequency Studies for Bhagirathi River (West Bengal, Unesco Sponsored International Hydrology Course, Universityof Roorkee-247667, India.

[14] Subramanya, K. (1994), Engineering Hydrology, Chap-7, Tata McGraw-Hill Publishing Company Limited, New Delhi. (2nd edition)

[15] Singh, V.P. (1992), Elementary Hydrology, Chapter-25, Hall of India Private Limited, New Delhi.

[16] Sir William Hall Crow and Partmers Ltd. (1993) South West Area Water Resources Management project FAP4, Final report volume-3.

Appendix-A1 (I) (Detailed of discharge data, which have been used in this study, is given in the following tables)

Table 1: Annual maximum discharges (cumec) with year. Period of record used from 1961 to 2000, Number of years 29, Station Bhairab Bazar (273). River: Meghna. Designation of data set is D1

Year	1961	1962	1963	1964	1965	1966	1967	1968	1969	1970
Maxi Discharge	13141	7590	9487	12300	12100	14400	12700	13300	11500	16400
Year	1972	1973	1974	1975	1976	1981	1982	1983	1984	1985
Maxi Discharge	11500	12400	19500	12700	16700	11200	13500	16000	13600	14300
Year	1986	1987	1988	1989	1990	1991	1992	1993	2000	
Maxi Discharge	11100	15200	19800	15500	11700	14500	12800	19900	12394	

Table 2: Annual maximum discharges (cumec) with year. Period of record used from 1956 to 1992, Number of years = 36, Station: Baruria (46-9L). River: Brahmaputra. Designation of data set is D2

Year	1956	1957	1958	1959	1960	1961	1962	1963	1964	1965
Maxi Discharge	60400	65500	71300	68500	64800	53800	59400	56400	63100	64200
Year	1966	1967	1968	1969	1970	1972	1973	1974	1975	1976
Maxi Discharge	68900	69600	62300	56000	75000	66600	67300	91100	52200	65600
Year	1977	1978	1979	1980	1981	1982	1983	1984	1985	1986
Maxi Discharge	66600	56600	66100	61200	66500	55900	56500	77000	63800	43100
Year	1987	1988	1989	1990	1991	1992				
Maxi Discharge	74000	98600	71100	64400	84100	67500				

061-072·Determination 9/26/05 5:28 PM Page 64

Table 3: Annual maximum discharges (cumec) with year. Period of record used from 1966 to 1992, Number of years= 25, Station Baruria (91-9L). River: Ganges. Designation of data set is D3

Year	1966	1967	1968	1969	1970	1971	1973	1974	1975	1976
Maxi Discharge	81300	63600	80200	72700	84200	76600	90900	113000	93300	83500
Year	1977	1978	1980	1981	1982	1983	1984	1985	1986	1987
Maxi Discharge	81800	80400	109000	88200	89600	101000	107000	90500	81500	113000
Year	1988	1989	1990	1991	1992					
Maxi Discharge	132000	80000	83800	100000	726000					

Table 4: Annual maximum discharges 'Cumec' with year. Period of record: 1934-35 to 1995-96 except 1971-72, 96-2000.Number of years = 63,Station No = 90, Station: Harding Bridge, River = Ganges, Designation of data set is D4

Year	1934-35	1935-36	1936-37	1937-38	1938-39	1939-40	1940-41	1941-42	1942-43	
Maxi Discharge	46600	44000	45300	39400	47800	35900	39100	38300	44700	
Year	1943-44	1944-45	1945-46	1946-47	1947-48	1948-49	1949-50	1950-51	1951-52	
Maxi Discharge	43300	43300	42200	49100	51200	61100	52600	52600	42200	
Year	1952-53	1953-54	1954-55	1955-56	1956-57	1957-58	1958-59	1959-60	1960-61	
Maxi Discharge	52600	50900	58600	60300	60100	46200	56200	52700	48000	
Year	1961-62	1962-63	1963-64	1964-65	1965-66	1966-67	1967-68	1968-69	1969-70	
Maxi Discharge	73200	58700	56100	49000	36800	41900	50800	45200	55200	
Year	1970-71	1971-73	1973-75	1973-74	1974-76	1977-77	1976-78	1977-79	1978-80	
Maxi Discharge	48700	38200	50700	50700	51100	65400	51100	67900	36900	
Year	1980-81	1981-82	1982-83	1983-84	1984-85	1985-86	1986-87	1987-88	1988-89	
Maxi Discharge	57600	47900	61600	60000	56500	50600	53500	76000	72300	
Year	1989-90	1990-91	1991-92	1992-93	1993-94	1994-95	1995-96	1999	2000	
Maxi Discharge	31600	51300	56000	41900	44800	46100	49100	55019	60952	

Table 5: Annual maximum discharges (cumec) with year. Period of record used from 1964 to1992, Number of years 26, Station Baruria (228-5) River: Old Brahmaputra. Designation of data set is D5

Year	1964	1965	1966	1967	1968	1969	1970	1974	1975	1976
Maxi Discharge	2830	3230	3490	3000	2900	2770	3250	3820	3060	3210
Year	1977	1978	1979	1980	1981	1982	1983	1984	1985	1986
Maxi Discharge	3550	2770	2630	3340	2690	2470	2370	4780	3070	1930
Year	1987	1988	1989	1990	1991	1992				
Maxi Discharge	3230	4910	2180	2060	2900	1490				

061-072·Determination 9/26/05 5:28 PM Page 65

Appendix-A2 (I) (Results and figures of discharge data)

Table 1: Comparison of flood frequency results using data D1 obtained by different methods of various desired return periods

Return periods (Years Distribution)	2	5	10	20	50	100
EV1 (cumec) MM: X_T MML: X_T	 13584 13519	 16101 15456	 17767 16739	 19366 17970	 21435 19563	 22985 20757
LN2 (cumce) MM and MML X_T	13742	15878	17125	18227	19553	20490
LN3 (cumce) MM: X_T MML: X_T	 23584 8751	 15741 10776	 17120 11921	 18411 12914	 20053 14086	 21271 14901
LP3 (cumce) MM (Direct): X_T MML (Indirect) X_T	 13599 13487	 16598 15641	 17039 17111	 18300 18556	 19914 21985	 21121 21985

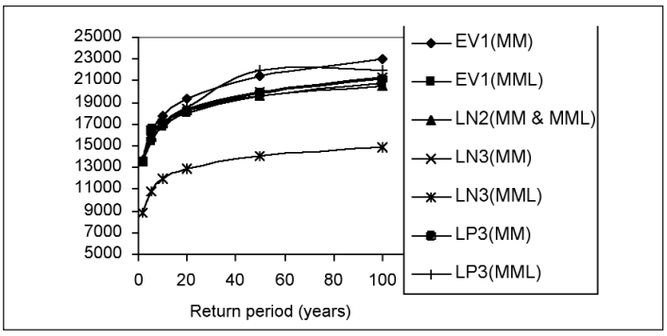

Figure 1: Comparison of flood frequency using the results given in Table 1

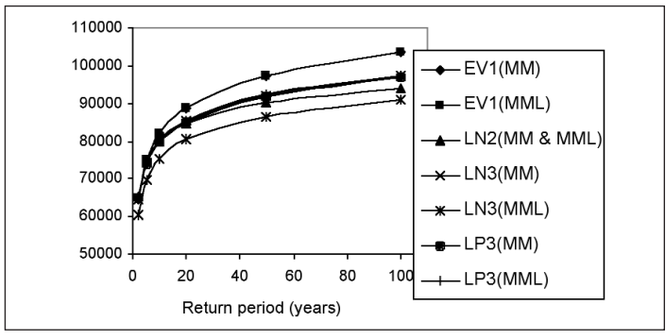

Figure 2: Comparison of flood frequency using the results given in Table 2

Table 2: Comparison of flood frequency results using data D2 obtained by different methods of various desired return periods

Return periods (Years Distribution)	2	5	10	20	50	100
EV1 (cumec) MM: X_T MML: X_T	 64555 64760	 75023 75150	 81954 82029	 88603 88627	 97208 97168	 103657 103569
LN2 (cumce) MM and MML X_T	65357	74585	79918	84607	90214	94158
LN3 (cumce) MM: X_T MML: X_T	 64715 60607	 740064 69873	 79939 75416	 85388 80397	 92247 86480	 97293 90837
LP3 (cumce) MM (Direct): X_T MML (Indirect) X_T	 64762 64791	 73929 74158	 79694 80024	 85059 85469	 91852 92344	 96882 97423

061-072·Determination 9/26/05 5:28 PM Page 66

Table 3: Comparison of flood frequency results using data D3 obtained by different methods of various desired return periods

Return periods (Years Distribution)	**2**	**5**	**10**	**20**	**50**	**100**
EV1 (cumec) MM: X_T MML: X_T	 87646 87477	 103796 101229	 114489 110334	 124746 119068	 138022 130373	 147971 138844
LN2 (cumce) MM and MML X_T	88674	102446	110479	117583	126128	132166
LN3 (cumce) MM: X_T MML: X_T	 87933 85637	 101846 99731	 110505 108856	 118486 117481	 128473 128543	 135783 136813
LP3 (cumce) MM (Direct): X_T MML (Indirect) X_T	 88014 87512	 101568 101477	 110012 110589	 117823 119282	 127655 130561	 134897 139104

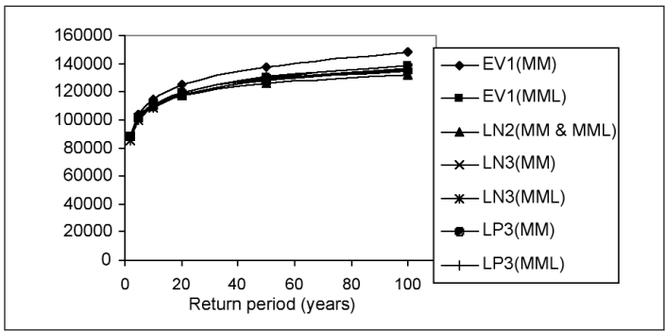

Figure 3: Comparison of flood frequency using the results given in Table 3

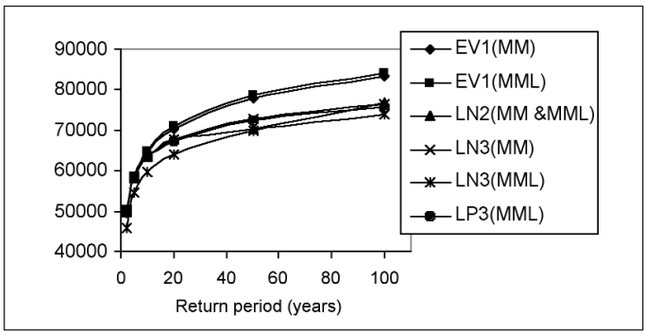

Figure 4: Comparison of flood frequency using the results given in Table 4

Table 4: Comparison of flood frequency results using data D4 obtained by different methods of various desired return periods

Return periods (Years Distribution)	**2**	**5**	**10**	**20**	**50**	**100**
EV1 (cumec) MM: X_T MML: X_T	 49350 49380	 58513 58728	 64581 64916	 70401 70852	 77934 78536	 83579 84294
LN2 (cumce) MM and MML X_T	49984	58395	63342	67741	70358	76833
LN3 (cumce) MM: X_T MML: X_T	 50081 45914	 58462 54462	 63324 59580	 67611 64183	 72751 69809	 76373 73841
LP3 (cumce) MM (Direct): X_T	Does Not Exist					
MML (Indirect) X_T	87512	101477	110589	119282	130561	139104

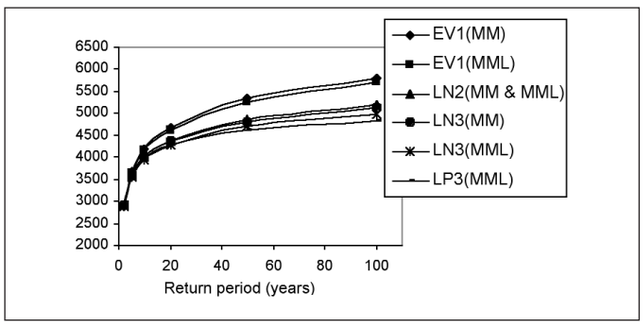

Figure 5: Comparison of flood frequency using the results given in Table 5

061-072·Determination 9/26/05 5:28 PM Page 67

Table 5: Comparison of flood frequency results using data D5 obtained by different methods of various desired return periods

Return periods (Years Distribution)	**2**	**5**	**10**	**20**	**50**	**100**
EV1 (cumec) MM: X_T MML: X_T	 2883 2890	 3668 3645	 4188 4146	 4686 4626	 5332 5247	 5815 5712
LN2 (cumce) MM and MML X_T	2906	3584	4000	4379	4849	5191
LN3 (cumce) MM: X_T MML: X_T	 2918 2887	 3594 3555	 4000 3944	 4364 4287	 4810 4700	 5130 4991
LP3 (cumce) MM (Direct): X_T MML (Indirect) X_T	 Does Not Exist 2965	 3619	 3975	 4272	 4608	 4831

Appendix-B1 (Rainfall data [(I) 3-days-4 sets (II) 5-days-4 sets])

Detailed of rainfall data, which have been used in this study, are given in the following tables.

Table 1: Annual maximum rainfall (3-days) in "mm" with year. Period of record used from 1962 to 2000.Number of years = 37, Name of station: Bhola. Designation of data set is 'R-1'

Year	1962	1963	1964	1965	1966	1967	1968	1969	1970
Maximum rainfall	226.6	258.8	293.2	159.5	281.7	212.1	226.8	380.2	192.8
Year	1971	1972	1973	1974	1975	1976	1977	1978	1979
Maximum rainfall	215.2	262.2	177.2	237.0	248.3	279.4	165.1	354.3	219.3
Year	1980	1981	1982	1983	1984	1985	1986	1987	1988
Maximum rainfall	212.9	235.0	205.5	236.2	251.4	256.1	464.8	292.1	267.7
Year	1990	1991	1992	1993	1994	1995	1996	1997	1998
Maximum rainfall	563.3	581.3	463.4	348.0	149.1	165	342.5	176.6	350.0
Year	2000								
Maximum rainfall	275								

Table 2: Annual maximum rainfall (3-days) in “mm” with year. Period of record used from 1962 to 1981 to 1994.Number of years = 25, Name of station: Borhanuddin, Designation of data set is ‘R-2’

Year	1962	1963	1964	1965	1966	1967	1968	1969	1970
Maximum rainfall	219.7	33.4	295.1	215.1	351.5	310.0	302.8	505.5	271.7
Year	1971	1972	1973	1974	1975	1976	1977	1978	1979
Maximum rainfall	215.8	192.6	302.0	318.0	388.1	290.2	232.9	259.3	268.0
Year	1980	1981	1982	1983	1984	1985	1986	1987	1988
Maximum rainfall	165.1	176.5	295.1	180.4	202.5	638.0	132.0		

Table 3: Annual maximum rainfall (3-days) in “mm” with year. Period of record used from 1968 to 1978. Number of years = 11,Station: Charfession, Designation of data set is ‘R-3’

Year	1968	1969	1970	1971	1972	1973	1974	1975	1976
Maximum rainfall	288.8	220.0	535.4	331.0	226.4	461.3	367.0	625.4	358.1
Year	1977	1978							
Maximum rainfall	252.4	294.6							

Table 4: Annual maximum rainfall (3-days) in "mm" with year. Period of record used from 1961 to 1994, Number of years = 22.Station: Designation of data set is 'R-4'

Year	1961	1962	1965	1966	1967	1968	1969	1971	
Maximum rainfall	221.4	182.9	240.1	122.7	316.6	347.7	292.1	249.0	
Year	1972	1973	1974	1975	1976	1978	1979	1980	
Maximum rainfall	227.8	223.5	188.0	457.2	660.4	359.3	330.2	237.5	
Year	1981	1990	1991	1992	1993	1994			
Maximum rainfall	185.9	474.4	616.4	118.9	487.2	255.5			

Table 5: Annual maximum rainfall (5-days) in "mm" with year. Period of record used from 1962 to 2000. Number of years = 37,Station: Bhola. Designation of data set is 'R-5'

Year	1962	1963	1964	1966	1967	1968	1969	1970	
Maximum rainfall	250.7	287.8	319.4	228.3	282.2	305.1	294.9	407.7	
Year	1971	1972	1973	1974	1975	1976	1977	1978	
Maximum rainfall	221.8	264.2	311.2	202.6	286.9	291.7	329.2	181.6	
Year	1979	1980	1981	1982	1983	1984	1985	1986	
Maximum rainfall	478.8	258.9	329.8	245.4	240.0	370.8	251.4	269.2	
Year	1987	1988	1989	1990	1991	1992	1993	1994	
Maximum rainfall	272.2	438.2	375.8	182.8	267.7	32.0	598.6	275.3	
Year	1995	1996	1997	1998	1999	2000			
Maximum rainfall	330.1	350.5	274.4	525.0	361.5				

Table 6: Annual maximum rainfall (5-days) in "mm" with year. Period of record used from 1962 to 1982, 1990 to 1994.Number of years = 25.Station: Borhanuddin. Designation of data set is 'R-6'

Year	1962	1963	1965	1966	1967	1968	1969	1970	
Maximum rainfall	274.2	357.0	296.6	232.9	415.2	401.2	343.6	562.4	
Year	1971	1972	1973	1974	1975	1976	1977	1978	
Maximum rainfall	356.1	279.3	200.0	328.6	427.5	482.6	339.5	281.1	
Year	1979	1980	1981	1982	1990	1991	1992	1993	
Maximum rainfall	288.3	315.0	283.2	209.6	291.0	300.6	399.0	591.1	
Year	1994								
Maximum rainfall	175.1								

Table 7: Annual maximum rainfall (5-days) in "mm" with year. Period of record used from 1968 to 1978,Number of years = 11.Station: Charfession. Designation of data set is 'R-7'

Year	1968	1969	1970	1971	1972	1973	1974	1975	
Maximum rainfall	383.1	250.9	272.5	408.7	282.2	462.3	514.3	917.5	
Year	1976	1977	1978						
Maximum rainfall	41.9	406.1	351.5						

061-072·Determination 9/26/05 5:28 PM Page 69

Table 8: Annual maximum rainfall (5-days) in "mm" with year. Period of record used from 1961 to 1982, 1990to 1994. Number of years = 22. Station: Daulatkhanh. Designation of data set is 'R-8'

Year	1961	1962	1965	1966	1968	1969	1970	1971	
Maximum rainfall	299.3	189.5	273.1	205.3	349.9	445.1	381.0	260.8	
Year	1972	1973	1974	1975	1977	1978	1979	1981	
Maximum rainfall	274.3	261.7	523.3	685.8	486.3	340.4	276.4	276.4	
Year	1982	1990	1991	1992	1993	1994			
Maximum rainfall	272.3	283.9	326.9	122.0	219.7	95.5			

Appendix-B2 (Results and figures of rainfall data)

Table 1: Comparison of Rainfall Frequency analysis results using data R1 obtained by different methods of various desired return

Return periods Distributions	**2**	**5**	**10**	**20**	**50**	**100**
LN2 (mm) MM and MML:X_T	259.7	353.7	415.7	475.0	552.0	610.0
LN3 (mm) MM:X_T MML: X_T	257.3 251.3	350.3 342.5	414.1 412.3	476.5 485.5	559.4 589.7	623.3 674.8
Lp3 (mm) MM (direct) : X_T MM (indirect) : X_T MML : X_T	258.1 248.9 251.0	349.0 338.0 338.0	411.2 409.5 407.0	472.2 488.5 480.5	553.8 608.2 588.9	617.1 712.7 681.3
EV1 (mm) MM : X_T MML : X_T	261.6 259.2	368.4 336.8	439.1 388.2	507.0 437.2	594.8 501.2	660.6 549.0

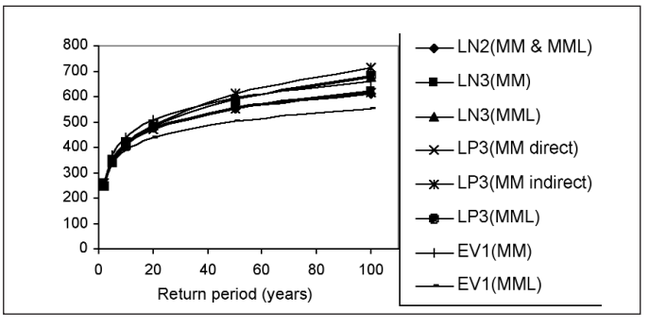

Figure 1: Comparison of rainfall frequency analysis using the results given in Table 1

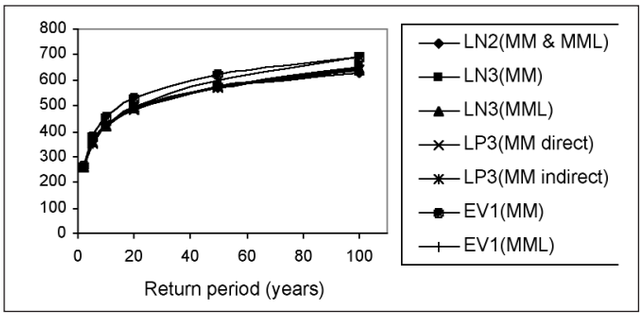

Figure 2: Comparison of rainfall frequency analysis using the results given in Table 2

Table 2: Comparison of Rainfall Frequency analysis results using data R2 obtained by different methods of various desired return periods (in years)

Return periods Distributions	**2**	**5**	**10**	**20**	**50**	**100**
LN2 (mm) MM and MML:X_T	263.5	360.8	425.2	487.0	567.4	628.2
LN3 (mm) MM:X_T MML: X_T	259.9 260.7	355.7 355.4	422.6 421.6	489.0 487.6	578.3 576.3	647.9 645.6
Lp3 (mm) MM (direct) : X_T MM (indirect) : X_T MML : X_T	261.3 257.4	354.1 351.7	418.7 422.0	483.1 495.6	570.4 600.7	639.1 687.8
EV1 (mm) MM : X_T MML : X_T	266.0 264.7	379.5 350.2	454.7 406.9	526.8 461.2	620.1 531.6	690.0 584.3

061-072·Determination 9/26/05 5:28 PM Page 70

Table 3: Comparison of Rainfall Frequency analysis results using data R3 obtained by different methods of various desired return periods

Return periods Distributions	**2**	**5**	**10**	**20**	**50**	**100**
LN2 (mm) MM and MML:X_T	326.3	449.8	532.0	611.1	714.3	792.5
LN3 (mm) MM:X_T MML: X_T	334.7 303.6	458.7 449.9	534.3 579.9	603.0 730.7	687.9 966.8	749.4 1176.6
Lp3 (mm) MM (direct) : X_T MM (indirect) : X_T MML : X_T	316.2 296.3	444.7 440.1	543.4 579.3	649.0 756.3	803.4 1069.4	933.8 1387.0
EV1 (mm) MM : X_T MML : X_T	331.8 326.5	494.5 438.2	602.2 512.2	705.5 583.2	839.3 675.1	939.5 743.9

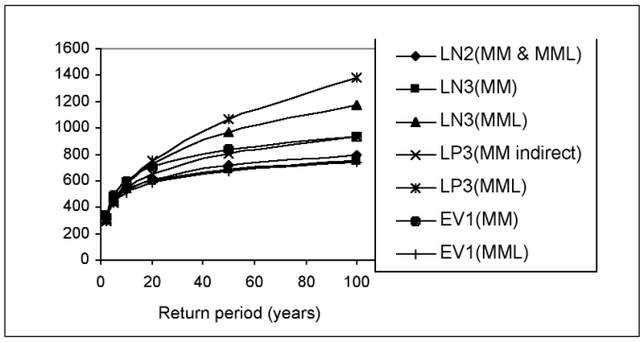

Figure 3: Comparison of rainfall frequency analysis using the results given in Table 3

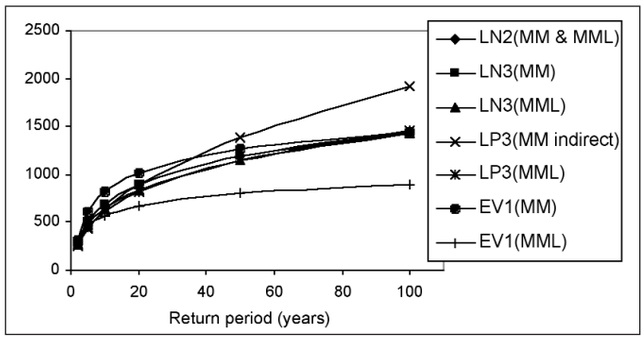

Figure 4: Comparison of rainfall frequency analysis using the results given in Table 4

Table 4: Comparison of Rainfall Frequency analysis results using data R4 obtained by different methods of various desired return periods (in years)

Return periods Distributions	**2**	**5**	**10**	**20**	**50**	**100**
LN2 (mm) MM and MML:X_T	274.8	500.6	685.0	887.4	1187.7	1442.3
LN3 (mm) MM:X_T MML: X_T	275.8 274.1	504.0 468.9	688.4 641.1	889.5 840.1	1185.8 1150.5	1435.7 1425.4
Lp3 (mm) MM (direct) : X_T MM (indirect) : X_T MML : X_T	258.9 273.1	438.8 452.4	628.2 615.8	886.2 814.1	1380.2 1146.1	1919.8 1464.2
EV1 (mm) MM : X_T MML : X_T	311.3 307.3	615.0 464.6	816.1 568.8	1009.0 668.7	1258.7 798.0	1445.8 894.9

061-072·Determination 9/26/05 5:28 PM Page 71

Table 5: Comparison of Rainfall Frequency analysis results using data R5 obtained by different methods of various desired return periods (in years)

Return periods Distributions	**2**	**5**	**10**	**20**	**50**	**100**
LN2 (mm) MM and MML:X_T	276.9	365.0	421.8	475.3	543.7	594.6
LN3 (mm) MM:X_T MML: X_T	282.1 225.1	369.9 310.2	422.4 357.4	469.6 398.0	527.2 445.2	568.4 477.8
Lp3 (mm) MM (indirect) : X_T	328.6	346.3	347.1	353.9	377.5	409.0
EV1 (mm) MM : X_T MML : X_T	277.1 281.7	377.0 393.2	443.2 467.1	506.6 537.9	588.7 629.5	650.3 698.2

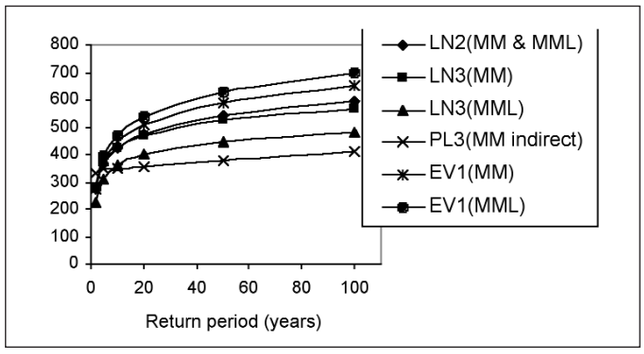

Figure 5: Comparison of rainfall frequency analysis using the results given in Table 5

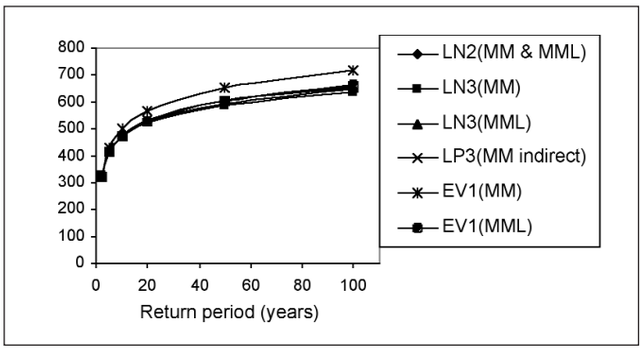

Figure 6: Comparison of rainfall frequency analysis using the results given in Table 6

Table 6: Comparison of Rainfall Frequency analysis results using data R6 obtained by different methods of various desired return periods (in years)

Return periods Distributions	**2**	**5**	**10**	**20**	**50**	**100**
LN2 (mm) MM and MML:X_T	322.6	414.4	472.5	526.4	594.6	644.9
LN3 (mm) MM:X_T MML: X_T	323.9 321.9	415.7 414.7	472.7 474.4	525.0 530.6	590.4 602.2	638.1 655.6
Lp3 (mm) MM (indirect) : X_T	321.7	414.2	474.1	530.7	603.4	658.0
EV1 (mm) MM : X_T MML : X_T	321.7 320.6	428.4 412.0	498.9 472.5	566.7 530.6	654.3 605.7	720.0 662.0

061-072·Determination 9/26/05 5:28 PM Page 72

Table 7: Comparison of Rainfall Frequency analysis results using data R7 obtained by different methods of various desired return periods (in years)

Return periods Distributions	**2**	**5**	**10**	**20**	**50**	**100**
LN2 (mm) MM and MML:X_T	389.0	550.7	660.5	676.4	908.6	1016.9
LN3 (mm) MM:X_T	381.8	538.7	653.0	769.5	930.3	1058.6
Lp3 (mm) MM (direct) : X_T MM (indirect) : X_T	386.0 357.5	533.7 493.1	640.3 628.4	749.4 802.7	901.5 1115.2	1024.3 1436.2
EV1 (mm) MM : X_T MML : X_T	398.5 393.4	612.6 513.5	754.3 593.0	890.2 669.3	1066.2 680.5	1198.1 842.0

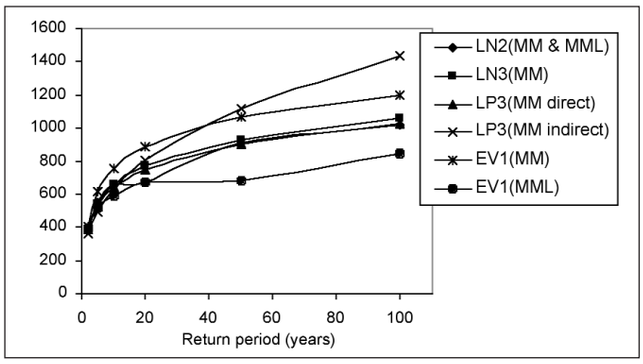

Figure 7: Comparison of rainfall frequency analysis using the results given in Table 7

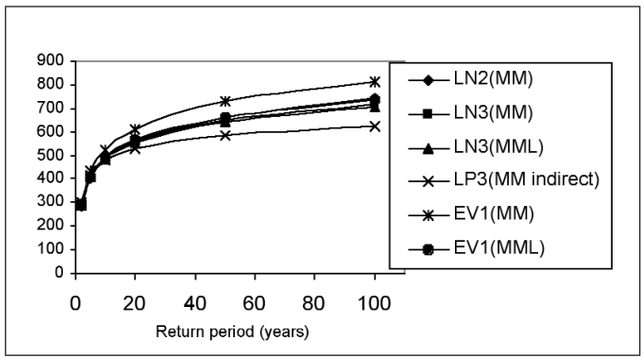

Figure 8: Comparison of rainfall frequency analysis using the results given in Table 8

Table 8: Comparison of Rainfall Frequency analysis results using data R8 obtained by different methods of various desired return periods (in years)

Return periods Distributions	**2**	**5**	**10**	**20**	**50**	**100**
LN2 (mm) MM and MML:X_T	286.0	403.8	483.6	561.2	663.5	741.9
LN3 (mm) MM:X_T MML: X_T	290.9 293.4	409.9 411.1	486.0 485.0	557.4 553.4	648.3 639.5	715.8 702.7
Lp3 (mm) MM (indirect) : X_T	301.3	416.0	478.0	529.7	585.7	621.6
EV1 (mm) MM : X_T MML : X_T	291.2 290.7	431.4 409.5	524.2 488.2	613.2 563.6	728.5 661.3	814.8 734.5

DEVELOPMENT AND PERFORMANCE EVALUATION OF A PROTOTYPE ELECTRIC HYBRID POWERTRAIN SYSTEM FOR AUTOMOTIVE APPLICATIONS

Azhar Abdul Aziz and Lim Chon Wei
Automotive Development Centre (ADC), Faculty of Mechanical Engineering,
Universiti Teknologi Malaysia, 81310 Skudai, Johor

ABSTRAK

Researchers at Universiti Teknologi Malaysia (UTM) have developed a dedicated hybrid power plant based on the parallel configuration using a gasoline engine coupled to a high performance electric motor, specifically targeted for automotive application. The aims are to achieve even lower exhaust emissions, better fuel economy and better performance than the conventional arrangement, demonstrating an alternative solution to the conventional power plant. The engine used is a 1.3 litre spark-ignition, coupled with a 27.5 kW Nexus electric motor. The control strategy developed in conjunction with the program is to use the electric drive motor for initial acceleration and for regeneration braking energy recovery, and for reducing the peak load and transients seen by the engine. A relatively small pack of advanced lead acid batteries is use for energy storage. The design, development and evaluation exercises are fully described giving a comprehensive insight of the prototype and its capabilities.

Keywords : *Automotive, parallel, electric motor, batteries, hybrid*

NOMENCLATURE

P_{road}	Road power demand, kW
P_{roll}	Power to overcome rolling resistance, kW
P_{hill}	Power required for hill climbing, kW
P_{aero}	Power to overcome aerodynamic drag, kW
P_{accel}	Power for acceleration, kW
m	Mass, kg
g	Gravitational constant, 9.81 m/s^2
V	Velocity, m/s
C_{-r}	Rolling resistance coefficient
C_d	Aerodynamic drag coefficient
r	Density of air, kg/m^3
A	Frontal area of vehicle, m^2
ICE	Internal Combustion Engine
SOC	State of Charge
HEV	Hybrid Electric Vehicle

INTRODUCTION

Today's motorised vehicles can be improved from the perspective of fuel economy and emission. While the major auto manufacturers invest huge sums to perfect the fuel cell technology, electric hybrid system – a conventional internal combustion engine boosted by an electric motor – looks the more likely to be the interim technology, before fuel cell can be the ideal replacement of the low efficiency internal combustion engines.

Hybrid systems are essentially tandem energy sources. Hybrids offer major advantages - they can provide the best of both performance and fuel economy in the same package and able to capture energy usually lost in braking and recover it as electric energy. All these looks promising provided the systems be reasonably priced. Hybrid configurations are generally more complex in design compared to vehicles with conventional powertrains. They contain various extra components and the interaction and energy flows between components, as well as their management is more complex. Despite this, it offers certain design flexibility as powertrain components can be placed in different parts of the vehicle where practical.

In a hybrid system, the internal combustion engine (ICE) can operate at a constant speed to charge the engine alternator and generate power for the electric traction motors - a series approach. Likewise, it is can be linked directly to the drive train and propel the vehicle in parallel using electric motors – a parallel system. A group of researchers from UTM has undertaken to develop a prototype electric hybrid power plant in the first of the many phases of the development program, from design to prototyping, dedicated for automotive application.

DESIGN OBJECTIVES

The aims of building the electric hybrid power plant are:

1. Component integration and design
2. Control algorithm
3. System architecture development

The unforeseeable objective is the establishment of the learning curve in developing such technology on a low cost research budget.

PARALLEL VERSUS SERIES

In initiating such a broad base R&D project, the choice of either series or parallel configuration must be seriously given due consideration.

Series Hybrids: Most beneficial in city driving conditions, since electric motors, which operate efficiently through a wide range of conditions, propel the vehicle. The IC engine can run at a constant speed to operate the

073-080·develop&perform 9/20/05 12:51 PM Page 74

alternator, while regenerative braking captures braking efficiency energy normally lost to help charge the batteries. The engine of series hybrid is uncoupled from the road load and runs in either a fixed or a restricted range of operating points. The engine-generator set generally supplies the average demanded power, while an energy storage device (mostly batteries) supplies peak power.

Parallel Hybrids: Most efficient at highway speeds, since the IC engine is directly connected to the drive wheels and an electric motor can augment the IC engine during launches and acceleration. Regenerative braking and surplus power from the engine keep the batteries charged. The two power sources may contribute torque separately or in combination with each other. This offer design flexibility of the components placement.

The parallel hybrid electric configuration is the choice for two main reasons. First, a hybrid vehicle yields the most acceptable combination of the low emissions and high-energy economy achieved by electric vehicles with the superior range and performance of an IC engine vehicle [1]. Second, an extremely high efficiency IC engine was available to the team with a peak power of 54 kW (86 hp). These traits allow parallel hybrid to perform well in high load, high average power conditions. This is the choice of many interested parties and is well demonstrated by a group of engineering students (univ. of Wisconsin, US) who is an active participant in the annual Future Truck competition [2].

DESIGN OF HYBRID ELECTRIC VEHICLE

A hybrid electric vehicle (HEV) has two sources of on-board power. The integration of these power-producing components with the electrical energy storage components allows for many different types of HEV designs. The flexibility in the design comes from the ability of the control strategy to manage how much power is flowing to or from each component. This way, the components are match with the control strategy to achieve the optimal design for a given set of design constraints. There are many, often conflicting objectives desirable for HEVs. The primary ones being:

- maximise fuel economy
- minimise emissions
- minimise propulsion system to keep cost affordable
- do all the above while maintaining or improving upon acceptable performance (acceleration, range, noise etc.)

To achieve these objectives, both the hardware configuration and the power control strategy are integrated as a package. The hardware configuration dictates to some extent what control strategies make sense, although there is a wide spectrum of control strategies for each hardware configuration. As described earlier, a parallel hybrid configuration was selected based on the project requirements and literature studies. The series layout was not given consideration because of its low overall power conversion efficiency [2]. It is required to convert the mechanical energy of engine to electrical energy at the generator, and finally to mechanical energy at the motor.

In the parallel configuration, the engine and electric motor are parallel to one another, with their shafts coupled by a torque coupler so that the combined torque can be absorb by the dynamometer (Figure 1). The torque coupler consists of, one-way clutch, electro-magnetic clutch and belt drive. With a one-way clutch on the engine shaft output, the electric motor can directed motive power to the dynamometer without driving the engine. Further, by decoupling the electro-magnetic clutch on the motor shaft, the engine can run independently as prime mover. The one-way clutch and electro-magnetic clutch transition the parallel hybrid powertrain from one mode of operation to another.

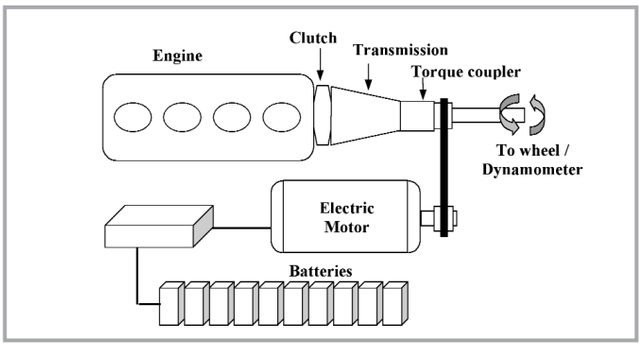

Figure 1: The parallel power plant configuration

VEHICLE ENERGY ANALYSIS

The Road power demand equation represents the energy consumption of a vehicle over a period. This equation defines how power is use in a vehicle as it travels down the road. It is the principle behind the vehicle simulation and all the components and modifications integrated into the vehicle. Equation 1 describes the road power demand in details.

$$P_{road} = P_{roll}+P_{hill}+P_{aero}+P_{accel}+P_{aux} \quad (1)$$

It encompasses all of the vehicle design aspects that UTM-HEV team could vary to improve the overall economy. The relative importance of reducing the different parameters of the equation is shown in Figure 2.

In order to increase the fuel economy of the vehicle the road power demand must be decreased, which is accomplish by reducing the power demands that make up the road power.

The power to overcome rolling resistance is equal to the product of the vehicle mass, gravity, velocity, coefficient of rolling resistance, and the cosine angle that the road makes with

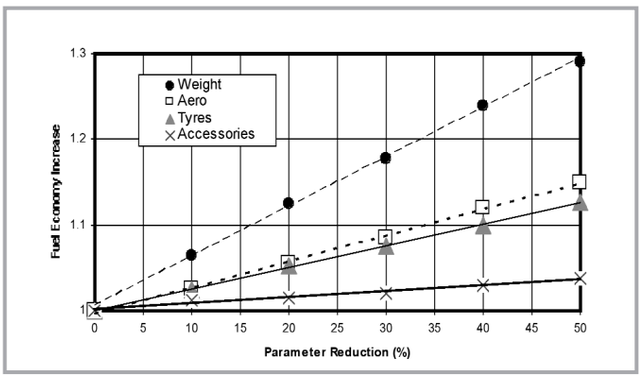

Figure 2: Parameter reduction to increase fuel economy [3]

073-080·develop&perform 9/20/05 12:51 PM Page 75

level ground. Equation 2 describes this fact in details.

$$P_{roll} = mg\ VC_r \cos\theta \quad (2)$$

This power loss is reduced by aggressively pursuing weight reduction in the vehicle through numerous means. Selecting tyres with a very low rolling resistance will also prove the system performance.

The second portion of road power demand is the power required to climb hills. The value for the hill power loss is determined using Equation 3.

$$P_{hill} = mgV\sin\theta \quad (3)$$

Mass is the only portion of this equation that can be changed in the design.

The third power loss is due to aerodynamic drag. Shown as Equation 4, aerodynamic drag power loss is dependent on the air density, front area profile, velocity, and the coefficient of aerodynamic drag.

$$P_{aero} = 0.5\ rAV^3C_d \quad (4)$$

In the above equation, the front area profile and drag coefficient are the only changeable parameters.

Equation 5 is the power consumption caused by acceleration.

$$P_{accel} = d/dt\ E_{kinetic} = m\ V\ dV/dt \quad (5)$$

Again, mass reduction appears as a key to energy economy, but neither the velocity nor the change in velocity (with respect to time) are altered in the design.

The final portion of the road power demanded is the energy drawn by the auxiliary functions. This power consumption is reduced in the Perodua Rusa van by employing a smaller localised air conditioning system. Equations to quantify auxiliary power are more complex than this discussion warrants and have been omitted.

COMPUTER MODEL

A parallel hybrid drive train was conceptualised, simulated, fabricated, and assembled at the Automotive Development Centre (ADC), in UTM. All parts used were off-the-shelf, except for the control system, which was custom designed and fabricated.

Prior to developing the hardware, a rigorous computer model of the drive train was developed using the ADVISOR, a hybrid modeling and simulation software produced by NREL (National Renewable Energy Laboratory). For reasons of brevity, the mathematical model derivation of the drive train is omitted. ADVISOR is a Matlab/Simulink ‘ based simulation analysis tool.

The developed computer model is of the forward-looking type, with a driver sending commands to the drive train controller based on vehicle speed deviation from the desired driving schedule.

DRIVETRAIN SIMULATION

The parallel electric hybrid power plant combines an IC engine and an electric motor, drawing energy from gasoline fuel and batteries. Prediction of how the changing one aspect of the drive train will interact and affect the performance of the other systems becomes very difficult, especially under varying driving conditions. An effective control strategy must balance several design tradeoffs that each plays a role in the overall efficiency of the vehicle. The team needed an inexpensive but a fast method to make sound engineering decisions regarding what components to use and how to tune them once installed in the vehicle. For this reason, the research team developed the system using the computer simulation approach, i.e. the dynamic simulation program, i.e. the dynamic simulation program SIMULINK.

CONTROL STRATEGY

The team has also developed a hybrid control strategy capable of regulating state of charge (SOC) and load leveling. A SOC regulating strategy will monitor the battery voltage level and maintain the voltage within a prescribed range, neither full nor empty. Transient emissions caused by the changes in the engine load, was over come by the use of the electric motor. The gradual increase in engine power output is up set by the motor output. Buffering the engine from the road in this manner also increases the vehicle fuel economy. Keeping the average engine load within the permissible limits controls steady state emission concentrations.

The control system (refer Figure 3) was developed as a machine with four conditional states. Upon assigning the control strategy as a finite state machine, the software is restricted to run in a sequence of one state at a time. Since the current vehicle state can always be determined, each state can be tested, debugged, and tuned separately. Each of the states is reviewed in the following sections.

STATE 1: ENGINE ONLY

The first state is engine only mode. In this state, the vehicle operates as if the electrical system were not present. All pedal commands go directly to the engine and the motor provides no load leveling assistance. This state is use during vehicle forward driving, high speed coasting, and battery recharging operation. When conditions dictate for high voltage requirements, the state ceases to operate. The state is not for reverse driving.

STATE 2: ELECTRIC ONLY

The second state is electric only mode. In this state, the vehicle operates as pure electric vehicle. All pedal commands go to the electric motor through motor speed controller. This state is use during low speed operation or city driving and reverses driving within the sufficient SOC of the battery. When the battery SOC drops to low level, the state will automatically change to Hybrid state.

STATE 3: REGENERATIVE BRAKING

The third state is the regenerative braking system state. Regenerative braking is the act of using the mechanical energy from the wheels to drive the motor, generating electricity for storage in the battery. This process recharges the battery while decreasing the vehicle speed.

The vehicle goes into the regenerative braking state only if the brake pedal is depressed and the high voltage system has room to store energy. All regenerative braking commands are passed through a set of filters. The first filter reduces the regenerative motor commands at low velocities to avoid "chatter" present at

073-080·develop&perform 9/20/05 12:51 PM Page 76

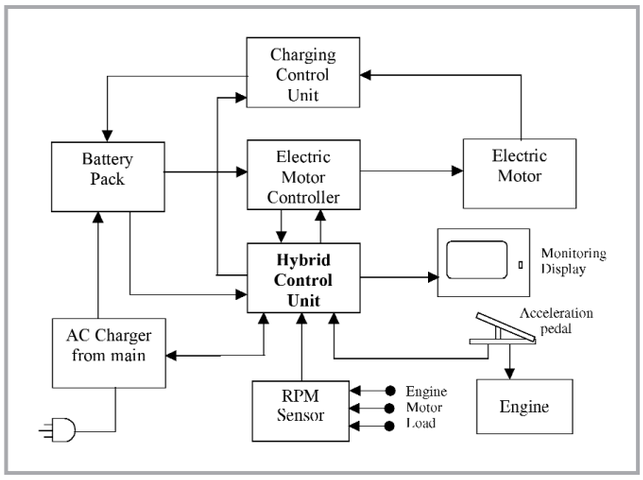

Figure 3: Schematic diagram of the control system

low motor speeds. The second filter reduces regenerative commands as the SOC approaches dangerously high levels.

STATE 4: HYBRID

HYBRID state is the forth and most common state of the control strategy. It contains the SOC regulator control code, that manages the battery voltage as previously described. The range within the high and low bounds of the SOC regulator is called the SOC dead-zone. The dead-zone, set approximately between 50 to 60% SOC, adjusts for the best efficiency during battery charging and discharging. While in the HEV state, the control system will make use of both the engine and the motor conditions to meet the driver's demands.

COMPONENTS IDENTIFICATION AND SELECTION

With the overall parallel powertrain chosen and the road load energy analysed, it was time to select the major components so that the complete drivetrain could be developed. Firstly, the two power sources must be determined. The team had selected the gasoline engine as the prime mover, while the electric motor as mover to augment the engine.

ENGINE

The engine is to provide the average power needed for all operating conditions. A Daihatsu gasoline 1.3 litre engine is use for the hybrid system design. The engine has sufficient power to maintain a highway cruising mode of 110 km/hr.

ELECTRIC MOTOR

One of the most critical components of a HEV is the electric motor. The selection was due to its efficiency, performance, functionality and size. DC motors are typically easier to control, thus their controllers tend to be less expansive [4]. The Nexus brushed DC motor was the choice. It was originally develop as part of the hybrid electric-diesel bus drive system in the UK. The motor has a rated power of 27.5 kW (at 160 VDC, 60 minutes rating) and a peak torque of 180 Nm (at 55 kW). The speed range of the motor is up to 7000 rpm having a bulk mass of 80 kg and input voltage ranging from 24 to 160 V respectively.

With the power sources selected, the remaining components selection can now be made and the overall layout finalised. The parallel electric hybrid powertrain layout is shown in Figure 4. The components shown in this figure are described in the following paragraph.

Table 1: Engine specifications

Type	Petrol engine, in-line, 4-cylinder, 4-cycle, 16 valve, SOHC
Displacement	1296 cc
Compression ratio	9.5:1
Max. output	54 kW/6000 rpm
Max. torque	101 Nm/3200 rpm

A. ENGINE

The engine selected was a four cylinder, in-line, 53 kW, gasoline type. The engine and its accessories are supported by a custom-made frame.

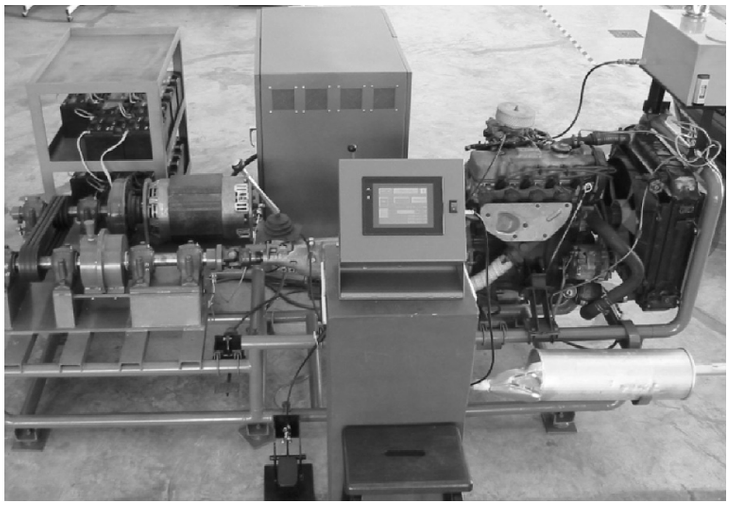

Figure 4: Photograph of the parallel hybrid power plant

B. ELECTRIC MOTOR

Nexus brushed DC motor with rated power of 27.5 kW and maximum torque of 180 Nm.

C. BATTERY PACK

Electrochemical batteries are the most commonly used devices in hybrid vehicles. Due to cost constraint and availability, Hawker Genesis advanced lead-acid battery was selected, with specification of 12 Volt and 42 Ah respectively. The batteries are arranged in series to supply power to the electric motor.

D. TRANSMISSION

A 5-speed manual transmission was used in the laboratory evaluation of the parallel hybrid arrangement.

E. CONTROL UNIT

The control unit built up of motor controller, speed encoder, switches, safety devices, and power electronic components. The heart of the hybrid control is the Siemen programmable logic controller (PLC), which integrates all components involved.

073-080·develop&perform 9/20/05 12:51 PM Page 77

F. Belt Drive

The two parallel shafts were coupled by belt drive assembly and were supported by bearings. The structure of the platform enables drivetrain offset and adjustment to the tensioning of the drive belt be made.

G. One-way Clutch

In order to allow electric motor to operate without driving the engine, a one-way clutch or overrunning clutch is needed. This enables the engine to be isolated when it is not required, and to start and rotate up to the motor speed when its torque is needed to execute certain portion of the drive cycle. The Means One-way clutch which suitable for high rotational speed and torque for automotive transmission purpose is selected (refer to Figure 5.a).

H. Electro-magnetic Clutch

In engine mode operation, electric motor is disconnected from the main drive shaft. A high speed and high torque electro-magnetic clutch is needed for this application. Warner Electric clutch with static torque of 350 Nm and maximum running speed of 3600 rpm was selected (refer to Figure 5.b).

(a) One-way Clutch (b) Electro-magnetic Clutch

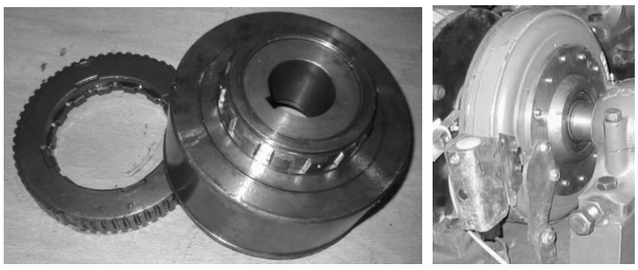

Figure 5: Photographs of the clutches

I. Flexible Coupling

Flexible coupling protect against misalignment that may damage the components.

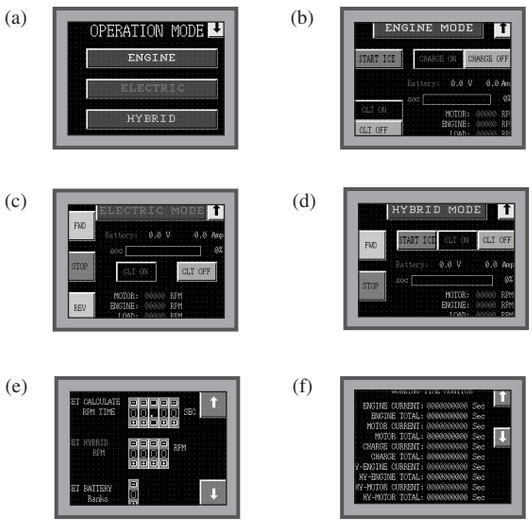

Figure 6: The displays of touch screen

J. Acceleration Pedal

The acceleration pedal was a combination design specially to throttle the engine and control the electric motor speed.

K. Touch Screen

The touch screen facilitate display, monitor and control. It serves as a user-friendly way for control parameter input. Omron touch pad was selected. Figure 6 shows several views of touch screen display windows. When the system is switch on, the screen display three operation modes for selection (Figure 6.a). By touching the desire box on the screen will select the mode for driving. Each operation modes (Figure 6.b, c and d) display driving command (forward, reverse, and stop), electro-magnetic clutch status ("CLT ON" for clutch engage, "CLT OFF" for clutch disengage), button to start engine (ICE), battery SOC and rotational speed displays. Operator can also set parameter input (Figure 6.e) and monitor the working time of various components (Figure 6.f).

SEQUENCE OF OPERATION

The operation of hybrid electric vehicle is meant for maximising fuel economy and reducing emission that makes use the advantages of both power sources. Therefore, three modes of operation are specified. They are (i) Engine mode, (ii) Electric mode and (iii) Hybrid mode. The selection of mode depend on the driving requirement and available of battery charge. The battery level is measure in state of charge (SOC). When the battery is full, SOC indicates 100% and when the battery is empty, SOC indicates zero. The control system will monitor the SOC within the range of 40% to 100%. The three-operational mode control strategy is shown in Figure 7 and 8.

For high SOC, the vehicle operates as electric vehicle at low speed. When power requirement is above electric motor capability, engine will take over the driving task in hybrid mode. During high speed, the vehicle operates as conventional vehicle. Battery charging is possible. If hard acceleration or high power is needed exceeding engine capability, electric motor will assist in hybrid mode.

For low SOC, certainly the vehicle operates in engine mode and charges the battery whenever have excessive power.

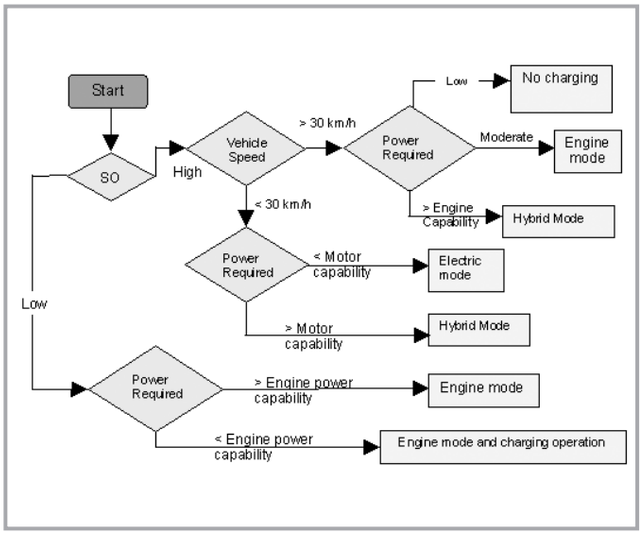

Figure 7: Flow chart of control strategy

073-080·develop&perform 9/20/05 12:51 PM Page 78

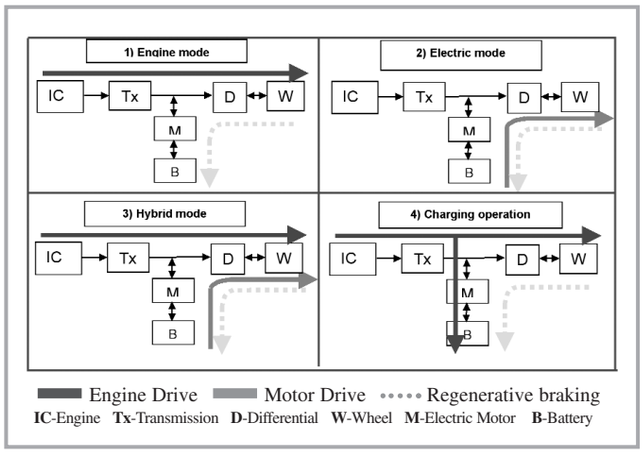

Figure 8: Power flow of multi-mode control strategy

ENGINE MODE

This mode is for highway driving and when the battery SOC is low. ICE provides power for forward driving requirement. The vehicle will functions as conventional vehicle except for reversing, where the electric power is opt. Extra power of the engine is use to charge the battery until reaching high SOC. While charging, the electro-magnetic clutch will be engaged.

ELECTRIC MODE

This mode is for urban driving and when the battery SOC is high. The vehicle will be completely driven by the electric powered motor. The electro-magnetic clutch will be engaged. It is only intended for short driving range, which is restricted by the battery capacity.

HYBRID MODE

Hybrid mode is the most common mode during driving. In this mode, the electric motor is to accelerate the vehicle from rest to a speed of 30 km/h. Once reaching the speed, the engine is activated to provide motive power. The engine can adequately provide power up to 100 km/h and climbing at 5% gradient. During high acceleration and load, the motor will assist the engine in meeting the power demand. The vehicle drives in reverse when it is in the electric mode.

Regenerative braking will be present in all the modes to salvage the recovered energy and stored in the battery.

PERFORMANCE EVALUATION

Two driving cycles were use to predict the power plant performance and emission results, as shown in Figure 9. The Urban Dynamometer Driving Schedule (UDDS) was used for city test and represents city driving condition [5]. The Highway Fuel Economy Test (HWFET) on the other hand, is to simulate for highway driving. Currently it is use by the US EPA for Corporate Average Fuel Economy (CAFÉ) certification of passenger vehicles in the United State.

RESULTS AND DISCUSSION

The performances of the batteries, motor and engine (in conjunction with the UDDS driving cycle, in hybrid mode) are shown in Figure 10. The type of control strategy used is "parallel electric assist" [6]. Here the motor is to provide additional power when needed by the vehicle and to maintain the state of charge (SOC). By observing the battery performance, the SOC is opted, and maintain above 60%. The initial battery SOC is 70%. Through out the driving cycle, the engine is the sole source power. It provides the average driving power to the vehicle while the motor is to augment the engine. As seen in the chart of motor power, the electric motor provides motive power during starting. Negative torque is noticeable in the motor during deceleration. At this stage, motor acts as a generator to recover kinetic energy, which is to charge the battery. As a whole, the simulated Parallel HEV is strictly in the path the driving cycle.

Figure 11 shows comparison of the simulation results of conventional vehicle and parallel Hybrid Electric Vehicle

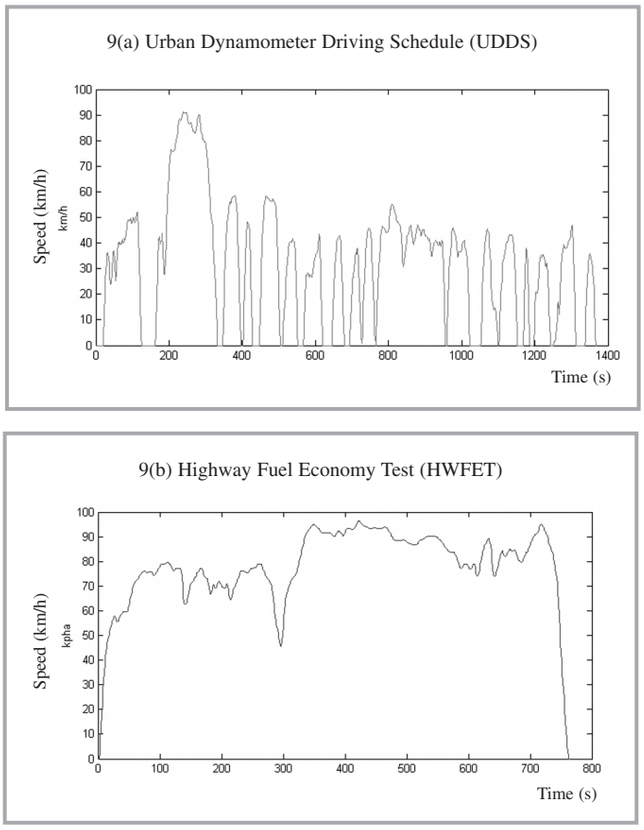

Figure 9: Driving cycle for power plant evaluation

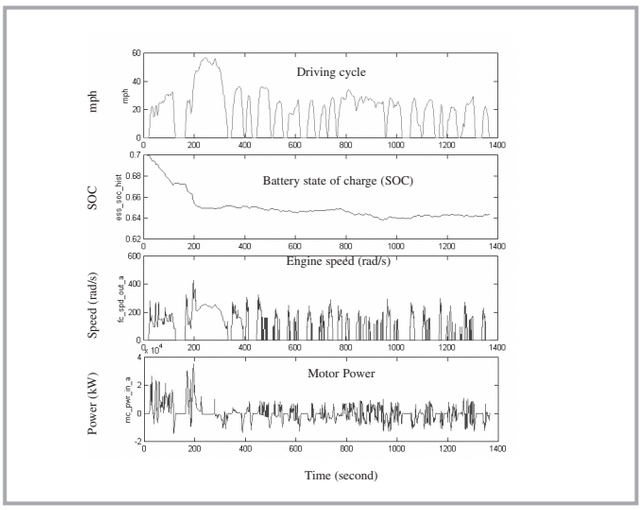

Figure 10: Simulation result of UDDS cycle

073-080·develop&perform 9/20/05 12:51 PM Page 79

(HEV). Results indicate parallel HEV obtained fuel economy of 28.6 mpg as compared to 24.6 mpg of conventional power plant on the same platform running on the driving cycle of UDDS. HEV also achieved better acceleration performance. However, the gradeability at 55 mph is lower than conventional vehicle because hybrid vehicle carries extra weight of batteries and electric motor. Gradeability refers to the maximum grade the vehicle is able to maintain at 55 mph for 10 seconds. It is based on the requirement of PNGV (Partnership for a New Generation of Vehicle) associate with fuel economy and emission.

Table 2 summarises the emission concentration produced in UDDS cycle. Here the total emission concentration was

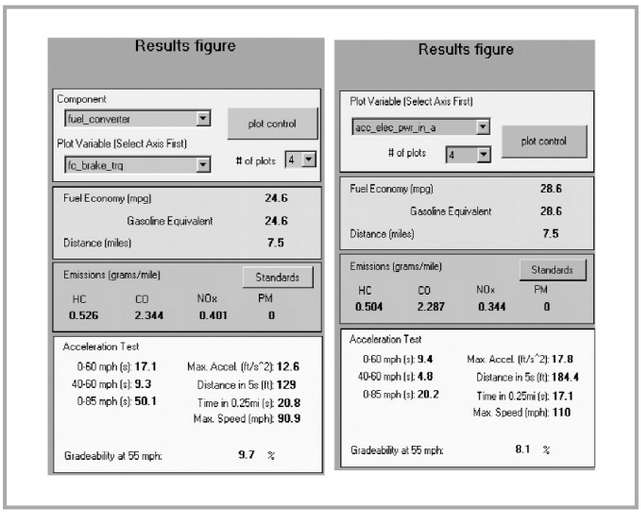

Figure 11: Results of conventional vehicle and hybrid electric vehicle

reduced drastically. Both the UDDS and HWFET test cycles depict promising results from the emission perspective. Same vehicle parameters were used which is the Perodua Rusa van with coefficient of drag 0.5, coefficient of rolling resistant 0.015 and frontal area of 2.221 m2. Both used the 54 kW engine. Figure 12 illustrates the results. High emission can only be seen in the beginning of the cycle. Hybrid operation in electric mode assists in keeping the emission level to the minimum.

Table 2: Emission levels

Regulated Emission	Emission Levels (gram/mile)
Hydrocarbon (HC)	0.504
Carbon Monoxide (CO)	2.207
NOx	0.344
Particle Material (PM)	0

CONCLUSIONS

A parallel hybrid power train system based on the combination of an internal combustion engine and a dedicated electric motor was successfully developed and evaluated. The hybrid control strategy is to use the electric motor for initial acceleration, for battery charging and regenerative braking energy recovery, and to assist the engine when it's not operate effectively. This has been well developed and demonstrated to be feasible. From the

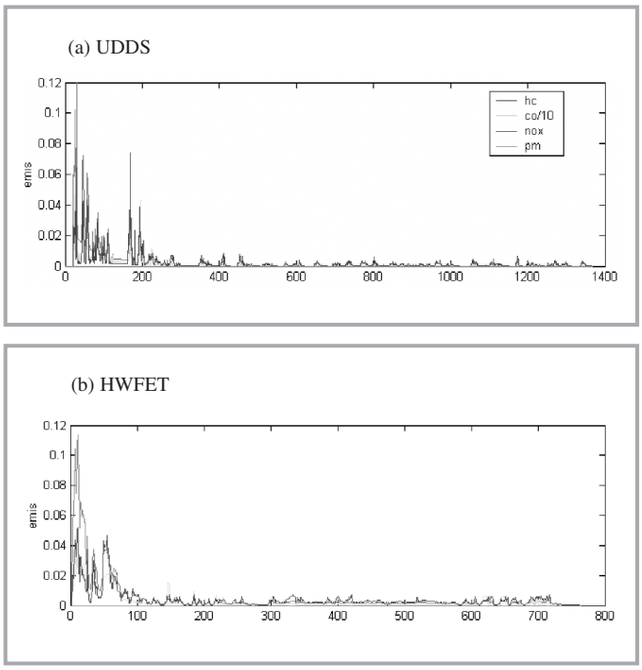

Figure 12: Emission charts

aspects of performance, the system has demonstrated its potential to minimise emission and fuel economy.

The completion of parallel electric hybrid prototype has brought many challenges and new ideas for improvement. In the second phase of the project, it will focus on the refinement of the complete system to render it having higher power-to-weight, smooth switching modes and power-to-volume ratios, suitable for fitting onto a platform (reference vehicle) for field trial evaluations.

ACKNOWLEDGEMENTS

The IRPA's advisory committee at MOSTI (Malaysia's Ministry of science, technology and Innovation) approved the research grant for the project in the year 2000. The cooperation and encouragement by all parties in ensuring the success of the project implementation are gratefully acknowledged. ■

REFERENCES

[1] Y. Gao, L. Chen, and M. Ehsani, "Investigation of the Effectiveness of Regenerative Braking for EV and HEV", SAE Paper 1999-01-2910, 1999.

[2] P.E. Ross, "Start Your Motors!", Feature Article, IEEE Spectrum, Oct. 2003.

[3] A.D. Vyas, H.K. Ng, D.J. Santini, and J.L. Anderson, "Electric and Hybrid Electric Vehicle: A Technology Assessment Based on a Two-Stage Delphi Study", Argonne National Laboratory Report ANL/ESD-36, Argonne, IL, 1997.

[4] N.M. LeBlanc, M. Douba, S. Quong, R.P. Larsen, M. Stithim, and W. Rimkus, "Technical Analysis of the 1994 HEV Challenge", SAE Paper 950176, 1995.

073-080·develop&perform 9/20/05 12:51 PM Page 80

[5] S. Sluder, M. Duoba, and R. Larson, "Evaluation of High Energy Efficiency Powertrain Approaches. The 1996 Future Car Challenge", SAE SP 1234, 1997.

[6] National Renewable Energy Laboratory, ADVISOR homepage, http://www.ctts.nrel. gov/analysis/

[7] B.K. Powell, K.E. Bailey, and S.R. Cikanek, "Dynamic Modelling and Control of Hybrid Electric Vehicle Powertrain System", IEEE Control System, October 1998, pp 17-33, Oct. 1998.

[8] J.S. Burn, N.D. Lamar, M.O. Dimick, and S.J. Granger, "Development of the L3: An Efficient, High-power, Clean Fueled, Parallel Format, Hybrid Vehicle", SAE Paper 2000-01-3097, 2000.

[9] R. Dimitrios, J. Burl, and J. Beard, "Control Strategies for a Series-Parallel Hybrid Electric Vehicle", SAE Paper 2001-01-1354, 2001.

[10] A. Abdul Aziz, L. C. Wei, and K. B. Tawi, "A Dedicated Parallel Hybrid Automotive Power Plant for a Small Utility Vehicle", 6th Asia-Pacific International Symposium on Combustion and Energy Utilization (APISCEU), Kuala Lumpur, 2002.

INFORMATION

THE JOURNAL OF THE INSTITUTION OF ENGINEERS, MALAYSIA

AIMS OF IEM JOURNAL

The Journal is intended to be a forum for a publication and discussion of current practice and future developments in all engineering disciplines.

Practical papers are particularly sought in which examples of good present practice can be described and disseminated for the benefit of professional engineers in industry. The propose is to encourage the widest possible readership and to keep the audience fully informed of the latest developments and practices, both in Malaysia and throughout the world.

Papers of high technical merit relying on mathematical arguments and computation will be considered but author are urged to relegate as far as possible the details of analysis to an appendix. The aim is to convey the essential arguments and conclusions, and their relevance to present problems as simply as possible in the main text so that the paper is understandable to the widest possible audience of professional engineers.

To maintain the standard of the paper, a system of specialist refereeing is employed. Referees are asked to be particularly concerned with the clarity and depth of treatment as well as the particularly and topicality of the subject.

The editors endeavour to balance practice and theory as far as contribution allow so that the Journal is suited to the needs of practicing engineers as well as those in teaching and research.

TASK OF THE REFEREES

The main object of the refereeing procedure is to protect the reputation of the journal by excluding any material which is not original or significant or which is not sufficiently concise or well presented. A referee need not concern himself if with minor editorial matters.

While a referee is obviously expected to draw attention to obvious errors, he should not criticize a paper adversely merely because he does not agree with all its ideas, or because he does not favour the methods or procedures that it advocates. He should try to recognise real merit, even in a paper, which to him personally is uninteresting or unattractive.

Referees are asked not to mark the manuscript of the paper in any way, except that, if really necessary, small marginal asterisks, or numerals, for across-reference to the referee's report, may be lightly inserted in pencil. If a reference decides to refer a paper to a colleague to reinforce his opinion, this must be done under confidential cover.

PRESENTATION

Referees are asked to consider whether the author presents his material logically, in clear and direct English and in as concise a manner as possible. Referees are asked to consider most carefully whether any paper can be shortened, and to give instructions as to how any length reduction can be achieved.

MATHEMATICS

Referees are asked to consider whether all the mathematics is essential or which parts can be deleted or relegated to an Appendix.

ILLUSTRATIONS

Experimental result can often be displayed more effectively be means of graphs than by tabulation, but, when a graph shows merely a simple mathematical law, it should be omitted and the author should be asked to present the facts in word or symbols. If the paper included tables and graphs (or other diagrams) presenting the same data, this should be pointed out by the referee. Detailed engineering drawings or wiring diagrams are preferable.

REFERENCES

Referees are asked to consider whether the references are adequate. If important recent references have been omitted it will help if the referee would indicate where these might found. If references are quoted which might difficult to locate, the referee is asked to consider whether these are necessary.

ABSTRACT

The abstract is an essential part of the paper. It should be as concise as possible, and should comprise a brief and factual summary of the contents and conclusions of the paper, refer to any new information that it may contain, and given an indication of its relevance. It should be intelligible in itself without reference to the paper.